# BENT TAIL RADIO SOURCES AS TRACERS OF GALAXY CLUSTERS AT HIGH REDSHIFT AND SMBH MASS ESTIMATES

Zolile Martin Mguda
Department of Astronomy
University of Cape Town
Rondebosch
South Africa

A thesis submitted for the degree of Doctor of Philosophy

November 2020

# Declaration of Authorship

I, Zolile Martin Mguda, know the meaning of plagiarism, and declare that all of the work in the thesis, save for that which is properly acknowledged, is my own. The thesis has been submitted to the Turnitin module and I confirm that my supervisor has seen my report and any concerns revealed by such have been resolved with my supervisor.

Signed : Signed by candidate

Date : 07 January 2020

# Contents

# List of Figures

# List of Tables

# Abstract

Bent tail radio sources (BTRSs) are radio galaxies which have jets that show a characteristic C-shape that is believed to be due to ram pressure caused by the motion of the galaxy through the ambient medium. They are generally found in galaxy clusters in the local Universe. They have already been used in observations as tracers of galaxy clusters at redshifts of up to $z \sim 1$. They have, however, been shown to be numerous in galaxy groups as well. The ability to find high redshift galaxy clusters is important in cosmology because they are important cosmological probes. According to the $\Lambda-$CDM model, galaxy clusters form around redshift of $z \sim 2$ and finding clusters of halo mass greater than $10^{14}$ $\mathrm{M}_{\odot}$ at redshift greater than $z = 2.5$ would disprove the current concordance model. Finding galaxy clusters at those redshifts is more feasible with the new generation of radio telescopes and the upcoming square kilometer array (SKA).

In this work we look at some SMBH mass measurements, which are crucial in the determination of the correlations between the SMBH mass and some galaxy characteristics including jet length and luminosity. The high redshift SMBH mass measurement methods are calibrated using local Universe correlations. This makes SMBH mass measurement an important aspect in the study of high redshift radio galaxies and hence BTRSs. We use cosmological simulations from the MareNostrum Universe simulation to look at the efficacy of using BTRSs as tracers of clusters assuming the ram pressure is the cause of the jet bending. This is the first step in predicting the possible number of BTRSs that we may observe with the SKA.

We find that SMBH masses can be measured up to redshift of $z = 4.5$ using the virial mass estimator method. The BTRSs are equally likely to be found in galaxy clusters and galaxy groups in the local Universe. This means that around 50 % of the BTRSs that we are likely to find at high redshift will be in galaxy clusters. However, finding a pair of BTRSs in close proximity is a sign of a galaxy cluster environment. These results are still dependent on the resolution of degeneracies in our understanding of the duty cycles of AGN radio jets, projection effects of the radio jets, the environmental dependence of radio-loudness in galaxies and other open questions.

# Acknowledgements

To my kids Lihlithuba, Sivenathi, Lunathi, nabasesesinqeni, “It takes a village...”

I would like to thank my family, nuclear and extended, for forming and affirming me. To my late dad “ndithi Dabane!” and to my late mother – without whom it is inconceivable that I would have made it this far – “kere ’Mme maMohlakoana, ke ho leboha kapelo ea ka eohle. Ketšepa hore ketlalula kelatela tsela ebakang hore obe motlotlo.” To my family members who perished along the journey, “You shall be missed. Siyolo and Andiswa you have gone too soon. Sobonana kwelizayo, elamanyange.”

I thank my mates at the ‘fish tank’ for the cameraderie, advice, encouragement and a general atmosphere that made me a better person. I thank the wider NASSP community, the staff at the South African Astronomical Observatory and the Astronomy Department of the University of Cape Town with the words, “Enkosi ngokundiluleka.”

To the students and post-docs that I have had the pleasure to meet during this time, I thank you with the isiXhosa saying, “Nenjenjalo nakwabanye (May you do the same for others also).” To the A-team and the Department of Mathematical Sciences at the University of South Africa, thank you for welcoming me and challenging me to be better.

To my friends, who are too numerous to mention, at UCT, SAAO and UNISA, “The road was easier because you shared it with me.” I salute my supervisors Drs K. J. van der Heyden and P. Vaisanen. I salute my mentors Prof D. P. Smits (thanks Alpha) and Prof A. Faltenbacher (danke mein herr) and thank Prof Tom Jarrett, who, together with Prof Smits, edited my thesis. I would like to thank Prof R. Kraan-Korteweg and Prof P. Whitelock for continued support.

There has been many individuals who have made invaluable contributions to my journey and there is not enough space to name all of you individually. I would like to single out the following people, who have helped in this work, Drs Iniyan Natarajan, Danielle Lucero, Bruno Letarte & family and Prof Lerothodi Leeuw.

I would like to thank the NASSP and NRF for financial support.

# Chapter 1

# Introduction

Humanity has come a long way in understanding the Universe; how it works, how it may have started and where we think it will end. There are still gaps in our understanding, but the general picture is well-established and extensively studied. This knowledge is used to explain and predict natural phenomena.

In this work, the use of the theoretical knowledge of a bent tail radio source (BTRS), and the physics involved, to trace the presence of galaxy clusters and galaxy groups at high redshift. We also look at the role supermassive blackhole mass measurements play in our ability to predict the prevalence of radio loud AGNs at higher redshifts. We look at two methods used in SMBH mass measurements. One is used in the local Universe due to its reliance on high spatial resolution. The second can be used up to a redshift greater than 2. It is based on spectroscopy of broad emission lines produced in the central engines of AGNs. This method is calibrated using results of SMBH mass measurements performed via reverberation mapping in the local Universe. This suggests that the study of radio galaxies relies heavily on constraining SMBH masses at all redshifts.

BTRSs are extended radio galaxies whose radio jets show a characteristic C-shaped morphology which can be as severe as V-shaped in cases of a high degree of bending. The bending is thought to be a result of the ram pressure exerted on the jets by ambient gas when the relative velocity between the ambient gas and the radio galaxy is large. These are conditions that are predominantly found within galaxy groups and clusters.

Blanton et al. (2000) have already done a similar study using observations with the very large array (VLA) telescope's faint images of the radio sky at twenty-cm (FIRST) survey (Becker et al., 1995). They managed to find galaxy groups and clusters using BTRSs in their samples. Here their hypothesis is approached from a simulation point of view to determine if the efficacy of this method, as seen at low redshift, can be extended to high redshift ($z \geq 1$). Whether this method only traces galaxy clusters or it also traces galaxy groups is also explored. The latter is an important question as it is currently not adequately addressed in the literature. The distinction between galaxy clusters and groups may turn out to be a moot point as more statistics on their behaviour and characterisation are gathered but, despite the general expectation that they form a continuum from $\sim 10^{13}$ M$_\odot$ groups to clusters with masses $> 10^{15}$ M$_\odot$, they are currently classed as distinct.

The results of Blanton et al. (2000) and Wing & Blanton (2011) were successfully used to find galaxy clusters up to a redshift of $\approx 1$ (Blanton et al., 2003). These results also showed that BTRSs are also likely to be found in galaxy groups. This is promising for their use as tracers of galaxy clusters and groups at high redshift. With an improved spatial resolution of $\sim 1''$ and a sensitivity of $\sim 10\,\mu$Jy, radio surveys, such as the SKA-MID, may find $\sim 100\,000$ BTRS in the local Universe and at high redshift ($z \geq 8$) (Dehghan et al., 2011; Ghisellini et al., 2014). This method will thus yield even better results.

Finding galaxy clusters throughout the history of the Universe is an important cosmological question because the ΛCDM cosmological model puts a strict constraint on when galaxy clusters greater than a certain halo mass could have formed (Kravtsov & Borgani, 2012; Somerville & Davé, 2015) . This means that finding a galaxy cluster of mass greater that $10^{15}$M$_\odot$ at a redshift much earlier than $z = 2$ could disprove the current cosmological model (Allen et al., 2011; Harrison & Hotchkiss, 2013). In this work, cosmological simulations are used to find cluster-sized dark matter halos in the Universe that have enough mass and baryonic matter density to give rise to the amount of ram pressure required to form BTRSs. This allows for the checking, against observations, of whether the environments of BTRSs are necessarily always clusters or groups.

To study this phenomenon, an understanding of an active galactic nucleus (AGN), its host galaxy and group/cluster environment are needed. To better understand an AGN one has to understand its nuclear activity, where a supermassive blackhole (SMBH) accretes gas and forms radio jets whose luminosity can be observed at great distances. The bending of these jets is what characterises BTRSs. This becomes a study of different aspects of extra-galactic astronomy as well as their evolution and how they come together to form the observed BTRS phenomenon.

One of the most important areas where the evolution of SMBH masses has a significant bearing is the evolution of QSOs and radio-loud AGNs. SMBHs are at the hearts of both and play an integral role in the physics of both phenomena (Kaiser et al., 1997; Mguda et al., 2015). In this thesis we are interested in the role of SMBHs in determining the sizes of the radio jets of AGNs. It is these jets that interact with the ICM/IGM environments, causing their bending (Miley et al., 1972; Venkatesan et al., 1994; Mguda et al., 2015).

QSOs are believed to form through radiative mode accretion, where cold gas is accreted onto the SMBH at rates greater than 1% of the Eddington luminosity and is the likely cause of the $\mathrm{M}-\sigma$ relation (Silk & Rees, 1998). Radiative mode accretion is generally associated with less massive SMBHs found high gas density cores in pseudo-bulges of spiral galaxies (Heckman & Best, 2014). Radio-loud AGNs are believed to form via kinetic mode accretion, where hot gas around high mass SMBHs is accreted at a rate much lower than 1% of the Eddington luminosity, giving rise to AGN jets (Fabian, 2012). Kinetic mode accretion is prevalent in the most massive galaxies in the Universe and in galaxy cluster cores. These are the environments where BTRSs are believed to be likely, hence studying SMBH masses is the first step in the study of BTRSs.

The new generation of radio telescopes, like the low frequency array (LOFAR), the SKA and its pathfinders Karoo array telescope (MeerKAT) and the Australia square kilometer array pathfinder (ASKAP), have sensitivity and sampling speed that will yield a wealth of new radio sources (Agudo et al., 2015; Prandoni & Seymour, 2015). A large number of the sources in continuum surveys are expected to be extended radio sources, with AGN jets which can be detected up to high redshift (Amarantidis et al., 2019). The VLA FIRST Survey (Becker et al., 1995), discussed later in this chapter, has yielded most of the known BTRSs. These BTRSs are thought to be a result of the ram pressure exerted on the jets by ambient ICM/IGM gas of high density when the relative velocity between the ambient gas and the radio galaxy is large. These are conditions that are found within galaxy groups and clusters. If BTRSs are found in clusters, then observing a BTRS at high redshift would help locate where clusters can be found. Optical and NIR surveys are not effective at finding the most massive galaxy clusters far beyond $z = 1.2$ (Ascaso et al., 2014). The advantage of using radio telescopes to locate BTRSs, hence galaxy clusters, is that the sensitivity of radio telescopes would allow the observation of a lot of BTRSs up to redshift $z \geq 2$. Finding BTRSs at high redshift would aid in the investigation of the number density of high mass clusters and how they vary with redshift.

According to hierarchical structure formation, the redshift at which virialised high mass galaxy clusters are found is an interesting cosmological probe because clusters form late in the evolution of the Universe and the timing of their formation depends on the cosmological model (Allen et al., 2004; Planck Collaboration et al., 2013). Finding a massive galaxy cluster much earlier than a redshift of $z \geq 2.5$ may disprove the ΛCDM cosmological model. This chapter discusses the current knowledge of BTRSs and some open questions in the field.

BTRSs first appeared in 1968, when NGC 1265, IC 310, 3C 129 and 3C 465 were observed (Ryle & Windram, 1968; MacDonald et al., 1968). They were classified into two groups, NATs with opening angles less than 45° and WATs, whose opening angles are greater than 90°. These opening angles gave rise to a U-shape for NATs and V-shape for WATs (Rudnick & Owen, 1976; Valentijn, 1979). These classes are discussed later in the chapter.

BTRSs are believed to have a continuous spectrum of bending angles, which depend on the ram pressure exerted by the environment and the degree of stiffness of the radio jet. Most of the BTRSs found in the early days were in rich Abell clusters (Ryle & Windram, 1968; MacDonald et al., 1968; Miley et al., 1972). These Abell clusters are characterised by high velocity dispersion and high ICM densities compared to the less massive galaxy groups. This was initially a significant contributing factor to the belief that ram pressure exerted on the galaxy due to its motion through the ICM, is the cause of the jet bending.

Pursuant to the Fanaroff-Riley classification, a new way of looking at double-lobed galaxies was available that could be useful in classifying the radio properties of BTRSs (Fanaroff & Riley, 1974). This classification, done on a sub-sample of the 199 radio galaxies in the Third Cambridge Radio Catalogue (3CRR) (Mackay, 1971), was both simple and effective because it could be applied to accurately classify ∼95% of the members of the catalogue and it was an easy visual classification. The sub-sample was complete for all members of the 3CRR for which the radio emission can be separated into three or more components (radio blobs.) Fanaroff & Riley (1974) observed double-lobed radio galaxies to have two different morphologies, with a dividing line between them being the radio power at the wavelength 1440 MHz of $\mathrm{P}_{1440} < 5 \times 10^{25}\,\mathrm{W\,Hz}^{1}$, assuming a spectral index of $\alpha = 0.8$: where FR IIs are generally found above that line whereas FR Is generally lie below.

The radio morphology of Fanaroff-Riley galaxies is shown in Fig. 1.1. FR I galaxies are edge-darkened, with the highest radio surface brightness along the jet close to the host galaxy, whereas

FR II galaxies are edge brightened, with the highest radio surface brightness at the outer edges of the jet plumes (Fanaroff & Riley, 1974).

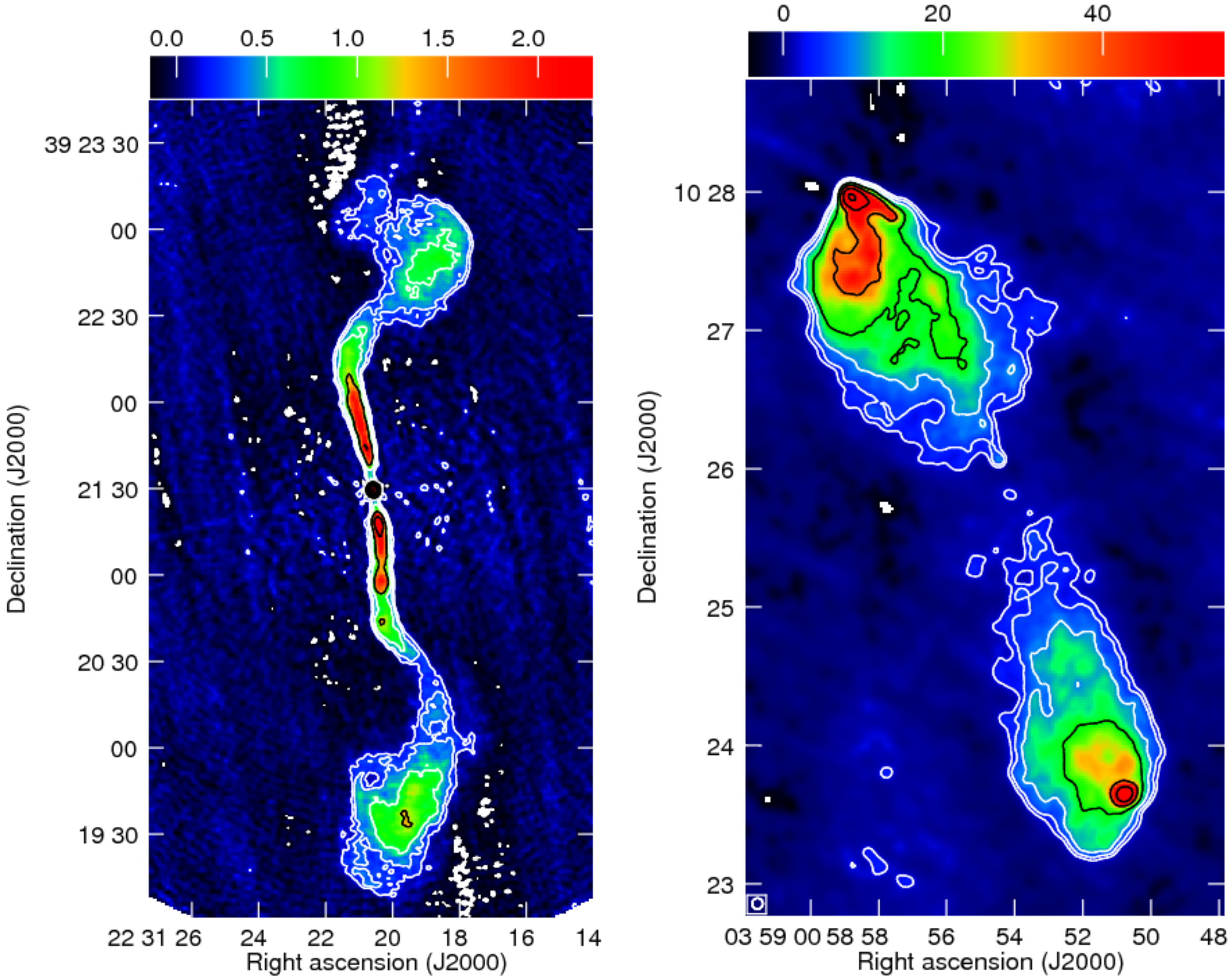

Figure 1.1: Radio images of the FR I galaxy 3C 449 (Left) and the FR II galaxy 3C 98 (Right). The brightest radio emission, shown in red, is closest to the radio core in FR I galaxies and furthest away from the core, at the termination points of the jets, in FR IIs. The units are in mJy per beam. Images are taken from Kharb et al. (2015)

Ekers (1978) is one of the first to recognise the potential of BTRSs as probes of the intergalactic medium (IGM). Most poignantly, by finding the velocity dispersion of the host clusters of NGC 6109 and NGC 6137 to be $\sigma_{\text{cluster}} = 584\ \text{km}\,\text{s}^{-1}$ and $\sigma_{\text{cluster}} = 291\ \text{km}\,\text{s}^{-1}$ respectively, they verified the result of Hill & Longair (1971) and Schilizzi & Ekers (1975) that BTRSs are not only found in Abell clusters, but also occur in poor clusters. This suggests that the high velocity dispersion of the galaxies and the high density of the ICM in galaxy clusters may not be the only explanations for the existence of BTRSs.

Burns (1981) used the VLA to study the morphology of 4C 47.51, which is a cD galaxy at the core of a rich galaxy cluster, and suggested that because the velocity of the galaxy with respect to the environment of this asymmetrical radio galaxy should be low, then the bending is likely due to passive forces such as buoyancy due to pressure gradients. Eilek et al. (1984) studied 3C 465 in the Cluster Abell 2634 and found that no single theory on jet bending could explain the bending of this jet. This suggests that galactic motion, buoyancy, gravitational bending and dynamic pressure could account for the bending of that source, further alluding to the complexity of the causes of bending in AGN radio jets.

Throughout this work, BTRSs are investigated solely based on how the effects of ram pressure on the radio jets would cause the bending. This does not mean the other models for jet bending are deemed invalid or incorrect, but the scope of this study is limited to only ram pressure to enable the comparison with cosmological simulations that are largely based on resolving the motion of galaxies in the gravitational potential of galaxy clusters and groups. These BTRSs were believed to require high density and high velocity dispersion environments found in high mass clusters. A WAT was found as a cD galaxy in a poor Abell Cluster that showed X-ray luminosity characteristic of more massive rich Abell clusters (Burns, 1981). Two NATs were observed in group environments, where the low IGM density was believed to have allowed the jet to grow too quickly, thus lowering the ram pressure caused by the jet on the ICM ($\rho_{\text{jet}} v_{\text{jet}}^2$) (Doe et al., 1995), which is discussed in the next section. This was believed to be the modus through which all NATs and WATs would be bent in group environments.

## 1.1 Galaxies

From the time humanity first used the Sun, Moon and stars to discern time, the seasons and time of the month, astronomy has largely been an observational enterprise. In ancient times the naked eye was used and later on Galileo's telescope ushered in an era of assisted observations. With progress made in physics, these observations benefited greatly from the understanding of optics and provided the motivation, at least in part, for that improvement. This helped the finding of more stars and their classification in an attempt to understand them better.

The comparison of stars at this time was subjective until the introduction of photographic plates which made it feasible to make a more robust comparison of stellar fluxes. The discovery of spectroscopy, coupled with the more robust ability to compare fluxes, expanded the capacity to learn more about the fundamental characteristics of stars. The theoretical advances in physics further enriched astronomy as a Science and led to new questions which required better optical telescopes and instrumentation.

With William Herschel's discovery of the infrared light in 1800 leading to the birth of infrared astronomy three decades later, the window into the electromagnetic radiation produced by celestial bodies gradually opened wider. The first infrared observations of stars other than the Sun only came in the early twentieth century. Radio observations were to follow after the second world war and X-Ray observations in 1962. Some of the celestial bodies observed with optical telescopes were, unlike point-like stars, fuzzy or 'nebulous' in appearance.

The first dedicated catalogues of 'nebulae' were by Charles Messier in the 18th century and William Herschel in the early 19th century. The existence of extragalactic nebulae was postulated by Immanuel Kant in the late 18th century and was only confirmed more than a hundred years later when, with the use of spectroscopy, the radial velocity of M31 was determined by Vesto Slipher to be -300 $\mathrm{km\,s^{-1}}$ which was too high, suggesting that M31 may not be gravitationally bound to the Galaxy.

The discovery of other spiral nebulae with high radial velocities led to the Shapley-Curtis debate of 1921 which argued, on the one hand the size of the Milky Way, and on the other hand the existence of these spiral nebulae as the 'island universes' postulated by Kant that are external to the Milky Way. The result was inconclusive and further evidence was continually being sought to determine both the true extent of the Galaxy and the conclusive evidence that some of the nebulae were separate galaxies from the Milky Way.

This culminated in the 1924 work of Edwin Hubble, who used the measurements of the period-luminosity relation in Cepheids to find the distance to M33 to be 285 kpc. He found a similar result for M31, which meant that these spiral nebulae were indeed extragalactic Hubble (1926). With this, galaxy studies began to emerge as an independent study in astronomy. A long period of trying to improve the morphological classification of galaxies and assigning certain physical characteristics to the different morphological classes followed as the number of known galaxies in the Universe increased.

In the past decade or two, galaxy formation and evolution models have become more sophisticated, and have been one of the main focuses of research in extragalactic astronomy. They have involved the interaction of AGN feedback and star formation (Fabian, 2012; Combes, 2017). One of the key questions that is still subject to active research is how galaxies formed in the early Universe. The two major competing hypotheses are the hierarchical structure formation, which proposes that the massive galaxies seen today formed via the merger of smaller structures, and the monolithic formation process, that proposes galaxy formation through dissipational collapse of proto-galaxies (Fabian, 2012; Kravtsov & Borgani, 2012). The radio emission from AGNs, is confined to galaxies with older spheroidal populations.

### 1.1.1 Galaxy classification

A galaxy is a collection of stars, stellar remnants, dark matter, gas and dust bound together by gravity. This definition itself has evolved over time as more has been learnt about the Galaxy as well as others. In the beginning, when galaxies were being observed with photographic plates, it was Hubble (1926) who classified galaxies into ellipticals, spirals and barred spirals. Upon further study, the class of lenticular galaxies (type S0) as intermediate between ellipticals and spirals was introduced (Hubble et al., 2013). The sequence shown in Fig. 1.2 illustrates the different characteristics of elliptical, lenticular, spiral and irregular galaxies and how they were believed to evolve from one into the other at the time.

The general classes of elliptical, lenticular, spiral and irregular galaxies are discussed below. A final note on the historical development of the classification schemes is that there have been further additions to the Hubble classification scheme, geared towards streamlining it, based on additional findings, notably by including large-scale bar and ring structures (de Vaucouleurs, 1959; van den Bergh, 1960a,b,c; Elmegreen & Elmegreen, 1982).

#### Elliptical galaxies

Elliptical galaxies have a prolate spheroid shape with low ($\leq 1\%$) cold molecular gas content (Blanton & Moustakas, 2009). They are characterised by old stellar populations and a smooth surface brightness profile. The shape of their isophotes is characterised by the de Vaucouleurs

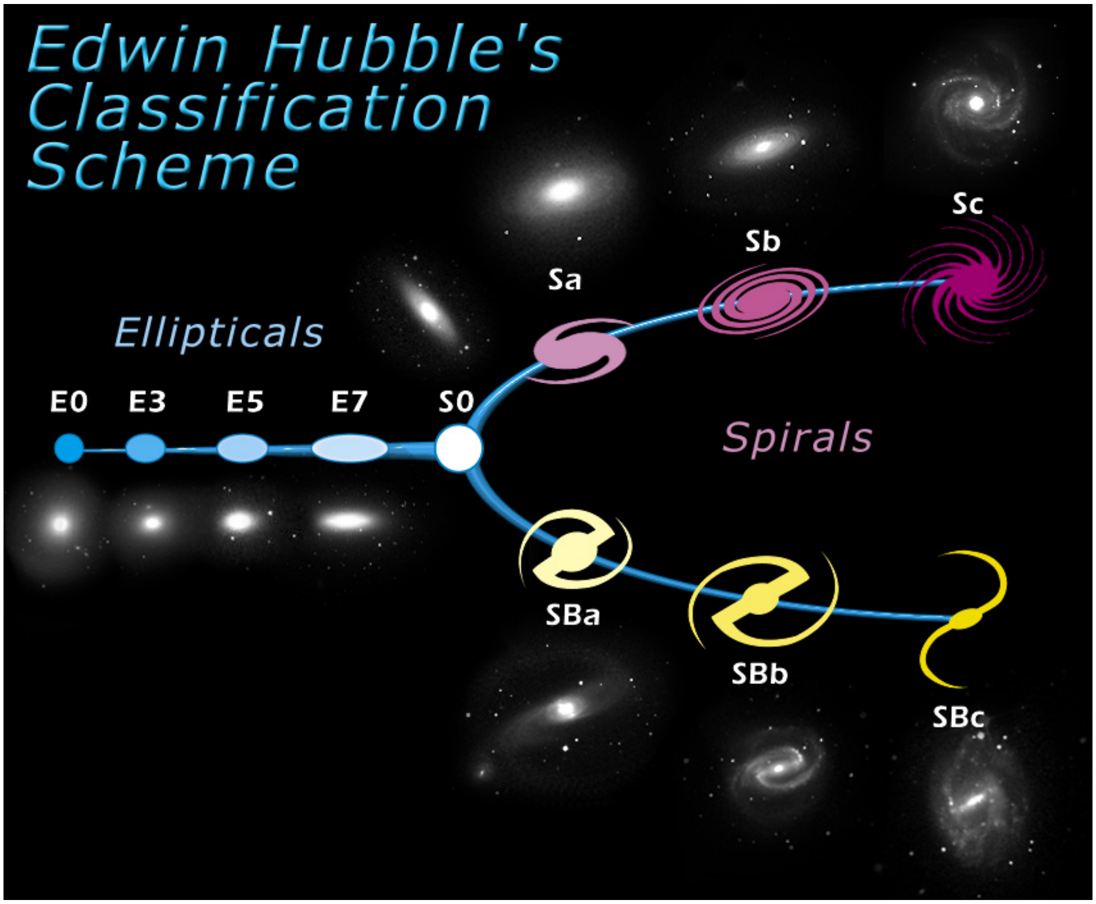

Figure 1.2: The Hubble tuning fork diagram showing the basic classification of galaxies into ellipticals, lenticulars, spirals and barred spirals. Image credit `https://www.spacetelescope.org/images/heic9902o/`.

profile (de Vaucouleurs, 1948), which is equivalent to a Sersic index of n=4 (Sersic, 1968). Together with lenticulars they are known as early-type galaxies (ETGs). This is due to their being listed first in the Hubble tuning fork diagram. They were initially believed to be free of gas and dust. However, this simplistic characterisation has been found to be inaccurate with improved telescopes such as the Hubble Space Telescope (HST). All early-type galaxy (ETG) shapes are supported by the random velocity anisotropy although they may be fast or slow rotators. Their spheroidal component dominates their surface brightness.

The age of the stellar population of ellipticals means that the redder G, K and M stars dominate the luminosity of these galaxies. They show no dust lanes and their shape is supported by random motions of the stars (Blanton & Moustakas, 2009). Their lack of activity with respect to star formation does not mean total dormancy, as these systems have relaxation times that are greater than the age of the Universe and are thus still dynamically active.

Dust and gas have been found in many of the ellipticals that were initially believed to be free of both. Faint dust lanes in ellipticals have sometimes been found oriented perpendicular to the major axis of the galaxy. Suffice it to say that some ellipticals have been mis-classified and the main difference between them and S0 galaxies is the lack of the dust lane that characterises S0s. The galaxy luminosity function shows that elliptical and lenticular galaxies are more numerous at stellar masses greater than $10^{10}$ $M_\odot$ (Blanton & Moustakas, 2009).

The largest galaxies in the Universe, which are found close to the cores of galaxy clusters and groups, are ellipticals. These also harbour the most massive SMBHs in the Universe because SMBH mass correlates with the mass of the spheroidal component of galaxies such as galaxy bulges. The other types of ellipticals are dwarf ellipticals and dwarf spheroidals which are less massive by several orders of magnitude.

### Lenticular galaxies

These are the other class of ETGs and are characterised by the presence of a dust lane that may be enveloped entirely by the spheroidal component. The spheroidal component of lenticulars (S0) shares the same characteristics as ellipticals and bulges of spirals. Hubble believed them to be an intermediate class between spirals and ellipticals and they sometimes show the presence of a bar structure (Sparke & Gallagher, 2006). The amount of dust present in S0 galaxies is less than the dust found in spirals (van Dokkum & Franx, 1995).

The variation of bulge to disc ratios suggests that lenticulars could have fundamental differences in how they are formed depending on their environments. For full reviews on lenticulars see Kormendy & Kennicutt (2004) and Kormendy & Ho (2013). The fraction of lenticulars in the local universe is approximately 20% of the total population of galaxies (Wilman & Erwin, 2012).

### Spiral galaxies

The structure of spiral galaxies is more complex than the elliptical and lenticular galaxies. Spirals usually have a bulge at their centres surrounded by a flat rotating disc which extends much further than the bulge component. Both components (bulge and disc) are surrounded by a spherical halo where globular clusters usually reside. The spiral arms are supported by rotation instead of the anisotropy of stellar motions that supports the bulge component and ETGs. The galaxy luminosity function shows that spiral galaxies are more numerous at stellar masses lower than $10^{10}$ $M_\odot$ (Blanton & Moustakas, 2009).

The disc contains stars, gas and dust. The spiral structure is believed to be a result of density waves in the disc or alternatively shock waves which give rise to a new generation of stars. This gives spiral arms their characteristic blue colour, arising from massive, hot stars. Spirals dominate the local universe where their populations have been estimated to be $\sim$67% of galaxies with stellar mass greater than the Milky Way galaxy.

The Hubble classification scheme, as visually presented in Fig. 1.2, groups spirals based on the spread of the spiral arms, the separation of the bulge with the arms, the bulge-to-disc ratio and the presence of bars (Sandage et al., 1975). Regular spirals are designated as (S) and barred spirals along their major axis are (SB). In both designations the scheme defines those with arms very near to a relatively large bulge as 'a' and the designation moves to 'b' and 'c' type spiral galaxies as the bulge becomes smaller whereas the arms are more well defined and stretched outwards (de Vaucouleurs et al., 1991). The surface brightness of spirals also follows the Sersic profile but with the galaxy concentration index, n, set to 1.

### Irregular galaxies

Irregular galaxies have no real symmetry and are neither bulge or disc dominated. They were originally left out of the Hubble classification system and were gradually introduced as the number of galaxies observed increased, culminating in the Hubble-de Vaucouleurs galaxy morphology scheme shown in Fig. 1.3. The motion of the stars in irregulars is highly stochastic with no rotational motion (Sparke & Gallagher, 2006). They generally contain the highest amount of gas which drives star formation. As a result, they have a very blue photometric colour due to a very young stellar population. They are one of the primary additions by de Vaucouleurs et al. (1991) to the Hubble-de Vaucouleurs classification scheme.

Irregulars are generally small in size compared to standard galaxies and have a mass range $10^8\ M_\odot \leq M_* \leq 10^{10}\ M_\odot$. They are sub-classified into gas rich, low metallicity type I irregulars

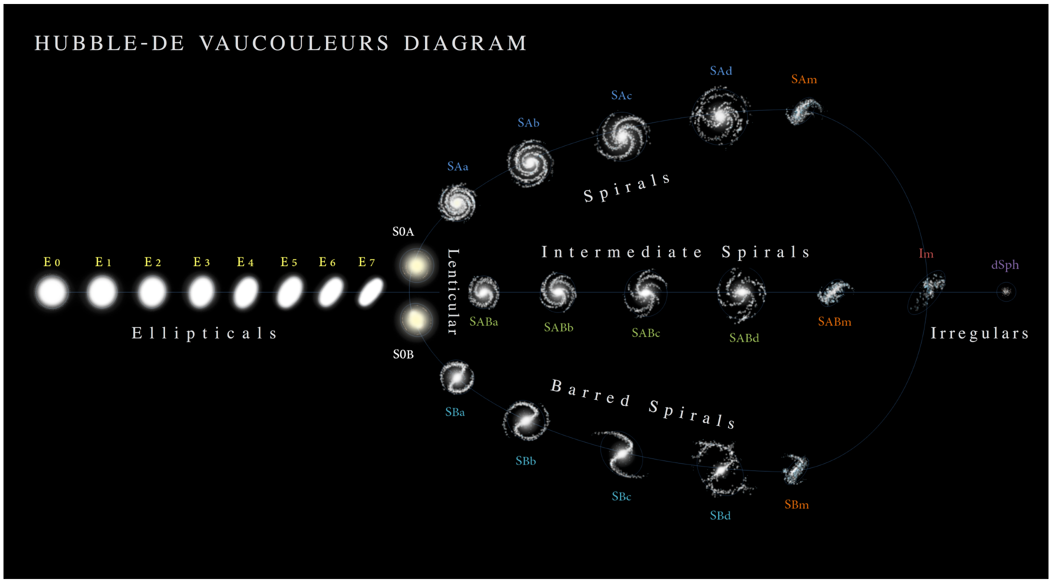

Figure 1.3: The Hubble-de Vaucouleurs galaxy classification diagram including the addition of new classes of barred lenticulars and irregular galaxies to ellipticals, lenticulars, spirals and barred spirals. Image credit: `https://en.wikipedia.org/wiki/File:Hubble-Vaucouleurs.png` by A. Ciccolella

and the chaotic, type II irregulars with high dust content. Type II irregulars are believed to be a result of recent galaxy-galaxy interactions or collisions.

### Peculiar galaxies

Peculiar galaxies are galaxies that have a shape, size, or content that is different from the normal ellipticals, spirals, and irregulars in the Hubble classification system. They often result from galaxy interactions, or sometimes show some other feature such as a jet emerging from the nucleus, low surface brightness or even unusual amounts of dust (Arp, 1966; Arp & Madore, 1987). They are designated 'p' or 'pec' in addition to their main classification type.

The two main types of peculiar galaxies are interacting galaxies and active galactic nuclei (AGN). The first type of peculiar galaxy are the interacting galaxies, which are those galaxies whose structure has been altered by the gravitational attraction of neighboring galaxies or have undergone galaxy-galaxy collision (Lynds & Toomre, 1976; Higdon et al., 2011). These include the special case of ring galaxies where a small galaxy collides nearly along the rotational axis with a larger spiral galaxy thus temporarily changing the appearance of the spiral galaxy (Lynds & Toomre, 1976; Higdon & Higdon, 2010). As the smaller galaxy passes through the disk of the spiral, its gravitation pulls in stars and interstellar material from the outer disk of the large galaxy and as it departs, this material moves back outward and triggers major star formation and the appearance of a ring.

When two large galaxies of similar masses interact, energy exchange between orbital motion and the motions of the stars in each galaxy will cause the two to approach each other resulting in a merger. Such a merger sometimes disrupts both galaxies in such a way that very little trace of the original structures of the merging galaxies remains. The resulting distribution in space of the stars in the formed galaxy will then have none of the standard morphologies in the de Vaucouleurs classification scheme.

The second group of peculiar galaxies are those whose appearances and characteristics have been modified by internal processes, mostly AGN activity (Arp, 1966). Spiral galaxies have interstellar medium (ISM) densities are higher than for elliptical galaxies. When AGN jets go off in the cores of spiral galaxies, as is the case in Seyfert galaxies, the galaxy core increases its luminosity and the ISM gets an energy injection that shocks the gas, heating it to high temperatures and stirring it simultaneously (Paliya et al., 2014). This is also coupled with a much higher degree of variability in the radiation of the galaxy as the radiation is produced within a relatively small region.

## 1.2 AGNs and SMBHs

BTRSs are AGNs with radio jets that extend up distances greater than 100 kpc, hence their study is based on the understanding of AGNs and SMBHs. The two largest groups of AGNs are Seyfert galaxies and quasars. Seyfert galaxies, named after their discoverer Carl Seyfert, were first defined as a class in 1943 (Seyfert, 1943). They are spiral galaxies whose core shows very high surface brightness and high ionisation spectral lines. Their core luminosity, found within 100 pc of the galaxy center, is comparable to the total luminosity of the whole galaxy. Their cores are also luminous at ultraviolet wavelengths similar to quasars. Unlike quasi-stellar objects (QSOs), whose stellar content or host galaxy is not visible in the optical observations, the stellar content of Seyfert galaxies in visible in optical observations. Their radio emission was first observed when Grote Reber observed the radio emission of Cygnus A (Reber, 1944).

The association of the quasar 3C 273 by Oke & Schmidt (1963) and 3C 48 by Matthews & Sandage (1963) with extragalactic optical sources was the first optical verifications of radio galaxies discovered with the third Cambridge radio catalogue (Edge et al., 1959). Their existence had already been known for about four years before redshift measurements placed them at redshifts that established them as extra-galactic sources. Thus, from its inception, the study of active galaxies lends itself to multiwavelength observations. The introduction of this new phenomenon took time to be accepted as a bona fide 'new' discovery until theory caught up with observations.

With Seyferts and quasars being verified as legitimate observations, other extra-galactic sources of electromagnetic radiation were found and the field of AGNs was well and truly on its way. The brightness of the quasars and their point-like appearance suggests a source smaller than a parsec harbouring more light than the entire galaxy. No known method of energy generation could achieve this at the time. Theoretical arguments followed soon, suggesting accretion onto a SMBH as the cause of the high luminosity (Zel'dovich, 1964; Lynden-Bell, 1969). It took a while longer to verify that the source of the energy released by the quasar was the accretion of matter onto a SMBH (Lynden-Bell, 1978; Soltan, 1982; Rees, 1984).

With this, SMBHs could be studied observationally as well as theoretically. This allowed for the testing of the theoretical framework of SMBHs. The widespread use of charge-coupled device (CCD) technology made it possible to study blackholes in general and SMBHs in particular because variability studies could be used to infer the size of the source of radiation. The field grew to be a major astrophysical frontier after the building of the Hubble space telescope (HST) and the adaptive optics (AO) technologies for ground-based telescopes.

### 1.2.1 SMBHs

A simple definition of a blackhole as a region of space where the gravitational force is so large that even light cannot escape encapsulates the most obvious aspects of blackhole observation without revealing their most interesting characteristics and their importance to the understanding of physics. Blackholes show consistent behaviour despite a mass range that spans nine orders of magnitude. This is one of the most active fields of study in both theoretical physics and observational astronomy.

The mathematical existence of blackholes is a direct result of Einstein's field equations. Schwarzschild

(1916) solved them by assuming spherical symmetry of an uncharged, time-independent, non-rotating compact object. This Schwarzschild metric was, for a period of almost 50 years, the only known solution to Einstein's field equations. Kerr (1963) found a different approach to attain symmetries in the Einstein's field equations by assuming shear-free geodesics, time-independence and symmetry along the rotational axis of a spinning compact object. The Kerr metric was the kind of improvement on the Schwarzschild metric that allowed for the modelling of more realistic blackhole characteristics.

Kerr blackholes are considered the more realistic representation of the concept of blackholes because at their formation, blackholes have the angular momentum of an extended object concentrated within a small volume which generally calls for rapid rotation of the blackhole. Blackholes have three fundamental properties viz. mass, spin and charge.

Three types of blackholes have emerged from observational Astronomy. The most prevalent type are Galactic or stellar mass black holes. These are the end result of the evolution of massive stars ($M > 18$ $M_\odot$.) They are found all over the Galaxy as well as in other galaxies. Most of these stellar mass black holes are dormant because there is not much accretion onto them. The second kind have only been actively sought through telescope surveys recently. These are called intermediate mass black holes (IMBHs) and are believed to have masses of the order $10^5$ $M_\odot$. They are found at the cores of globular clusters. IMBH are too far and too small to be easily observed outside the Galaxy using current telescopes. They are thus surveyed using the same techniques as Galactic black holes. The third kind are SMBHs and they are one of the cornerstones of the study of BTRSs. The study of IMBHs is still in its early stages and it is not known yet if they co-evolve with their host globular clusters in a similar way that SMBHs are believed to co-evolve with their host galaxies.

SMBHs are found at or near the centres of almost all, if not all, massive galaxies (Magorrian et al., 1998; Gebhardt et al., 2000; Ferrarese & Merritt, 2000). This suggests that the majority of these galaxies have passed through an AGN phase during their evolutionary history. There is a belief, gaining more credence, that they may have co-evolved with their host galaxies. There are numerous correlations between the mass of the SMBH and galaxy properties in particular for Bulges and ETGs (Kormendy & Richstone, 1995; Magorrian et al., 1998; Gebhardt et al., 2000; Ferrarese & Merritt, 2000; Marconi & Hunt, 2003). These suggest that the influence of the SMBH may not just be gravitational, but more fundamental in shaping the evolution of the galaxy.

### 1.2.2 SMBH masses: measurement techniques.

The history of blackhole mass ($M_{\rm BH}$) measurements is dominated by the improvements in the technology and the modelling methodology for this field of study. The initial major contribution to improved SMBH demographics was provided by the availability of the HST with its improved spatial resolution. This made possible the confirmation of earlier ground-based detection of SMBHs, thus ushering in the next era of SMBH mass measurement.

After the HST era, the ground based AO assisted telescopes such as the European Southern Observatory's Very Large Telescope (ESO VLT) and the Gemini multi-object spectrograph (GMOS), with their integral field units (IFU), were the next step. They offered improved sensitivity due to their 8 m diameter mirrors and high spatial resolution due to AO. The IFU offered the added benefit of 2-dimensional spectral evaluation of the field-of-view (FoV).

SMBHs have masses of the order $10^6$ $M_\odot \leq M \leq 10^{10}$ $M_\odot$. SMBHs with masses greater than $10^{10}$ $M_\odot$ have been measured in the local Universe but they are a high mass exception. A calculation of the energy released in growing SMBHs is greater than the host galaxy's binding energy. This suggests that the growth of the SMBH could blow the gas out of the galaxy, thus quenching star formation as well as the growth of the galaxy (Silk & Rees, 1998).

The reverberation mapping (RM) method has been used to directly measure the masses of approximately 50 SMBH masses in the local Universe. This has an error of $\approx$ 0.3 dex and is used in the optical and NIR wavelength ranges. This technique works by measuring the time delay between an increase in the luminosity of the accretion disc of an AGN and the increase in the emission line luminosity of a broad-line region (BLR) gas (Peterson, 2001). From this, a distance between the SMBH and the BLR can be inferred and the width of the spectroscopic H$\beta$ emission line of the BLR gives the kinematics of the BLR gas (Peterson & Horne, 2004).

Another method that has been successfully used to directly measure blackhole masses in the optical and NIR wavelength range has been the modelling of SMBH mass using data from AO assisted IFUs. These have been used to confirm the SMBH masses for measurements constrained with HST observations. This is now getting superseded by the modelling SMBH mass using CO observations from the Atacama large millimeter array (ALMA) telescope. The ALMA CO observations of AGN cores can map the gas motions with better sensitivity and resolution than the current optical and near-infrared IFU instruments.

### 1.2.3 Gas kinematics vs stellar dynamics

The measurement of SMBH mass relies on calculating the difference between the dynamics of the mass of the bulge or elliptical galaxy and the kinematics at the core of the galaxy. This difference is assumed to be due to the gravitational force generated by the SMBH. At parsec scales, the motion of stars around a SMBH is random, giving rise to a velocity dispersion, whereas the motion of the gas at these scales is usually in a Keplerian disc or in the dusty torus.

#### Ionised gas dynamical modelling

Almost all disc galaxies and more than half of S0 and elliptical galaxies have a detectable amount ($10^4\,\mathrm{M}_\odot - 10^5\,\mathrm{M}_\odot$) of warm ($10^4\,\mathrm{K}$) gas in their cores (Ho et al., 1997). Emission lines from this gas, such as H$\alpha$ and H$\beta$, have simple line profiles and large equivalent widths and generally have better S/N ratios than the absorption lines due to stellar dynamics (Kormendy & Ho, 2013). However, this warm gas is ionised and this has an additional effect on the line width caused by the thermal doppler effect. Difficulties in inferring the contribution of the gravitational potential are discussed later in this section.

Gas kinematics are the easiest way to trace the gravitational potential around the SMBH. Kinetic velocities of atomic gas, such as hydrogen, in Keplerian circum-nuclear discs can be measured from the widths of the emission line profiles. These kinematic velocities provide a measure of the SMBH mass. This method depends on having thin gaseous discs in equilibrium, which, because the gas is susceptible to non-gravitational forces such as turbulence and outflows or inflows, is not always the case. This affects the broadness of the measured emission line profiles which has an effect on the reliability of the SMBH measurements. This method is applied to high resolution HST data, but, because of the problems mentioned above, it is only considered reliable as an upper limit to the measured SMBH mass.

### Reverberation mapping

The RM technique (Blandford & McKee, 1982) is based on the assumptions that the motions of BLR gas clouds of AGNs are dominated by gravity and that the inner parts of the accretion disc around the SMBH produce UV radiation that photoionises the gas clouds. The time lag $\tau = r/c$, between changes in luminosity of the accretion disc and emission line luminosities is due to the time it takes light to travel the distance $r$ between the accretion disc and the BLR.

The velocity widths $\Delta V$ of the emission lines trace the virial velocity which is related to the SMBH mass by the virial theorem, given by

$$M_{\mathrm{BH}} = f\frac{(\Delta V)^2 r}{\mathrm{G}} \ , \tag{1.1}$$

where $G$ is the gravitational constant and $f$ is a factor that incorporates all the uncertainties in the BLR model. Currently, the value of $f = 5.2 \pm 1.2$ is calibrated from the measured RM of SMBH masses (Gültekin et al., 2009).

The calibration of $f$ has an added complication that whereas bulges scale with $M_{\mathrm{BH}}$, pseudobulges do not. The number of pseudobulges in the RM method sample may introduce a systematic error in the estimates for $f$.

### Molecular gas dynamics

In some galaxies, the circum-nuclear gas is molecular rather than atomic. This means it is cooler and less susceptible to turbulence except at distances very close to the SMBH. The molecular gas radiates at sub-millimeter wavelengths which can be observed using interferometric techniques. ALMA has an angular resolution that is an order of magnitude smaller than the best current optical and NIR telescopes.

This method has provided the most accurate SMBH mass measurements thus far (Davis et al., 2013). It requires the presence of molecular gas in the nuclear regions of AGNs, which is rare in massive galaxies. Most of the problems that affect ionised gas dynamical measurements apply to a lesser extent to molecular gas dynamics.

In some fortuitous circumstances, such as NGC 4258 and NGC 5793, $H_2O$ masers are found in these molecular discs. These environments are usually highly obscured and are thus impossible to resolve with optical photometry and spectroscopy. This makes the usage of $H_2O$ masers the only method that can measure kinematics around the SMBH in such cases. Because these masers occur in the radio regime, they can be observed using interferometric techniques which allows the positions of maser spots to be determined to milliarcseconds accuracy. These maser lines tend to be narrow, which allows for an accurate determination of their velocity. The high amplification factors of maser emission allows these spots to be detected way beyond the capabilities of other telescopes.

The SMBH mass measurement by maser dynamics has an improved accuracy and resolution than the majority of the measurement techniques. It relies on the study of the Keplerian rotation curve of $H_2O$ maser emission in molecular gas discs around the SMBHs of AGNs (Miyoshi et al., 1995; Zhao et al., 2018). Its angular resolution can reach a few milliarcseconds under the right conditions, which improves the dynamic range of these measurement techniques.

This method may only be applied to gas-rich galaxies and, in general, ETGs are gas-poor. Care must be taken when employing this method, because, in cases where the masses of the discs harbouring the maser are comparable to the mass of the SMBH or when there is a nuclear star cluster that is sufficiently massive, it might over-estimate the SMBH mass.

### Individual stellar motions

If individual stars in orbit around a SMBH can be resolved, then by observing them over a sufficiently long time span, their orbital period and semi-major axis can be measured. By applying Kepler's third law, the mass of the SMBH can determined.

The only SMBH for which this technique is currently feasible is Sgr $A^*$ in our Galaxy, which is our nearest SMBH. For other galaxies in the Local group, such as M 33, the upper mass limit of a possible SMBH was determined but there was not enough spatial resolution in the spectra to determine the presence of the SMBH without doubt. The stars are within a parsec of Sgr $A^*$ and have velocities that range from about $10^2 - 10^3\,\mathrm{m\,s^{-1}}$. Ghez et al. (2008) used the Keck telescope and Genzel et al. (2010) used the VLT, both of which were equipped with AO technology, to measure the mass of the Galactic SMBH to be $M_{\mathrm{BH}} = 4.30 \pm (0.36) \times 10^6\,\mathrm{M}_\odot$. The uncertainty in the SMBH mass measurement is dominated by the uncertainty in the distance to Sgr $A^*$.

## 1.3 AGNs

For historical reasons, the observed AGN population is classified based on observational properties of its members. This gives rise to a problem where the classification is more historical than pragmatic. Initially the classification was observational and thus did not necessarily help differentiate the underlying physical processes. This is compounded by the fact that each observational wavelength regime has tended to name the AGN types based on their particular requirements. This has sometimes led to members of the same optical AGN class being of different classes in the X-ray and with another new set of criteria in the radio regime. This was solved by introducing the unified theory of AGNs, which described them based on the observer's point of view of the inclination angle to the AGN.

AGNs are classified based on the presence of at least one of the following observed properties,

- compact nuclear region much brighter than a region of the same size in a normal galaxy
- non-stellar (non-thermal) continuum emission
- strong emission lines
- presence or absence of a jet
- variability in continuum emission and/or in emission lines on relatively short time scales

AGNs are considered radio-loud when they have a ratio of 5 GHz luminosity to B-band luminosity that is greater than 10, which occurs when they have a radio jet. Some fraction of AGNs are radio-loud. The prevalence of radio-loudness in AGNs is very dependent on the stellar mass of the host. Best et al. (2005) showed that the fraction of radio-loud AGNs with 1.4 GHz luminosity $> 10^{23}\,\mathrm{W\,Hz^{-1}}$, the fraction of radio-loud AGNs is nearly zero for host galaxies of stellar mass of $10^{10}\mathrm{M}_{\odot}$ and rises to above 30% for host galaxies of mass $> 5 \times 10^{11}\mathrm{M}_{\odot}$.

### 1.3.1 AGN jets

Jets appear in three scales in Astrophysics viz, sub-parsec scale, parsec scale and kiloparsec scale. Sub-parsec scale jets are found in solar mass type black hole systems, sometimes called micro-quasars, where the gravitational potential well is enough to create jets whose length ranges from

Astronomical Unit (AU) scale to a fraction of a parsec. Parsec scale jets have lengths that range from a parsec to a few hundred parsecs and are found in SMBH mass type systems in the cores of AGNs. They are found to be constrained within their host galaxies. Kiloparsec scale jets are also found in SMBH mass type systems in the cores of AGNs but their length scales range from several kiloparsecs to more than a megaparsec.

An Astrophysical jet system consists of a blackhole, an accretion disc, a torus (in the case of AGN jets) and a relativistic jet (Antonucci, 1993). It is formed by material falling onto a blackhole.

### 1.3.2 Unification Scheme

The presence of a dusty torus at the center of the host galaxy of an AGN can explain the difference between type-I and type-II AGNs by invoking a few simple assumptions (Netzer, 2015). This unification scheme is called the IR-optical-UV-X-ray unification scheme. Type-I AGNs have a bright, central non-stellar point-source radiation that is visible in a broad wavelength range and broad ($10^3\,\mathrm{kms^{-1}} - 10^{4.3}\,\mathrm{kms^{-1}}$) permitted and semi-forbidden emission lines and generally do not show narrow emission lines. Typer-II AGNs, on the other hand contain strong narrow emission lines ($< 10^3\,\mathrm{kms^{-1}}$). They show clear signs of photo-ionization by a non-stellar radiation source.

The radio unification scheme also invokes, in addition to the dusty torus, a relativistic jet. This combination is found in 10% of all high-ionization AGNs. The jet is aligned with the symmetry axis of the SMBH and torus system and is launched close to the SMBH (Urry, 2003; Tadhunter, 2008). The radio unification scheme has been used to predict compact and extended radio AGNs.

### 1.3.3 The bending equation

The degree of the bending of NATs and WATs due to ram pressure is governed by the bending equation which depends on the jet velocity, galaxy velocity with respect to the ICM, jet density and the density of the ambient medium.

The bending equation arises from the analytical solution of the conservation of momentum, mass and energy equation of the jet in the ICM

$$\frac{\partial v_{\mathrm{jet}}}{\partial t} + (v_{\mathrm{jet}}.\nabla)v_{\mathrm{jet}} = \frac{1}{\rho_{\mathrm{jet}}}\nabla P \ , \tag{1.2}$$

assuming time independence (De Young, 1991; Freeland & Wilcots, 2011). It yields

$$\frac{\rho_{\mathrm{jet}} v_{\mathrm{jet}}^2}{R_{\mathrm{bend}}} = \frac{\rho_{\mathrm{ICM}} v_{\mathrm{gal}}^2}{R_{\mathrm{P}}} \ , \tag{1.3}$$

where $\rho_{\mathrm{jet}}$ is the density of the jet, $v_{\mathrm{jet}}$ is the velocity of the jet, $\rho_{\mathrm{ICM}}$ is the density of the ICM, $v_{\mathrm{gal}}$ is the velocity of the galaxy, $R_{\mathrm{bend}}$ is the radius of curvature of the deflected jet and $R_{\mathrm{P}}$ is the pressure scale height of the jet material (the radius of the jet is used as the pressure scale height, which is useful when comparing the observability of the jet curvature given the width of the jet) (Burns & Owen, 1980; O'Dea, 1985; Jones & Owen, 1979; Begelman et al., 1979). It is the model that is used to determine where NATs and WATs are likely to be found in the Universe. Fig. 1.4 shows the difference in appearance between NATs and WATs as discussed in the introduction of this chapter. It is notable that close to the galaxy core NGC 1265 looks like a WAT and with a better resolved tail of the jets, the true opening angle is revealed. The observed environments of WATs and NATs are discussed below.

### 1.3.4 NATs

(O'Dea & Owen, 1985) used the very large array (VLA) radio telescope at 1.4 GHz to study NATs to discern global properties that could be used to define the group. They found several correlations that were consistent with the hypothesis that NAT jets are bent by the interaction of their radio luminous plasma with the ICM (Miley et al., 1972). O'Dea & Owen (1985) found a bi-modal distribution of NATs in their sample. The two groups are NATs whose length was 15 kpc $\leq$ length $\leq$ 50 kpc that showed a correlation between the integrated power at 1.4 GHz and the length of the radio jets and a small number (4 NATs) of powerful sources that had a length $\geq$ 100 kpc. There were no intermediate length sources of 50 $\leq$ length $\leq$ 100 kpc that suggested a continuum distribution of jet lengths (O'Dea & Owen, 1985). The shorter length jets were all found, with the VLA resolution, to be still expanding within the ISM of their respective galaxies.

Venkatesan et al. (1994) found NATs to also reside in poor Abell clusters where the radial velocity of the galaxy is less than 300 $\mathrm{km\,s^{-1}}$. These results were consistent with O'Dea & Owen (1985) where the lowest radial velocities of NATs hosts in the poorest Abell clusters were also lower than 300 $\mathrm{km\,s^{-1}}$. Such low radial velocities would cause jet bending only in extremely dense environments. The poor clusters are also not known to possess high densities. Other possible causes for bending due to ICM motion would be galaxy infall. That would cause a particular galaxy to have a higher relative velocity than the circular velocity the cluster mass can cause Venkatesan et al. (1994).

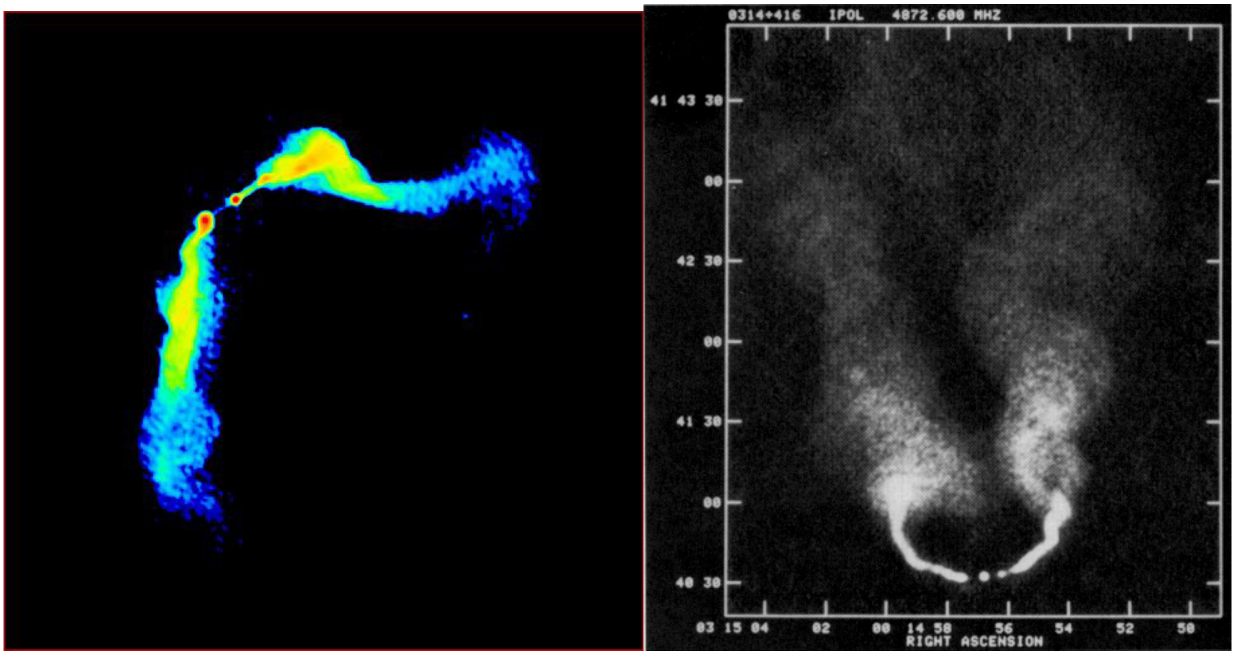

Figure 1.4: Images of the WAT galaxy 3C 465 (Left) and the NAT galaxy NGC 1265 (Right). The opening angle between the opposite jets in both is the reason they are termed wide and narrow. Images are taken from O'Dea & Owen (1986); Owen & Rudnick (1976)

### 1.3.5 WATs

WATs were first defined as a class by Owen & Rudnick (1976). The study of extragalactic radio jets was still in its early stages at the time. Their study was largely to separate the different opening angles observed in tailed galaxies. Their sample of six WAT galaxies suggested that WATs were found in Abell Clusters of all classes and that they showed a strong tendency to be associated with the BCG (Owen & Rudnick, 1976).

O'Donoghue et al. (1993) further defined the class using a sample of 11 VLA galaxies in 6 cm and 20 cm radio wavelength observation. They also compared the adiabatic and the kinetic flow dynamics that could be responsible for jet bending. O'Donoghue et al. (1993) found WATs to generally share the following observational characteristics that include the Owen & Rudnick (1976) definition,

- They have a characteristic C-shape morphology that begins at the hotspot.
- They are large structures that extend beyond 50 kpc.
- Preferentially found in galaxy clusters without cooling cores.
- Found close to the core of the cluster where the space velocity of the galaxy is low.
- Show a distinct jet-hotspot transition, where the jet suddenly goes from being narrow and faint to being broader and brighter. That transition is neither found in FR I or FR II radio galaxies.
- They have radio power close to the FR I/FR II break.

O'Donoghue et al. (1993) compared the kinetic and the adiabatic models of jet flows and their abilities to fully explain the dynamics of radio jets. They found that they both did not sufficiently account for jet bending and that at most, each model would only be partially applicable to the jet dynamics. They found that there are other models that might be more suitable to explain the behaviour of AGN jets.

The kinetic model assumes that the radio luminosity is caused by the conversion of some kinetic energy flux of the jet into radiation (Eilek et al., 1984). The kinetic model leads to much higher average jet velocity due to the less dramatic deceleration of the jets at the beginning stages. The slow decay of the velocity field of the jet necessitates an artificial numerical method of ensuring the jet velocity of zero at the end of the jet tail (O'Donoghue et al., 1993).

The adiabatic model assumes an absence of buoyancy forces and that the radio luminosity of the jet is solely due to the acceleration of relativistic electrons from the central SMBH engine. The magnetic field and the flow thermal energy are assumed to play no part in re-accelerating the electrons in the jet. O'Donoghue et al. (1993) found that the initial velocity of the jet must be close to 0.2 c for feasible radiative efficiency.

In both models the deceleration of the jet is assumed to be caused by the entrainment of the ambient matter by the jet. The adiabatic model was found to result in electron travel times that were about an order of magnitude larger than the travel times calculated from spectral aging. This was a similar result to 3C 75 found by Owen et al. (1985). This could only be mitigated by modelling the presence of strong magnetic fields in the jet cocoons, which implies that the kinetic energy flux is not the only source of radio power in AGN jets (O'Donoghue et al., 1993).

### 1.3.6 Blackhole mass correlation with the Sersic index

The increased numbers of optical galaxy surveys provides more than $10^6$ images of galaxies in low to medium redshift. There is a correlation between the Sersic index and the SMBH mass in elliptical galaxies and bulges of lenticular and spiral galaxies in the local Universe. This correlation has found extensive use as a way of compiling SMBH samples from photometric data. The measured distances, SMBH masses and Sersic indices lead to the measurement of the correlation between $M_{\rm BH}$ and the Sersic index $n$. This was found to be

$$\log\left(\frac{\mathrm{M_{BH}}}{\mathrm{M_\odot}}\right) = (7.98 \pm 0.09) + (3.70 \pm 0.46)\log\left(\frac{\mathrm{n}}{3}\right) - (3.10 \pm 0.84)\left[\log\left(\frac{\mathrm{n}}{3}\right)\right]^2 , \tag{1.4}$$

which has an absolute scatter of 0.31 dex (Graham, 2007).

This quadratic relation, when extrapolated, predicts a lower-bound of $10^3\,\mathrm{M_\odot}$ SMBH masses for dwarf elliptical galaxies with a Sersic index of n=0.5 as well as the upper limit of $1.2\times10^9\,\mathrm{M_\odot}$ for the most massive ellipticals. The highest mass galaxies have SMBH masses greater than the predicted value by up to an order of magnitude, whereas the intermediate mass blackholes (IMBH) are believed to be of the order $10^3 - 10^5\,\mathrm{M_\odot}$ and have recently been observed in dwarf ellipticals (Mezcua et al., 2016; Koliopanos et al., 2017; Graham & Soria, 2019; Graham et al., 2019). Also, these predictions are found to disagree with the local blackhole mass function (Shankar, 2009). This leads to a need for more SMBH mass measurements as well as a close look at whether other correlations lead to similar conclusions.

## 1.4 $M_{\mathrm{BH}} - M_{\mathrm{bulge}}$ relation

The $M_{\mathrm{BH}} - M_{\mathrm{bulge}}$ relation was the first sign suggesting that the influence of the SMBH went beyond its gravitational sphere of influence. It is a photometric relation because the measure of bulge mass can be achieved by applying a mass to light ($M/L$) ratio to bulge luminosity. Shirakata et al. (2016) found the $M_{\mathrm{BH}} - M_{\mathrm{bulge}}$ relation at $z = 0$ to be consistent with seed black hole masses that are either of the mass $10^3\ \mathrm{M}_\odot$ or have a random distribution of SMBH masses in the range $10^3\ \mathrm{M}_\odot - 10^5\ \mathrm{M}_\odot$.

Dressler & Richstone (1988) were the first to note a relationship between SMBH mass and the luminosity of the spheroid of the host galaxy. This was based on M31 and M32 whose SMBH mass ratio was $\simeq 10$, which is closer to the ratio of their spheroidal component luminosity $\simeq 15$ than it is to the ratio of their total luminosity ($\simeq 70$) (Kormendy & Ho, 2013). This was further bolstered with a five member sample of Dressler (1989). By using the mass-to-light ratio ($\Upsilon$) this was transformed into the $M_{\mathrm{BH}} - M_{\mathrm{bulge}}$ instead of luminosity.

The jump from $L_{\mathrm{bulge}}$ to $M_{\mathrm{bulge}}$ is not a simple one. A straightforward approach would be to multiply the bulge magnitude with a $\Upsilon$ ratio that corresponds to the observed band. This would ostensibly avoid the problem of the different wavelength bands having different $\Upsilon$ values. The other challenge is that not all wavelength bands are suitable for stellar mass determination. Due to dust extinction, the shorter wavelengths are poor indicators of stellar mass.

This leads to the K-band being the most used wavelength window for the $M_{\mathrm{BH}} - L_{\mathrm{bulge}}$ relation due to its smaller scatter of 0.31 dex (Tremaine et al., 2002). The relation, using the K-band magnitudes of the bulge, goes as

$$\log\left(\frac{M_{\mathrm{BH}}}{10^9 M_\odot}\right) = -(0.266 \pm 0.052) - (0.484 \pm 0.034)(M_{\mathrm{K,bulge}} + 24.21)\ . \tag{1.5}$$

Even with the K-band and its advantage of insensitivity to dust extinction and stellar population age, the $\Upsilon$ values of old stellar populations of the type found in bulges and ETGs are uncertain (Kormendy & Ho, 2013). Such uncertainties are introduced by e.g. the poorly known initial mass function (IMF) of stars which may vary from one galaxy to the next. Even at different radii within the same bulge (Graves & Faber, 2010), the effects of the age and metallicity distributions of a stellar population are difficult to disentangle and therefore negatively affect the ability to constrain the late stages of stellar evolution like the asymptotic giant branch (AGB) (Portinari

& Into, 2011) and the effect of dark matter on $\Upsilon$ in different galaxies and at different radii within a galaxy. Graham & Scott (2015) and Fontanot et al. (2015) found that there are mechanisms through which the $M_{\rm BH} - M_{\rm bulge}$ relation could have a quadratic slope, while Schutte et al. (2019) found that extending the relation to dwarf galaxies and their SMBH masses below $10^5$ $\rm M_\odot$, was consistent with the relation for high mass galaxies. The $M_{\rm BH} - M_{\rm bulge}$ relation seems to be robust to higher redshifts e.g ($0.5 < z < 1.2$) (Schramm & Silverman, 2013) which shows that the field could benefit from more SMBH mass measurements, particularly at the low mass end.

Graves & Faber (2010) conclude that stellar population age and metallicity account for $\sim$1/4 of the variation in $\Upsilon$, whereas dark matter and IMF uncertainties are responsible for the rest. The matter is still subject to contentious debate, with some showing that the K-band mass to light ratio ($\Upsilon_{\rm K}$) can vary by a factor of $\simeq 4$ among galaxies due to IMF variations (Conroy & van Dokkum, 2012) and others contending that the IMF varies little from from one galaxy to the other (Bastian et al., 2010). Thus $\Upsilon_{\rm K}$ is by no means a perfect fit for old stellar populations, as Schulze & Wisotzki (2011) found a range of more than an order of magnitude in $\Upsilon_{\rm K}$ values in a sample of 12 ETGs that included the effects of dark matter.

Galaxy formation studies use stellar luminosity instead of the eqn. (1.5) format. The conversion of the relation in Tremaine et al. (2002) translates to

$$\frac{M_{\rm BH}}{10^9 \rm M_\odot} = (0.542^{+0.069}_{-0.061}) \left(\frac{L_{\rm K,bulge}}{10^{11} L_{\rm K,\odot}}\right)^{1.21\pm0.09} . \qquad (1.6)$$

The $\Upsilon_{\rm K}$ values can vary from e.g. 0.31 for NGC 3384 to 1.94 for NGC 4649 (Marconi & Hunt, 2003), so a reliable calibration factor is necessary for use in conversion to $\rm M_{K,bulge}$.

Into & Portinari (2013) find $\Upsilon_{\rm K}$ to have a steep dependence on both the colour (B - V) and the velocity dispersion at the effective radius $\sigma_{\rm e}$, which is the region that encloses half the luminosity of the galaxy. This allows for better calibration of $\Upsilon_{\rm K}$ to convert bulge luminosity into bulge mass, as well as a comparison between the $M_{\rm BH} - L_{\rm bulge}$ and the $M_{\rm BH} - \sigma$ relations.

## 1.5 $M_{\rm BH} - \sigma$ relation

This relation, despite its being more costly in telescope time than $M_{\rm BH}$ - $\rm M_{K,bulge}$, has received the most attention of all the SMBH mass - host galaxy relations. Its scatter is marginally better than $M_{\rm BH}$ - $\rm M_{K,bulge}$ relation but it was the first direct evidence of a correlation between SMBH mass and the host galaxy's gravitational potential well (Shankar, 2009). It suggests a co-evolution of galaxies and their SMBHs and has become an integral part of galaxy evolution, galaxy mass and galaxy feedback studies.

After M32 became the first SMBH dynamical discovery (Tonry, 1984, 1987), there were very few other galaxies whose SMBH sphere of influence (SOI) could be resolved with ground-based telescopes. The availability of HST data increased the number of secure dynamically measured SMBHs to seven (Kormendy & Richstone, 1995).

The $M_{\rm BH} - \sigma$ relation was first independently proposed by Gebhardt et al. (2000) and Ferrarese & Merritt (2000) respectively as

- $M_{\rm BH} = 1.2 \times 10^8 \rm M_\odot \left(\frac{\sigma_e}{200\ km\,s^{-1}}\right)^{3.75}$
- $\log M_{\rm BH} = 4.80(\pm 0.54) \log\sigma_{\rm c} - 2.9(\pm 1.3)$

where $\sigma_{\rm e}$ is the aperture line-of-sight velocity dispersion (LOSVD) within the effective radius and $\sigma_{\rm c}$ is velocity dispersion corrected to the aperture of one eighth of the effective radius.This is considered to be a more fundamental relation than the virial mass estimator (VME) method of McLure (2003) due to its tighter correlation of ($\simeq 0.3\,$dex) over three orders of magnitude of SMBH mass, compared to the VME method dispersion of 0.5 dex. The error of 0.3 dex is consistent with measurement errors (Gebhardt et al., 2000).

Both the Gebhardt and the Ferrarese experiments, despite the slight disagreement in the result, were in agreement about the practical importance of the relation due to its implication that SMBH growth and bulge growth are closely linked, as well as the ability to deduce SMBH mass from easy observational measurements. No sufficient evidence to suggest that there has been an evolution of the $M_{\rm BH} - \sigma$ relation has been found in the redshift range $0.03 < z < 1$ (Sexton et al., 2019; Shen et al., 2015). There is also no evidence of a difference between the relation between Type 1 AGNs and Type 2 AGNs as well as inactive galaxies.

Subsequent studies of the $M_{\rm BH} - \sigma$ relation using larger samples have not given a much different result from the initial results Kormendy & Ho (2013). The latest endeavours have acted to streamline the measurements and separate bulges from pseudo-bulges[1] as well as ameliorate other measurement challenges such as signal-to-noise (S/N) ratio. It was also found that an improperly determined effective radius of an ETG or bulge may bias the $\sigma$ low. This effect is lessened by using IFU data and thus still affects a lot of the literature values of $\sigma$.

### High mass end of the $M_{\mathrm{BH}} - \sigma$ relation statistics

Lauer et al. (2007) assert that the curvature of the $\sigma - L$ relation for massive ETGs implies the $M_{\mathrm{BH}} - \sigma$ relation is unlikely to be adequately represented by a single power law. This is in line with the results of Bayesian analysis of the Tremaine et al. (2002) sample done by Wyithe (2006) which found that a log-quadratic fit is a better representation of the $M_{\mathrm{BH}} - \sigma$ correlation than a log-linear fit. Massive ETGs represent the high mass end of these samples and thus form the bulk of the galaxies responsible for the deviation from the single power law. There is still a need for more high mass measurements of SMBHs to confirm and constrain this deviation.

This led to the investigation of the demographics of the high mass end of the $M_{\mathrm{BH}} - \sigma$ relation. Hu (2008) did a detailed re-investigation of these galaxies and found that the following equation holds for elliptical galaxies

$$\log\left(\frac{\mathrm{M_{BH}}}{\mathrm{M_\odot}}\right) = (8.28 \pm 0.05) + (4.06 \pm 0.28)\log\left(\frac{\sigma_*}{200\ \mathrm{km\,s^{-1}}}\right)\ , \tag{1.7}$$

where $\sigma_*$ is the stellar velocity dispersion and $M_{\mathrm{BH}}$ is the SMBH mass. Core ETGs and pseudo-bulges showed significant departures from this relation. This may suggest different formation histories for the two groups.

Tremaine et al. (2002) gives an $M_{\mathrm{BH}} - \sigma$ relation of

$$\log\left(\frac{\mathrm{M_{BH}}}{10^9\mathrm{M_\odot}}\right) = -(0.510 \pm 0.049) - (4.377 \pm 0.290)\log\left(\frac{\sigma}{200\ \mathrm{km\,s^{-1}}}\right)\ . \tag{1.8}$$

The SMBH mass of a potential simulated galaxy is inferred based on the simulated galaxy mass using the $M_{\mathrm{BH}} - \sigma$ as well as the other relations. This is useful when one is comparing observed AGNs and BTRSs with galaxies in cosmological simulations.

---

[1] Unlike classical bulges, pseudo-bulges tend to exhibit present day star formation and their surface brightness profiles show an exponential Sersic index (Fisher & Drory, 2008).

### 1.5.1 BTRSs

BTRSs are a result of the interaction of the radio jets of AGN with the Intra-Cluster Medium (ICM). The ICM is a low density high temperature plasma in galaxy clusters that acts as a medium in which the radio jets propagate. The existence and morphology of BTRSs is influenced by many physical phenomena starting with the radio emission that is formed by the process of jet formation. This process requires gas accretion onto a SMBH, jet collimation, which keeps the radio jet collimated up to distances $> 100\,\mathrm{kpc}$. The bending is due to the interaction of the jet with the ambient medium which depends on the characteristics and motions of intergalactic medium (IGM) in galaxy groups or the intra-cluster medium (ICM) in galaxy clusters. Fig. 1.5 shows the BTRS NGC 1265 as well as its more radio luminous core, shown in red. The host galaxy of NGC1265 is an elliptical galaxy with a stellar component of mass $M_* \approx 2.5 \times 10^{11}\mathrm{M}_\odot$.

A study of BTRSs has to incorporate all of these aspects, some of which are still active research areas. Because of this intersectionality, this work includes the SMBH mass measurements and their correlation with several galaxy characteristics. This is useful when studying high redshift galaxies whose SMBH masses may have to be inferred from the photometry of the galaxies. The BTRSs that are visible at high redshift have some of the most luminous radio jets in the Universe and therefore are likely to form in the most massive elliptical galaxies harbouring the most massive SMBHs, hence the high-mass end of the $M_{\mathrm{BH}} - \sigma$ relation is introduced first.

The study of BTRSs relies on the understanding of the inner cores of galaxies and the role played by SMBHs in jet formation as well as the role played by the ICM and IGM in the bending of galaxy jets. With the correlations between SMBH masses and their host galaxies suggesting a potential co-evolution of galaxies and their SMBHs as well as an effect of AGN feedback in quenching of star formation, to study how the galaxies have evolved over time, environments in which they evolved have to be considered. Studying the galaxies as a function of redshift requires the ability to identify different environments such as galaxy clusters in the distant Universe.

Optical surveys such as the Sloan Digital Sky Survey (SDSS) (York et al., 2000) have yielded an extensive list of galaxy clusters and groups in the nearby Universe (Koester et al., 2007). The limitation of optical surveys is that their depth, with current optical telescopes, becomes severely limited beyond the redshift of $\sim 0.3$. The detection of galaxy clusters via X-Ray emission also suffers from a similar impediment beyond the redshift of $\sim 1$. Radio surveys can go much further than this with respect to depth (Becker et al., 1995) and that fact was taken advantage of by

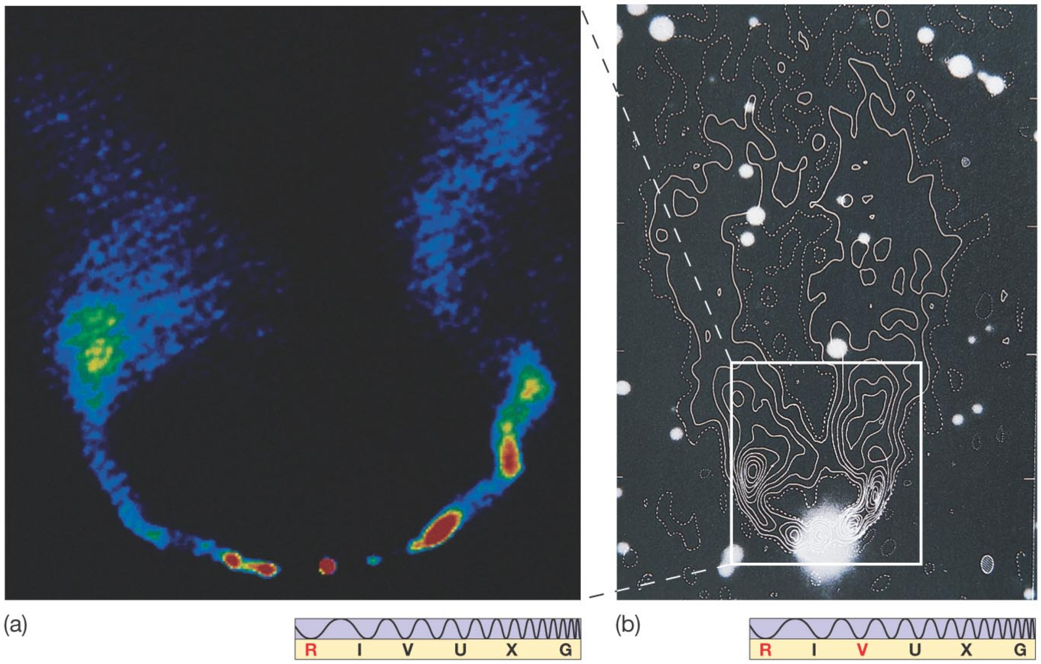

Figure 1.5: The radio image of NGC 1265 showing the basic bent morphology that is typical of BTRSs. On the left the core of the radio image is shown with the highest radio intensity shown in red. On the right the radio contours superimposed on the optical image are shown. It can be seen that, as in many extended radio sources, the radio emission covers a volume many times greater than the extent of the galaxy's stellar component. Image credit: Pearson Education, Inc

attempting to use radio galaxies as tracers of galaxy clusters and groups at high redshift (Blanton et al., 2000; Wing & Blanton, 2011).

BTRSs have been used as possible tracers of galaxy clusters at high redshift (Blanton et al., 2000, 2001, 2003). This has led to an interest in using them as probes to Intra-group medium (IGM) density in galaxy groups in the nearby Universe as there is currently no method for constraining IGM density analogous to using X-ray luminosity of the ICM to constrain the ICM density (Freeland et al., 2008; Morsony et al., 2013).

The discussion of the processes involved in the bending of jets is dominated by jet power, length of the jet, particle speeds as well as the magnetic fields in the jets and in the ICM (Kaiser et al., 1997; Kaiser & Alexander, 1997). These are influenced by SMBH masses and their accretion rates. The length of the jet is influenced by the age of the jet and the mechanisms that are responsible for maintaining their collimation (Antognini et al., 2012). These are active areas of research and they are still believed to depend on the type of Fanaroff-Riley type radio galaxies (FRGs) being studied. They are also believed to be dependent on the galaxy environment, with clusters and groups producing different fractions of FRGs.

These complications make trying to establish average characteristics of AGN radio jets challenging. This work represents a first step in establishing a method for a statistical study of the interaction of AGN jets and their cluster and group environments. These statistics can be compared to observational results of such all-sky radio surveys as the VLA FIRST survey for validation (Becker et al., 1995). Their predictions can be used to constrain the number of BTRSs that will be found by the square kilometre array (SKA).

Due to observational difficulty in deconvolving the influence of SMBH mass and spin on the Schwarzschild radius, the only blackhole property that is considered from an observational standpoint is the SMBH mass. This provides a direct link between observed extended radio source properties and the nature of the galaxies that host them. On a cosmological scale, galaxy formation and evolution is influenced by the environment in which the galaxies evolve, thus the role of the environment is further enhanced.

A very good review about the history of galaxy bulges and blackhole masses is by Graham (2016). There are a lot of good reviews on the matter of blackholes and AGN in general. The treatment of the topic, within this work, will only concentrate on the aspects pertinent to the context of this work and a reader who holds an interest in the subject can further pursue the subject by visiting these reviews and their references. I will be citing them as and when the need arises.

## 1.6 Galaxy clusters

As previously mentioned, the galaxy populations are influenced by their environments. The AGN populations in different environments also reflect this dichotomy and most AGN are found in galaxy clusters and groups. Galaxy clusters are the most massive gravitationally bound structures in the Universe. They are the building blocks of the cosmic web and are the link between astrophysics and cosmology. On the low mass end of galaxy clusters are galaxy groups. In this thesis, unless otherwise stated, galaxy groups shall mean small galaxy clusters with halo masses

$\leq 10^{13.5}$ $M_\odot$ and number of member galaxies ranging from tens to hundreds.

In every cluster or group, resides a brightest cluster/group galaxy (BCG) which is usually found close to the cluster/group core. It is the most massive member of the agglomeration. Best et al. (2007) found that, in the SDSS clusters and groups, BCGs were more likely to host a radio-loud AGN than field galaxies. The lower stellar mass BCGs ($M_* < 10^{11}$ $M_\odot$) are over an order of magnitude more likely to be radio-loud (where the 5 GHz flux is more than 10 times brighter that B-magnitude flux) than other galaxies of the same mass. This ratio falls off slightly to just below a factor of two for high-mass ($M_* > 5 \times 10^{11}$ $M_\odot$) BCGs of similar mass.

These BCGs are important in the work of finding high redshift clusters using BTRSs because they are likely to be the most radio-loud members of a cluster or a group. Due to the low likelihood of harbouring radio-loud AGN for low-mass galaxies, the increased likelihood found in BCGs greatly increases their efficacy as tracers of high redshift clusters, particularly because the fraction of high-mass galaxies was much lower at that epoch.

## 1.7 Radio properties of BTRSs

Radio-loud AGNs are generally hosted by massive elliptical galaxies with old stellar populations. The probability of a galaxy becoming radio-loud strongly depends on its stellar mass, even though the radio luminosity itself is not strongly correlated with galaxy mass for the radio-loud subset (Best, 2009). The length of an AGN jet depends largely on the age of the jet, the magnetic field, the mass of the SMBH, the accretion mechanism as well as the ICM environment (Antognini et al., 2012). There is, therefore, no straightforward way to map the stellar mass of the galaxy or blackhole mass to the length of the AGN jet. Radio loud galaxies have had their definition evolve with higher resolution and sensitivity of radio telescopes and larger Radio Surveys (Fanaroff & Riley, 1974; Baum & Heckman, 1989; Owen et al., 1989; Lin et al., 2010; Hardcastle, 2006). Tailed radio sources have radio luminosity greater than $10^{23}\,\mathrm{W\,Hz^{-1}}$ at 1.4 GHz and may show bent morphology to any degree (Lin et al., 2010). Bent tail radio sources would then be a subset of the tailed radio sources defined by,

- A large linear size extending more than 40 kpc from the radio core.
- A C-shape caused by large-scale bends of both tails in the same direction.

Best et al. (2005) lists how the fraction of radio-loud AGNs changes with the stellar mass of the host galaxy as well as a further breakdown of how much time each of these AGNs would spend with a luminosity above a certain threshold. They show this as a strong function of stellar mass. They also show that because the lower mass galaxies are more prevalent, the populations of all galaxy masses greater than $10^{10}$ $\mathrm{M}_{\odot}$ are represented in the high luminosity sample.

Their results translate to a relatively low abundance of 3% of $3 \times 10^{10}$ $\mathrm{M}_{\odot}$ radio-loud galaxies compared to radio-loud galaxies of mass $10^{11}$ $\mathrm{M}_{\odot}$ (Best et al., 2005; Bell et al., 2003). The abundance of radio-loud AGNs fall off quickly for galaxy masses less than $10^{11}$ $\mathrm{M}_{\odot}$. Best (2009) found the distribution of sizes of FRGs to be similar for sizes greater than 40 kpc. Consequently most of the jets larger than 40 kpc are hosted by galaxies with stellar masses above $10^{11}$ $\mathrm{M}_{\odot}$.

Different radio galaxy surveys provide different ratios of FR I to FR II galaxies as well as hybrid galaxies (7C Survey, 3CRR Survey, FIRST Survey, Molonglo Radio Catalog). They also lead to different distributions of jet sizes. However, the most recent surveys are the most sensitive and have better sky coverage and resolution. The FIRST survey is chosen because it has a good combination of the above desirable qualities compared to all current surveys. Using the results of the FIRST Survey, Blanton et al. (2000) found BTRSs to consist of 50% FR I, 25% FR II and 25% FR I-FR II galaxies. This sample was based on visual inspection and showed that despite the different excitation mechanisms that are argued to be responsible for the FR I-FR II dichotomy, the bent morphology occurs in both FR I and FR II galaxies and other studies have shown no correlation between source size and jet propagation speed at tens to hundreds of kpc scales (O'Dea et al., 2009).

## 1.8 Optical properties of BTRSs

The hosts of these BTRSs are elliptical galaxies, whose optical photometry shows no significant deviation from the structure of 'normal' elliptical galaxies (Blanton et al., 2000). Ledlow & Owen (1995) found that the Fanaroff-Riley radio galaxies are ellipticals showing some substructure at the sub-kiloparsec level. They also found that, except for their size, these hosts are indistinguishable from ordinary elliptical galaxies. This led them to conclude that, due to the presence of the SMBHs in their cores, all ellipticals display jets at some stage in their evolution. They also had R-band magnitudes that are brighter than −21 mag and 95% of their sample were FR I galaxies. This is comparable to Blanton et al. (2000) who found 80% of their sample to be FR I galaxies. Zirbel (1996) found that the mean absolute V-magnitudes of their whole sample of radio galaxies was $-22.658$ with $\sigma \leq 0.682$ and for the brightest cluster galaxies of their sample the mean was $-23.213$ with $\sigma \leq 0.366$. These magnitudes correspond to the brighter end of the elliptical galaxy luminosity function. Kormendy & Djorgovski (1989) found the distribution of elliptical galaxies to be Gaussian, peaking around -18 magnitude in the V-band. Heckman (1983) found the stellar $M/L$ ratio of radio-loud galaxies to be higher than normal ellipticals. Therefore, hosts of these radio galaxies are usually the brightest and most massive galaxies in the universe.

## 1.9 Samples from Radio surveys

Many radio surveys of extragalactic sources have been done since the dawn of radio astronomy. Only a few of the recent surveys have significantly increased the size of the sample of known BTRSs. FIRST and Australia telescope large area survey (ATLAS) and their contribution to BTRS statistics are discussed below.

### 1.9.1 FIRST survey

The April 2003 catalog of the FIRST survey covers $\simeq 9000\,\mathrm{deg}^2$ with a resolution of $5''$ FWHM to a limiting peak flux of 1 mJy. The FIRST survey's 'depth, large area, and high resolution implies that the images of the FIRST survey are fruitful fields to search for powerful jets at moderate to high redshift' (van Velzen et al., 2015). This is a Northern Hemisphere survey and is well-matched with the SDSS (York et al., 2000).

Blanton et al. (2000) visually examined $\simeq 32000$ multi-component sources from the $\simeq 3000\,\mathrm{deg}^2$ April 1997 catalog of the FIRST survey and found 384 to be BTRSs. The maximum angular separation between components was limited to $60''$. They found more than 50% of the BTRSs to be in rich clusters and the rest were found in groups (Blanton et al., 2000, 2001).

Proctor (2006) used a pattern recognition program to determine the degree of bending of radio galaxies in entire FIRST catalogue. They used a 2823 member random subset that was classified by visual inspection as a training set. They then used the result on the total sample to compare with SDSS seventh data release (DR7) (Abazajian et al., 2009) spectroscopic redshifts and SDSS photoZ2 DR7 (Oyaizu et al., 2008) photometric redshifts. They found BTRSs in rich groups or clusters 78% of the time (Wing & Blanton, 2011).

### 1.9.2 ATLAS survey of the Chandra Deep Field-South

The ATLAS survey of the Chandra deep field-south (CDFS) is a 1.4 GHz, 4 $\deg^2$ area, $17'' \times 7''$ resolution survey of the CDFS field located at the South Galactic Hole (Dehghan et al., 2014). It has an rms noise level varying from $\sim 15\,\mu$Jy in the low noise regions of the field to $\sim 1$ mJy towards the edges. This provides a sample of sources with rest-frame powers $10^{22} \leq \mathrm{P}_{1.4\,\mathrm{GHz}} \leq 10^{26}\,\mathrm{W\,Hz^{-1}}$. The linear sizes of the extended sources vary from tens of kpc to $\sim$1 Mpc and the redshift is up to z$\sim$2 (Dehghan et al., 2014).

The ATLAS data was supplemented with $2''$ VLA data ($2^{nd}$ data release) (Miller et al., 2013) over the $\sim 0.3\,\deg^2$ extended CDFS (ECDFS) field. The VLA ECDFS data also has a higher sensitivity of rms$=10\,\mu$Jy. The parts of the CDFS field that fall outside the ECDFS were supplemented with the extended VLA images. The improved resolution is responsible for the discovery of the bent morphology in more high redshift galaxies.

Of the 3079 radio sources above the $5\,\sigma$ detection level, 45 were BTRSs, nine could not be unambiguously classified, and one was a possible radio relic (Dehghan et al., 2014). This gives a ratio of $\sim$1.5% of the radio sources to be bent. With higher sensitivity, the SKA will observe more radio galaxies than any other telescope and the much better SKA resolution will allow the detection of smaller bending angles of the jet. This suggests that the resolution and higher sensitivity of the SKA will yield many more BTRSs at high redshift than the FIRST survey.

## 1.10 Open questions

The study of BTRSs is fundamentally the study of the motion of jet ejecta through the host interstellar medium (ISM) and the cluster ICM. Most of the open questions in this field pertain to the jet properties. This science will rely heavily on improved simulations of the plasma properties of AGN jets and the observations of the next generation of telescopes such as SKA, overwhelmingly large telescope (OWL) and the European extremely large telescope (E-ELT). The properties of the ISM, intergalactic medium (IGM) and the ICM such as the temperature and composition are quite well studied and the density in those media is quite well constrained.

The duty cycles of radio jets are an active area of research and the processes by which jets form are still subject to debate. Their collimation and bulk velocities are a subject of active study and the observed in situ acceleration of the jets is still not fully understood. The variation in jet composition as one moves away from the jet central engine is an area that will be explored via the SKA.

The effect of magnetic fields on the formation and collimation of jets, and its influence on the propagation of jets in the ICM on scales greater than 100 kpc, will be investigated via sensitive high resolution polarisation SKA observations.

The feedback mechanism between AGN jets and their host galaxies is a new field which has received a lot of attention in the last decade (Fabian, 2012; King & Pounds, 2015; Somerville & Davé, 2015; Naab & Ostriker, 2017). This may hold the key to understanding how the presence of SMBHs in galaxies have co-evolved with their environments on cosmological timescales. It may even prove to be the same as the observed difference between the environments of FR I and FR II galaxies.

These questions will be some of the driving forces in AGN research in the era of SKA. Better simulations are needed and more of the input physics can be interrogated when the observations have better sensitivity and resolution.

## 1.11 This work

In this work the feasibility of using BTRSs as tracers of galaxy clusters at high redshift is investigated. BTRSs have already been used in observational surveys as tracers of galaxy clusters up to a redshift of $\sim 1$ (Wing & Blanton, 2011; Blanton et al., 2000). The results have been promising, suggesting that this method has huge potential in light of the upcoming SKA and the expected rise in the number of high redshift radio sources compared to sources in other wavelength regimes.

However, there are still some unanswered questions. The results of BTRS clusters in the radio surveys have not been compared with other methods of tracing galaxy clusters to compare the efficacy of the different methods. This is particularly relevant given the dependence of the prevalence of radio sources on their environments (Best et al., 2007).

Another matter that has not been addressed in this work is how this method would work in the high redshift Universe when the density was higher due to the Universe itself being smaller. This is further complicated by the fact that according to hierarchical structure formation the massive clusters had not yet formed in the high redshift Universe.

It is also not yet clear what the cut off is for a galaxy cluster as opposed to a galaxy group (Mulchaey, 2000). This makes it unclear how the agglomerations found through BTRS observations can be separated into galaxy clusters and groups in the absence of sufficiently deep optical observations. The studies done on this method have not yet delved into the question of the bending of jets in groups as opposed to clusters. To look for clusters at $z > 2$ the ability to discriminate between the two is necessary.

The assumption that BTRSs occur in groups or clusters has already been proven to not always hold by the discovery of a BTRS in a filament rather than a cluster (Edwards et al., 2010). This interesting result suggests that this ansatz may not always be true. The prevalence of exceptions to this ansatz and thus its efficacy as a tracer of the largest gravitationally bound structures in the high redshift Universe is investigated using ΛCDM cosmological simulations.

The formation and collimation of radio jets over large distances is still an area of active research (Blandford et al., 2019). The magneto-hydrodynamic (MHD) simulations have recently played a major role in advancing the understanding of the processes involved, both at the level of jet formation and collimation in proto-stellar discs and in the accretion discs found near the SMBHs of AGNs (Davis & Tchekhovskoy, 2020). Finding a self-consistent theoretical picture of these processes as well as the re-acceleration of the ejecta that is necessary to explain the large extent of the radio jets would go a long way in explaining the processes involved in the formation of BTRSs.

With the new generation of optical and near infrared (NIR) telescopes, the earliest stages of galaxy formation as well as their evolution with the Universe will be observed. Using the SKA and these telescopes, galaxy evolution can be studied in a much finer detail than ever before. Current models of galaxy evolution can be compared with observations in this still developing field of research.

The most massive galaxies, harbouring the most massive SMBHs, have been shown to have a higher occurrence of radio loudness (Best et al., 2005). Our understanding of the influence of the high mass end of SMBHs on host galaxies and their environment is fundamental to the efficacy in using BTRSs as tracers of galaxy clusters at high redshift. The high mass end of the $M_{\mathrm{BH}} - \sigma$ relation seems to be non-linear, hence increasing the number of massive SMBHs measured would help statistically constrain that observation. Thus, the study of radio-loud galaxies is tied to the study of SMBH masses and the study of BTRSs looks at both the influence of the galaxy clusters on the jet morphology and the influence of redshift on the BTRSs. The SMBH mass measurements methods that are applied at high redshift are based on correlations that are constrained in the local Universe. This suggests that, since BTRSs are dependant on SMBHs of their host galaxies, it is important to study SMBH mass measurements both in the local Universe and at high redshift to understand BTRSs better.

### 1.11.1 Thesis outline

This work is structured as follows: the introductory chapter is a general review of the field of AGNs and how the field has evolved over time.

Chapter 2 discusses the telescopes for which data reduction was done in this thesis. This excludes telescopes for which we used results directly without any for of data reduction or analysis. These are the Southern African large telescope (SALT), Hubble space telescope (HST) and Gemini North telescope.

Chapter 3 deals with the velocity dispersion measurements of a sample of Southern massive galaxies. Each member in the sample is an ETG chosen because of a literature velocity dispersion ($\sigma$). The $\sigma$ measurements are done using the penalized pixel fitting (PPXF) algorithm. They are compared to the $M_{\mathrm{BH}} - \sigma$ relation. This is a good way of predicting the $M_{\mathrm{BH}}$ of any galaxy, as the tight correlation of the $M_{\mathrm{BH}} - \sigma$ relation is well established.

Chapter 4 discusses a Bayesian method of measuring SMBH mass using stellar kinematics and Jeans anisotropic multi-Gaussian (JAM) modelling.

Chapter 5 pertains to the measurement of the kinematics of the core of the galaxy NGC 6861 using the method developed in the previous chapter and the parameterisation of stellar surface brightness using the multi-Gaussian expansion (MGE). This is a lenticular galaxy with fast rotation and a dust lane within the inner $10''$ of the core. This dust lane makes the measurement of the surface brightness of the galaxy core more challenging.

Chapter 6 looks at the correlation between $M_{\mathrm{BH}}$ and the radio luminosity at 151 MHz for galaxies at high redshift. The blackhole masses are measured using the VME method and the radio observations are from the seventh Cambridge radio survey catalogue. These results are compared to similar results that have been made at higher frequency.

Chapter 7 discusses the BTRSs in their cluster and group environments. These BTRSs are inferred from the MareNostrum Universe simulation and the structure and power of radio jets is considered generic rather than having a distinction between Fanaroff-Riley types I and II (FR I-FR II). The number of BTRSs that should be observed by the SKA, if average values for jet velocities and power are used, is investigated.

Chapter 8 brings it all together in a summary and future work. Future work is discussed as well as potential directions that the study may take. Synergies with current techniques and how upcoming telescopes can be used to implement the techniques discussed in this work are discussed.

# Chapter 2

# Telescopes and instruments

In this work the stellar kinematics of galaxy cores are studied via spectroscopy using data from three different telescopes, namely HST, Southern African Large Telescope (SALT), the Very Large Telescope's (VLT) **S**pectrograph for **IN**tegral **F**ield **O**bservations in the **N**ear **I**nfrared (SINFONI) instrument and the GEMINI (North) telescope. SALT and GEMINI data is for longslit and SINFONI is IFU spectroscopy.

## 2.1 SALT

SALT is an optical telescope that is situated in the South African town of Sutherland. It is at an altitude of 1798 m above sea level. It has a primary mirror of 11m diameter made of 91 separate but identical hexagonal segments. These are laid out in a hexagonal mosaic i.e. they are arranged so that the vertices transcribe an 11 m circle. It shares the same basic design as the Hobby Eberly Telescope (HET) at the MacDonald Observatory in Texas, USA. Unlike the HET, SALT uses a spherical primary mirror instead of a parabolic one. This allows the hexagonal segments to be exactly the same thus reducing the manufacturing costs of the telescope's primary mirror.

This makes the telescope susceptible to spherical aberrations in the image, which are mitigated by the Spherical Aberration Corrector (SAC). The SAC is mounted at 13.8 m away from and concentric with the primary mirror. It provides a circular $8'$ FoV over the declination range $-75^\circ$ to $+10^\circ$ with a prime focus beam of f/4.2. It has a spherical mirror with a fixed elevation angle of 37 degrees. This primary mirror is stationary during observations and the targets are tracked by moving the optics and instruments which are mounted at prime focus. This means that the telescope can point to only a fraction of the sky at any given moment. This creates a visible 'doughnut' region of the sky where targets can be tracked for as short as about one hour to longer than six hours depending on the target's position in the sky.

SALT/RSS is a spectrograph with a spectral resolution of $\sim 500 - 10\,000$ and a pixel size of $0\farcs22$. Its wavelength coverage is 320 nm to 900 nm. This resolution, along with fairly good sky conditions, allows the measurement of velocity dispersion and systemic velocities with smaller error bars than most literature values of the chosen galaxy sample. More secure velocity dispersion measurements with higher S/N can, therefore, be attained by using SALT.

The data reduction was done using the image reduction and analysis facility (IRAF). The normal IRAF longslit data reduction steps are followed. The cosmic ray removal was achieved using the xzap package of IRAF. The rest of the data reduction steps were performed using various tasks in IRAF TWODSPEC package for the galaxy and flux standard stars. The flat-fielding was ignored due to SALT's internal calibration flats' tendency to increase the pixel-to-pixel sensitivity variation. The lack of flat-fielding does not affect the measurement of velocity dispersion.

## 2.2 VLT telescope

SINFONI is an IFU mounted in the Cassegrain focus of the very large telescope (VLT) unit telescope 4 (Yepun) at Paranal La Silla Observatory (Eisenhauer et al., 2003; Bonnet et al., 2004). It has J, H, K and H+K gratings in the near-infrared (NIR) ($1 - 2.5\,\mu$m) spectral domain. The SINFONI IFU instrument uses the image slicing technique to simultaneously obtain spectra over a continuous FoV. The spectral resolution $\lambda/\Delta\lambda$ is 2 000, 3 000 and 4 000 for J, H and K bands respectively.

The VLT is an interferometer of 4 optical/NIR 8.2m telescopes that is located at the Cerro Paranal mountain in Chile. It is located at an altitude of 2635 m above sea level. The telescope is equipped with adatptive optics which allows it to perform nearly diffrection-limited spectroscopy.

The SINFONI image slicer uses mirrors to slice the image in the focal plane of the telescope into 32 slitlets. The light from each of the 32 slitlets is then imaged onto 64 pixels on the detector thus obtaining 32x64 spectra of the imaged FoV. The instrument has an adjustable spatial scale with the following spatial scales: $0''\!.25, 0''\!.1$ and $0''\!.025$ per spaxel, which result in the FoV $8'' \times 8''$, $3'' \times 3''$ and $0''\!.8 \times 0''\!.8$.

## 2.3 Gemini North telescope

The GMOS-N data in this thesis is observed with the 8.1 m diameter, altitude-azimuth mounted Frederick C. Gillett Gemini North telescope. Gemini North telescope is located on the summit of Mauna Kea in Hawaii. The altitude of the telescope (4213 m above sea level) and the longitude Mauna Kea +19.824° allows for an all sky view in a dry, stable and clear environment that makes this telescope one of the best optical/NIR facilities in the world.

The Gemini North telescope has the following four features that improve its performance:

- The thin primary mirror that rests on a bed of 120 hydraulic actuators which maintains the mirror surface at its optimum shape while the telescope tracks across the sky.
- A 1 m diameter secondary mirror capable of rapid tip-tilt corrective motions which keep astronomical objects stationary in the focal plane as the telescope tracks across the sky. This protects from the effects of wind gusts shaking the telescope, atmospheric turbulence and temperature or density fluctuations along the light path through the atmosphere causing the image to wander.
- Adaptive optics which, in the short wavelength infrared bands, can correct for image blurring caused by atmospheric turbulence and produce images that are near-diffraction-limited.
- Vents on the dome walls that can be opened to regulate the temperature of the air above the primary mirror to match the temperature outside the dome.

## 2.4 Hubble Space telescope

The Hubble Space Telescope (HST) is a low Earth orbit space telescope that was launched in 1990. The HST has a 2.4 m primary mirror. It observes in the ultraviolet (UV), visible, and NIR regions of the electromagnetic spectrum. Being a space telescope, the HST is not affected by the distortion of the atmosphere and that allows it to have a high-resolution and much lower background light than ground-based telescopes.

The HST was built by the National Aeronautics and Space Administration (NASA) agency of the United States of America (USA) and launched by Space Shuttle Discovery in 1990. Five Space Shuttle missions have repaired, upgraded, and replaced systems on the telescope, including the primary mirror and all five of the main instruments. The telescope is still operating after 30 years.

# Chapter 3

# Velocity dispersion measurements of ETGs

## 3.1 Introduction

SMBH masses correlate with several properties of their host galaxies in such a way as to suggest co-evolution with their host galaxies. As already discussed, the most commonly used correlations between SMBHs and the characteristics of their host galaxies are the $M_{\rm BH} - \sigma$ (Ferrarese & Merritt, 2000; Gebhardt et al., 2000), $M_{\rm BH} - M_{\rm bulge}$ (Dressler, 1989), and $M_{\rm BH} - L_{\rm bulge}$ (Tremaine et al., 2002). There are different hypotheses on the existence of these correlations which range from the non-causal galaxy-galaxy merger hypothesis (Jahnke & Macciò, 2011) to causal feedback mechanism between the AGN and its host galaxy (Fabian, 1999). There still is, however, a possibility that these blackhole scaling relations only hold for elliptical galaxies and bulges. There are not enough measured SMBH masses in literature to sufficiently constrain these hypotheses and the current results suggest that $M_{\rm BH} - \sigma$ and $M_{\rm BH} - L_{\rm bulge}$ are not mutually consistent (Lauer et al., 2007).

In this chapter we measure the velocity dispersion of a sample of galaxies observed with the SALT telescope. This sample is chosen such as to allow for follow up studies with current IFU telescopes, whose resolution would allow for the dynamical mass measurements using the Jeans anisotropic multi-Gaussian method or the Schwarzschild orbit superposition methods. This sample is a pilot project for a study of Southern SMBH mass measurements which we aim to expand on.

It is important to reduce the scatter in the local SMBH mass measurements of galaxies in the nearby Universe because they are used to calibrate the SMBH mass measurements for high redshift galaxies. The single-epoch SMBH mass measurements of high redshift galaxies are calibrated using RM method results assuming the local $M_{\rm BH} - \sigma$ relation.

An ideal way to determine the SMBH mass would be to determine the kinematics of individual stars in the vicinity of the SMBH. It is not possible to determine the stellar kinematics of galaxies beyond the local group using individual stars with the current ground-based and space telescopes due to insufficient spatial resolution. However, the stellar component of such galaxies can be observed as a continuum of light from individual stars. In that case the SMBH masses in these galaxies are derived by measuring the line-of-sight velocity dispersion (LOSVD) of an aggregate of stars as a function of radius.

The current generation of large optical telescopes with IFU instruments and AO technology can resolve the SOI of high mass SMBHs up to galaxy distances of just beyond 100 Mpc at best. In sub-millimeter and radio regimes, the Atacama large millimeter array (ALMA) and the very long baseline array (VLBA) respectively, have similar capabilities. The upcoming generation of telescopes, with improved sensitivity and resolution, will allow the improvement of the statistics of SMBH masses on both the high and low mass ends. However, when using the $M_{\rm BH} - \sigma$ relation, spectra of the potential target galaxies are needed to evaluate the suitability of the targets for SMBH mass measurement. Most of the nearby galaxies do not have spectra available and even those that are found in the amalgamated literature database HyperLeda (Paturel et al., 2003) are sometimes unreliable due to low S/N ratio and the different instrumental resolution of the telescopes used in the observations.

The $M_{\rm BH} - \sigma$ relation, discussed earlier, has long received attention as it shows a link between the masses of SMBHs and the global properties of their host ETGs and bulges of spiral galaxies. A comprehensive review of these relations is available in Kormendy & Ho (2013) and Shankar (2009). Because it is based on longslit spectroscopy, it is a little more costly in terms of telescope time than photometry based relations. However, the costs are not restrictively high and the benefits of using this relation more than justify the higher telescope time investment.

In this chapter the LOSVD of a pilot sample of Southern Hemisphere nearby high velocity dispersion galaxies are measured. The extension of this pilot survey would be an ideal complement to the Northern Hemisphere's Hobby Eberly telescope (HET) massive galaxy survey (HETMGS) because of the Southerly position of SALT and the similarity in size and capability of the two telescopes. As discussed in the introduction chapter, the high mass end of the $M_{\rm BH} - \sigma$ relation is not well constrained. By measuring the SMBH masses of more high $\sigma$ galaxies, the statistics at that end of the relation will be increased, thereby better constraining the overall $M_{\mathrm{BH}} - \sigma$ relation. A first step in the attempt to measure the high mass end of the $M_{\mathrm{BH}} - \sigma$ relation is finding the high $\sigma$ galaxies on which follow up studies may be done with IFU telescopes that make use of AO instruments.

Longslit optical and NIR spectroscopy of galaxies is the primary technique for measuring the velocity dispersion of ETGs and bulges for use in the $M_{\mathrm{BH}} - \sigma$ relation. The longslit spectroscopy in this study was performed using the Southern African large telescope Robert Stobie spectrograph (SALT/RSS).

Photometry of galaxies is the most freely available observational result in the study of galaxies, hence the relation between $M_{\mathrm{BH}}$ and the Sersic index $n$ is used as a guide to blackhole mass when one is faced with a random sample of galaxies. The $M_{\mathrm{BH}} - \sigma$ relation can then be used to further consolidate the sample, in this case looking for high velocity dispersion galaxies that correspond to high mass SMBHs.

With the upcoming generation of optical telescopes such as the European extremely large telescope (E-ELT) and the overwhelmingly large telescope (OWL) and potentially combined with AO technology the SOI of the high mass end of SMBHs will be resolved up to distances beyond 350 Mpc and the low mass end will be resolved up to distances beyond the 14 Mpc distance of the Virgo cluster. This would expand the sample of Southern galaxies chosen with the view of investigating the slope to the $M_{\mathrm{BH}} - \sigma$ relation.

## 3.2 Pilot study

This survey is a pilot study to use the Southern African large telescope (SALT) to find galaxies that are suitable for dynamical SMBH mass measurement in the Southern Hemisphere. Its success will lead to the extension of the survey to complement the HETMGS for Southern galaxies (van den Bosch et al., 2015). SALT is used for $\sigma$ measurements and the follow up studies for SMBH mass measurements can be done with VLT SINFONI and the Keck telescopes, which have IFU and AO instruments.

The HETMGS survey is an optical long-slit spectroscopic survey of 1022 galaxies that lay within the declination limits of $-11^\circ < \delta > 73^\circ$ using the 10m HET telescope at the McDonald Observatory (Ramsey et al., 1998). The main goal of the HETMGS survey was to find nearby galaxies that are suitable for SMBH mass measurement with a particular focus on those galaxies predicted to have the largest SOI.

### 3.2.1 Sample selection

The sample was found by searching the literature for high $\sigma$ galaxies that are visible to the Southern African large telescope (SALT). The right ascension and declination limits are designed to take advantage of the location and capabilities of the SALT telescope. The main goal of this sample is to find nearby galaxies that are suitable for SMBH mass measurement with a particular focus on those galaxies predicted to have the largest SOI.

The SALT galaxy sample is chosen based on the following criteria which are designed to take advantage of the capabilities of SALT as well as the location of the site,

- Declination limits of $10^\circ < \delta > -75^\circ$
- Galaxy distance less than 70 Mpc
- Galaxy velocity dispersion greater than 250 $\mathrm{km\,s^{-1}}$

Another important consideration is the limiting distance of the current telescope capabilities for the resolution of the SOI of the galaxy under study.

A sample of Southern Hemisphere extra-galactic sources having a velocity dispersion that corresponds to SMBH masses $> 10^9$ $\mathrm{M_\odot}$ from HyperLeda (Makarov et al., 2014) has been chosen. The HyperLeda archive is a database and a collection of tools used in the study of galaxies and cosmology. It keeps track of such galaxy parameters as distance, morphology, astrometry, kinematics, and spectroscopy. Some of the spectroscopic data does not have a S/N ratio high enough for the velocity dispersion measurements needed in the $M_{\mathrm{BH}} - \sigma$ relation. Table 3.1, below lists the stars that meet the selection criteria in literature. The literature values for recessional velocity, redshift and velocity dispersion are stated in the table for comparison with the values achieved in this work.

This is to allow for a sample that can be observed from the site of SALT (Sutherland) and whose SMBH's SOI is resolvable with current IFU instrument. The best resolution from current IFUs with AO, including SINFONI is $0.''025$. Because this is a pilot project, galaxies with high velocity dispersion have been chosen so that SMBHs of high mass may be found. This is to improve statistics of high mass SMBHs as discussed earlier.

The follow up studies of the sample will be done with a spectral resolution that is capable of resolving the SOI of the SMBH. This can be achieved with IFU instruments on telescopes possessing AO e.g. VLT SINFONI. That puts a distance limit of about 100 Mpc for a galaxy with a $10^9$ $M_\odot$ SMBH and a velocity dispersion of 400 $\mathrm{km\,s^{-1}}$. SALT and the Very Large Telescope (VLT) in Chile share the Southern skies, therefore, that makes the SINFONI-VLT the perfect instrument with which to do follow-up studies of the SALT sample.

The criterion of spatially resolvable kinematics of SMBH's SOI can be traced by either stellar or gas kinematics. The details of the physics involved in using those two tracers are discussed in the next chapter. The size of the SOI is derived from the virial theorem by assuming a spherical

Table 3.1: SALT sample and literature values of recessional velocity and velocity dispersion $\sigma$. All the values are taken from HyperLeda except for ESO137-044, whose literature values come from NED/IPAC

| Galaxy name | Recessional velocity ( $\mathrm{km\,s^{-1}}$) | Velocity dispersion ( $\mathrm{km\,s^{-1}}$) |
|---|---|---|
| IC 1356 | $8494 \pm 24$ | $342.4 \pm 16.5$ |
| NGC 7196 | $2886 \pm 23$ | $279.2 \pm 37.7$ |
| NGC 7796 | $3341 \pm 15$ | $253.3 \pm 6.0$ |
| IC 5105 | $5407 \pm 15$ | $304.0 \pm 11.2$ |
| ESO 139-026 | $4990 \pm 38$ | $286.1 \pm 19.8$ |
| ESO 137-029 | $5310 \pm 8$ | $389.5 \pm 31.4$ |
| NGC 1400 | $590 \pm 11$ | $245.8 \pm 3.4$ |
| NGC 7014 | $4762 \pm 19$ | $288.5 \pm 7.8$ |
| NGC 5791 | $3347 \pm 12$ | $247.9 \pm 12.4$ |
| NGC 5796 | $2910 \pm 35$ | $266.5 \pm 6.1$ |
| IC 4765 | $4488 \pm 10$ | $278.4 \pm 5.8$ |
| ESO 137-008 | $3856 \pm 19$ | $282.7 \pm 11.2$ |
| NGC 6868 | $2949 \pm 9$ | $252.3 \pm 4.0$ |
| NGC 6861 | $2824 \pm 18$ | $406.9 \pm 19.6$ |
| NGC 1045 | $4617 \pm 17$ | $307.3 \pm 24.8$ |

isotropic region around the SMBH. The region where the SMBH's gravitational force dominates over the motion due to the rest of the galaxy is a sphere of a size defined as $r_i \equiv GM_{\mathrm{BH}}\sigma^{-2}$. Its apparent size at distance $D$ away can be represented as $\theta = r_i D^{-1}$.

In the absence of a measured SMBH mass the SOI ($\theta_i$) may be estimated using the scaling relation $\theta_i = G\sigma^{2.5}D^{-1}$ which assumes the slope of the $M_{\mathrm{BH}} - \sigma$ relation of 4.5 of Gültekin et al. (2009). This allows for the prediction of the SOI using only the distance to the galaxy and $\sigma$. The actual size of the SOI can only be confirmed upon the measurement of the SMBH mass.

These galaxies are re-observed with SALT to systematically obtain high S/N ratio. This helps improve on the HyperLeda results and give more secure spectroscopic measurements for use by the extra-galactic astronomy community.

The S/N ratio is calculated using the DER-SNR algorithm suggested by Stoehr et al. (2008). This method has been used extensively in high resolution spectroscopy of the Hubble Space Telescope's Space Telescope Imaging Spectrograph (HST/STIS). It is a simple and robust way of calculating S/N. It also allows for a cross comparison between S/N measurements from different telescopes (Stoehr et al., 2008).

## 3.3 Observations and data reduction

The SALT CCD is a mosaic of three CCDs of size $1\,020 \times 2\,051$ with approximately 50 pixel gaps between the CCDs. These gaps have to be mitigated in the data reduction. This is done by filling the gap through smoothing the transition between the pixel values at the edges of the gaps. This ensures that IRAF data reduction steps from being biased by the null values in the gaps.

Standard data reduction steps were performed by the automated pre-processing software at the South African astronomical observatory (SAAO) for the SALT data. The pre-processing steps performed include: bias subtraction, overscan correction and trimming, gain correction, mosaicing of the three CCDs and correction for the amplifier cross-talk. The pre-processing reductions were performed using PyRAF. It has been found that the internal calibration unit flat fields increased the pixel-to-pixel sensitivity variation of the CCD. This has led to the eschewing of the use of these flats in the flatfielding of the SALT spectra. The reduced SALT image has a mosaiced CCD with interpolation between the CCD gaps.

The next step in the data collection process is the observation of arc lamps and galaxy spectra. The arc lamps contain gas(es) for which *a priori* spectra are available. The arc lamps in SALT use ThAR, Xe and CuAr gases for the PG0900 grating in the wavelength range 3500 Å −7500 Å. The PG0900 grating has a resolving power of 600−2000 for a $1\farcs25$ depending on the grating angle. Fig. 3.1 shows a typical predicted efficiency of the PG0900 grating on SALT. The efficiency simulation is centred at 5500 Å. It shows the efficiency of up to 90% for the grating. The arc lamps are used to establish how light is dispersed in the telescope and the CCD. SALT uses the IRAF tasks IDENTIFY and REIDENTIFY to allow for a visual matching of the arc spectra. The wavelength solutions are then applied to the galaxy spectra using IRAF's FITCOORDS and TRANSFORM tasks.

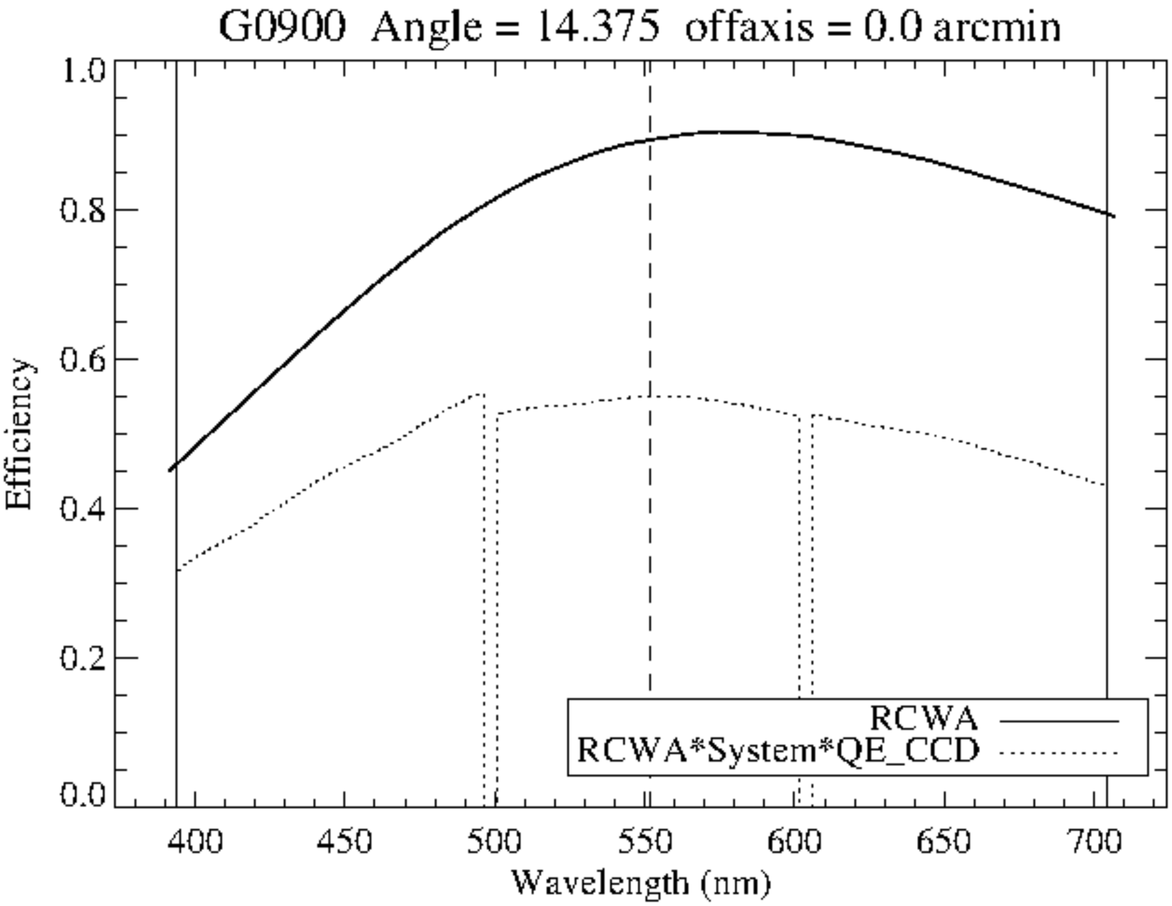

Figure 3.1: The predicted efficiency curve of a PG0900 grating. The calculation, centred on 550 nm wavelength, is done via the RSS simulator. Figure taken from https://pysalt.salt.ac.za/proposal-calls/2013-2/

The spectrum is extracted from the CCD with the APALL task after the background sky spectrum has been removed with IRAF's BACKGROUND task. Flux calibration is then done with a combination of REPONSE, SENS and CALIBRATE for SALT data.

The last step is the combining of spectra of the same galaxy that were taken to increase S/N ratio and to ensure, in the event of cosmic rays falling on the spectrum, that there are at least two extra spectra to allow for minimum statistical comparison of the true spectrum. SALT data is combined with the IRAF task SCOMBINE. The final list of galaxies comprised of about 20 ETGs with different surface brightness profiles. The observation log is listed in the Table 3.2 below.

Table 3.2: The summary of observation data for the SALT sample of galaxies.

| Galaxy name | RA (J2000) | Dec (J2000) | Observation date | Integration time (s) | Grating | |
|---|---|---|---|---|---|---|
| NGC 1045 | $02^{\mathrm{h}}40^{\mathrm{m}}29.^{\mathrm{s}}1$ | $-11^\circ16'39''$ | 2012-01-01 | 3×780 | PG0900 | 239 |
| NGC 1217 | $03^{\mathrm{h}}06^{\mathrm{m}}06.^{\mathrm{s}}0$ | $-39^\circ02'11''$ | 2011-11-03 | 900 | PG0900 | 154 |
| NGC 0424 | $01^{\mathrm{h}}11^{\mathrm{m}}27.^{\mathrm{s}}6$ | $-38^\circ05'00''$ | 2011-11-06 | 900 | PG0900 | 43 |
| NGC 6861 | $20^{\mathrm{h}}07^{\mathrm{m}}19.^{\mathrm{s}}5$ | $-48^\circ22'12''$ | 2012-07-10 | 2×420 | PG0900 | 179 |
| IC 5105 | $21^{\mathrm{h}}24^{\mathrm{m}}22.^{\mathrm{s}}0$ | $-40^\circ32'16''$ | 2012-07-11 | 2×500 | PG0900 | 190 |
| NGC 1400 | $03^{\mathrm{h}}39^{\mathrm{m}}30.^{\mathrm{s}}9$ | $-18^\circ41'17''$ | 2012-01-14 | 900 | PG0900 | 251 |
| NGC 7796 | $23^{\mathrm{h}}58^{\mathrm{m}}59.^{\mathrm{s}}8$ | $-55^\circ27'30''$ | 2012-15-05 | 2×450 | PG0900 | 188 |
| ESO 209-012 | $08^{\mathrm{h}}01^{\mathrm{m}}58.^{\mathrm{s}}0$ | $-49^\circ46'42''$ | 2011-12-19 | 900 | PG0900 | 90 |
| NGC 6893 | $20^{\mathrm{h}}20^{\mathrm{m}}49.^{\mathrm{s}}6$ | $-48^\circ14'20''$ | 2012-04-20 | 2×780 | PG0900 | 269 |
| IC 4765 | $18^{\mathrm{h}}47^{\mathrm{m}}18.^{\mathrm{s}}2$ | $-63^\circ19'52''$ | 2012-05-21 | 2×450 | PG0900 | 82 |
| ESO 137-008 | $16^{\mathrm{h}}15^{\mathrm{m}}46.^{\mathrm{s}}1$ | $-60^\circ55'07''$ | 2012-05-21 | 2×450 | PG0900 | 59 |
| NGC 5791 | $14^{\mathrm{h}}58^{\mathrm{m}}46.^{\mathrm{s}}2$ | $-19^\circ16'00''$ | 2012-05-21 | 2×394 | PG0900 | 63 |
| NGC 7014 | $21^{\mathrm{h}}07^{\mathrm{m}}52.^{\mathrm{s}}2$ | $-47^\circ10'44''$ | 2012-05-21 | 2×450 | PG0900 | 63 |
| ESO 139-026 | $17^{\mathrm{h}}46^{\mathrm{m}}50.^{\mathrm{s}}8$ | $-59^\circ15'30''$ | 2012-05-23 | 3×450 | PG0900 | 145 |
| ESO 137-029 | $16^{\mathrm{h}}29^{\mathrm{m}}06.^{\mathrm{s}}6$ | $-61^\circ38'39''$ | 2012-05-23 | 3×450 | PG0900 | 137 |
| NGC 5796 | $14^{\mathrm{h}}59^{\mathrm{m}}24.^{\mathrm{s}}1$ | $-16^\circ37'26''$ | 2012-05-27 | 2×450 | PG0900 | 145 |
| NGC 6868 | $20^{\mathrm{h}}09^{\mathrm{m}}54.^{\mathrm{s}}1$ | $-48^\circ22'46''$ | 2012-06-28 | 2×420 | PG0900 | 161 |
| IC 1356 | $21^{\mathrm{h}}02^{\mathrm{m}}53.^{\mathrm{s}}0$ | $-15^\circ48'41''$ | 2012-05-22 | 3×450 | PG0900 | 89 |
| NGC 7196 | $22^{\mathrm{h}}05^{\mathrm{m}}54.^{\mathrm{s}}8$ | $-50^\circ07'09''$ | 2012-05-22 | 2×450 | PG0900 | 163 |
| ESO 137-044 | $16^{\mathrm{h}}50^{\mathrm{m}}54.^{\mathrm{s}}6$ | $-61^\circ48'45''$ | 2012-05-22 | 3×450 | PG0900 | 107 |

The reduced spectra are shown in Figs 3.2, 3.3 and 3.4. Absorption lines from these spectra are used to determine $\sigma$ using the LOSVD. The quality of the spectra's absorption lines and S/N ratio has a positive influence on the accuracy of the $\sigma$ measurement.

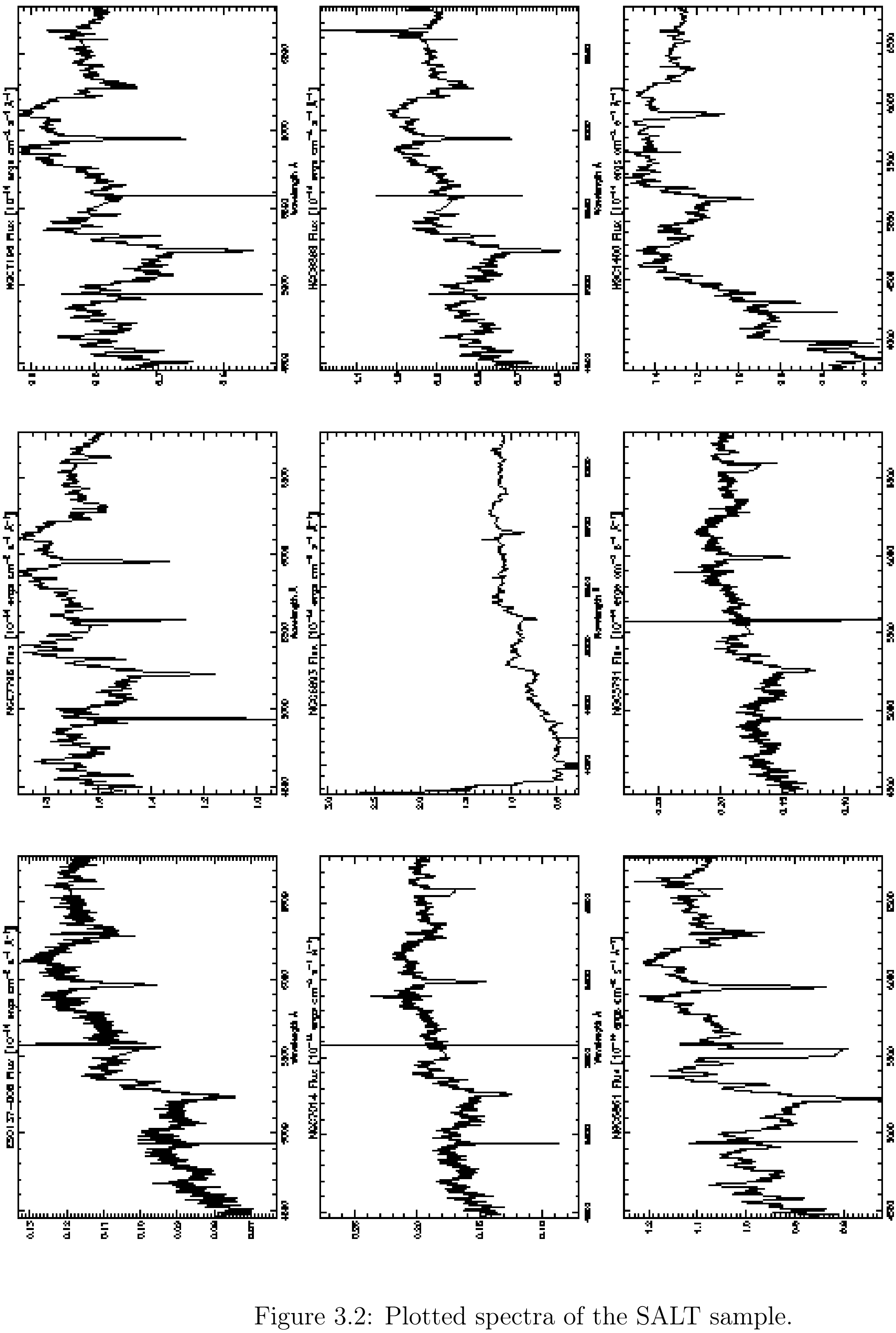

Figure 3.2: Plotted spectra of the SALT sample.

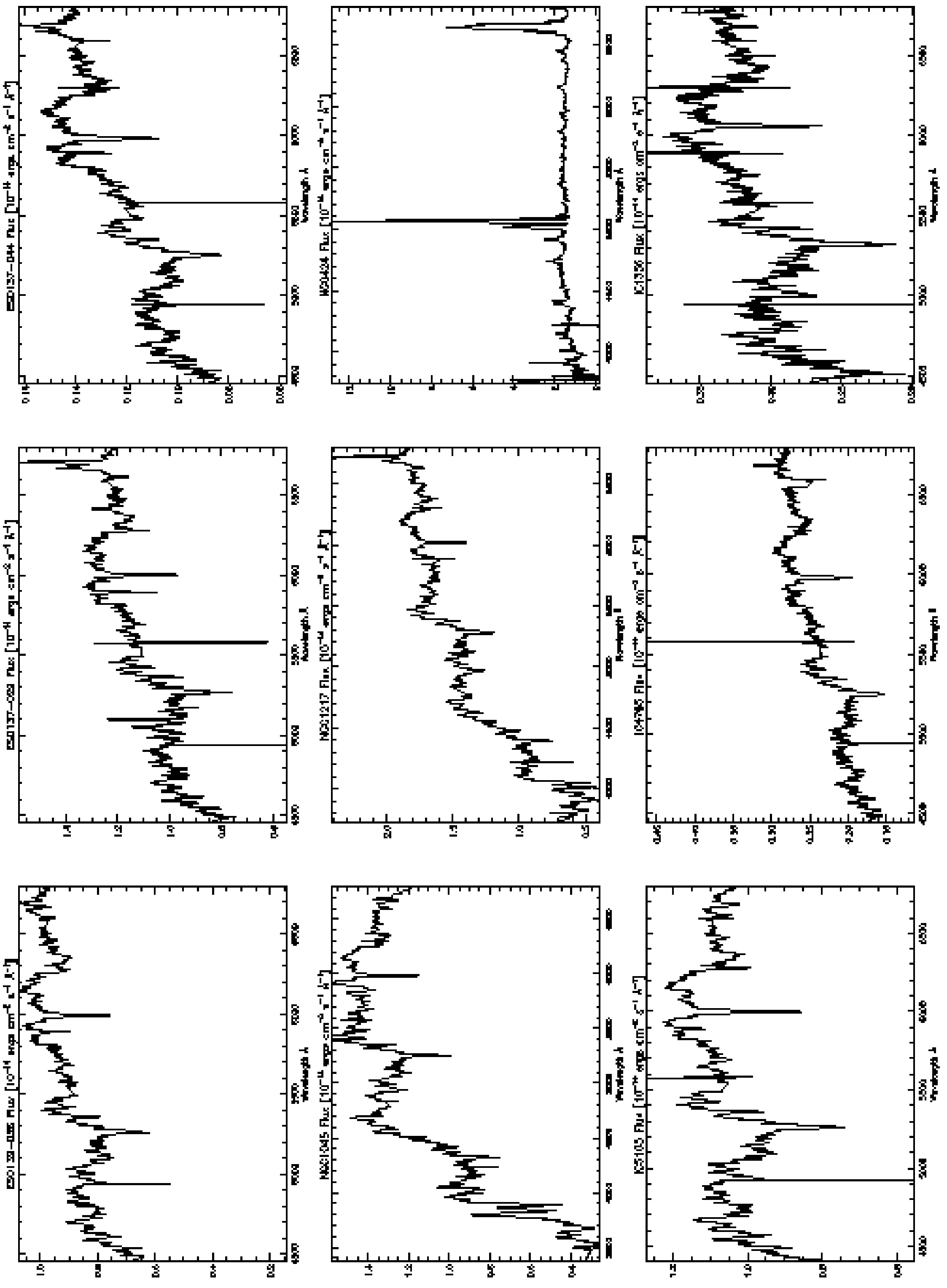

Figure 3.3: Plotted spectra of the SALT sample.

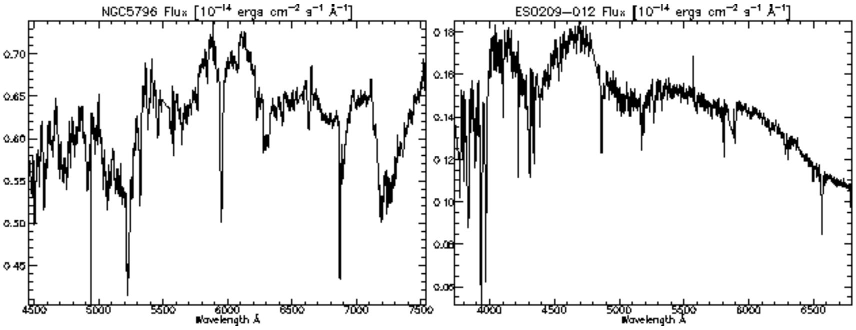

Figure 3.4: Plotted spectra of the SALT sample.

The spectral absorption lines, which are used to measure the full width at half maximum (FWHM), that are found in the range covered in the sample, are listed in Table 3.3. The emission lines in this wavelength range made velocity dispersion measurement a challenge. For all the spectra in the sample that extend redward of 7 000 Å, there is broad absorption line that makes this end of the spectrum unusable for kinematic analysis. This is a common absorption problem that is due to the HO molecule.

Table 3.3: Interesting absorption lines in the spectral range 3500Å - 6500Å.

| Wavelength (Å) | Element |
|---|---|
| 3934.777 | CaII (K) |
| 3969.588 | CaII (H) |
| 4305.61 | G |
| 5176.7 | Mg |
| 5895.6 | Na |

## 3.4 Results and analysis

A popular method for measuring the kinematics of a galaxy is using the Fourier correlation quotient (FCQ) (Bender, 1990), which allows for the quick recovery of LOSVD. Throughout this work the penalised pixel fitting (PPXF) method is used to measure the kinematics of a galaxy. The advantage of the PPXF method is that it can correlate more than one absorption feature of the spectrum to calculate the velocity dispersion. This, while it requires high S/N measurements, increases the robustness of the velocity dispersion memasurement. In this thesis we required the PPXF to make velocity dispersion measurements based on at least three absorption lines.

The stellar kinematics of each galaxy are extracted from the reduced spectra. Typically a S/N $\geq$ 50 per resolution element is required for each galaxy to allow for the reliable measurement of LOSVD and the third ($h_3$) and fourth ($h_4$) Gauss-Hermite moments which measure the skewness and kurtosis of the Gaussian fit (van der Marel & Franx, 1993; Bender et al., 1994; Statler, 1995). Most literature values for $\sigma$ for galaxies are based on SDSS observations, whose S/N is usually lower than ~10. Getting a higher S/N observation for these galaxies provides a more secure stellar kinematics measurement.

The Gauss-Hermite polynomials reduce degeneracy in the fitting of the LOSVD because they are orthogonal. The first coefficient $h_1$ is mean velocity, $h_2$ is the velocity dispersion, $h_3$ measures skewness, which is the LOSVD's departure from symmetry and $h_4$ is the kurtosis, which measures the LOSVD's symmetric departure from the Gaussian distribution.

The LOSVD extraction is achieved through the use of PPXF routine (Cappellari & Emsellem, 2004). PPXF uses a library of stellar templates to compose an optimal template as a linear combination of the spectra from the library. This optimal stellar template is then convolved with the LOSVD to find the best fit of the chosen portion of the observed spectrum. For the SALT spectra the MILES stellar library (Sánchez-Blázquez et al., 2006) was used.

There are several other stellar spectra libraries that are available in literature which cover the spectral range of the galaxies in the SALT sample. Some are based on synthetic spectra, which offer excellent spectral resolution, like SYNTHE synthetic library (Munari et al., 2005) and MARCS synthetic library (Gustafsson et al., 2008). Others are based on observed samples of spectra like MILES library of Stellar Spectra (Falcón-Barroso et al., 2011), ELODIE (Prugniel & Soubiran, 2001) and Indo-US Coudé Feed Spectral library (Valdes et al., 2004) which have spectral resolutions that range from 0.5 Å to 2.51 Å.

The MILES stellar library is suitable for the SALT sample based on its coverage of the wavelength range from 3 525 − 7 500 Å at a spectral resolution of 2.51 Å ($FWHM$) using well-calibrated stars. This translates to an uncertainty in velocity dispersion of 64 $\mathrm{km\,s^{-1}}$. The library has 985 stellar templates and thus has extensive coverage of the different stellar spectral types in the given wavelength range. This virtually eliminates the template mismatch problem when using PPXF.

The CCD gaps and the emission lines in the galaxy spectra were ignored using the facility **goodpixels** in PPXF, which allows for the ignoring of regions of the spectrum that would be deemed to contaminate the result. Fig. 3.5 shows all the bestfit PPXF outputs in the SALT sample for all the galaxies (18) for which we found a result. The legend for the figure is found in table 3.4. The rows and the columns in the figure correspond to the rows and the columns in the table such that the spectrum in the first row and third column of the figure is NGC1045 as represented by the corresponding row and column in table 3.4. The width of the absorption lines in the spectrum is used to measure the velocity dispersion of the galaxy. The green dots are the residuals of the fit and the blue line shows where the spectrum is not used for the fit (i.e. the ignored portion of the spectrum.) The SALT resolution is not high enough to allow for the resolution of the SOI of any SMBH in the SALT sample. However, it does allow high S/N measurements of the velocity dispersion $\sigma$ of galaxies in the nearby Universe. Because the $\sigma$ correlates with SMBH mass, it allows the preparatory step in studying the high mass end of the $M_{\mathrm{BH}} - \sigma$ relation. The SOI resolution measurements are usually achieved with HST longslit or IFU spectroscopy assisted with AO as part of the follow up SMBH mass measurement.

Table 3.4: This table is a legend for the figure 3.5. The columns and rows in this table correspond to the columns and rows in the figure.

| | | |
|---|---|---|
| IC4765 | IC5105 | NGC1045 |
| NGC1217 | NGC7196 | NGC1400 |
| NGC5791 | NGC7796 | NGC5796 |
| NGC6861 | IC1356 | NGC6868 |
| NGC6893 | ESO139-026 | NGC7014 |
| ESO137-029 | ESO137-044 | ESO137-008 |

Table 3.5: PPXF systemic velocity and velocity dispersion measurements with S/N ratio.

| Galaxy name | Recessional velocity ( $\mathrm{km\,s^{-1}}$) | Velocity dispersion ( $\mathrm{km\,s^{-1}}$) | S/N ratio |
|---|---|---|---|
| IC 1356 | 8354.9 ± 5.0 | 291.0 ± 5.9 | 89 |
| NGC 7196 | 2886 ± 23 | 277.9 ± 37.5 | 163 |
| NGC 7796 | 3341 ± 15 | 252.9 ± 5.9 | 188 |
| IC 5105 | 5407 ± 15 | 303.0 ± 11.1 | 190 |
| ESO 139-026 | 4968.7 ± 4.6 | 289.7 ± 5.4 | 145 |
| ESO 137-029 | 5405.9 ± 5.0 | 226.7 ± 6.9 | 137 |
| ESO 209-012 | 12090 ± 45 | N/A* | −− |
| NGC 0424 | 3496 ± 20 | N/A* | 43 |
| NGC 1400 | 562.0 ± − − − | 298.0 ± − − − | 251 |
| NGC 7014 | 4762 ± 19 | 291.1 ± 7.9 | 63 |
| NGC 5791 | 3347 ± 12 | 251.6 ± 13.0 | 63 |
| NGC 5796 | 2965 ± 9 | 269.4 ± 6.1 | 145 |
| IC 4765 | 4488 ± 10 | 279.1 ± 5.8 | 82 |
| ESO 137-008 | 3856 ± 19 | 282.4 ± 11.2 | 59 |
| NGC 6868 | 2939.6 ± 3.8 | 307.2 ± 5.0 | 161 |
| NGC 6861 | 2824 ± 18 | 414.0 ± 20.0 | 179 |
| NGC 1217 | 6241 ± 15 | N/A* | 154 |
| NGC 6893 | 3046 ± 26 | N/A* | 269 |
| NGC 1045 | 4617 ± 17 | 312.6 ± 25.2 | 239 |
| NGC 59 | 375 ± 26 | N/A* | |
| ESO 137-044 | 4483.4 ± 9.4 | 499.4 ± 12.1 107 | |

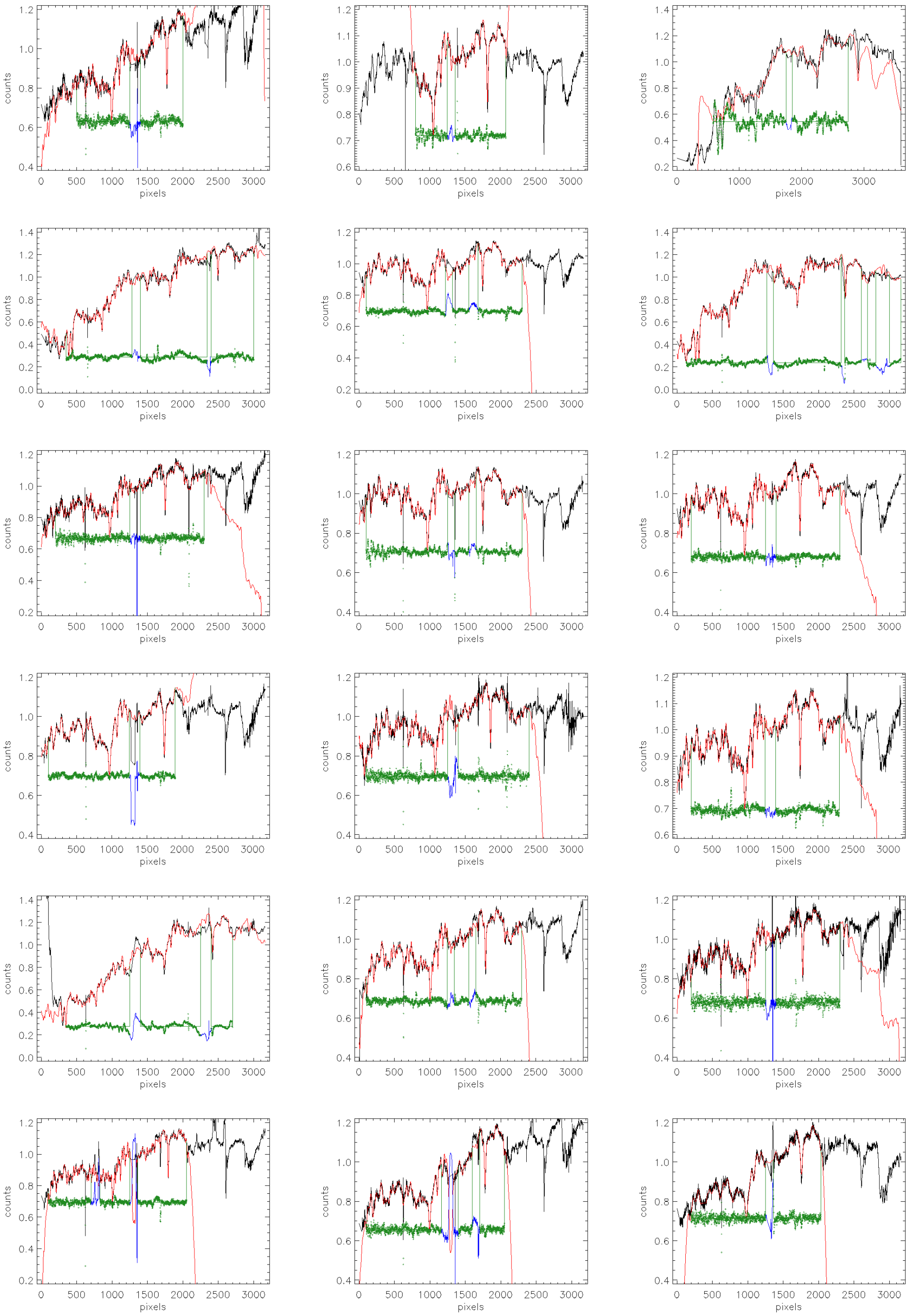

Figure 3.5: An example of the PPXF fitting on all the galaxies for which we found a result. The suitable goodpixel choices are optimised per individual spectrum. The x-axis is in pixel number and the y-axis is in normalised counts. The spectrum is the black line and the PPXF fit is in red. The difference (residuals centered around zero) are shown in green. The names of the particular galaxies in the figure are in table 3.4 below.

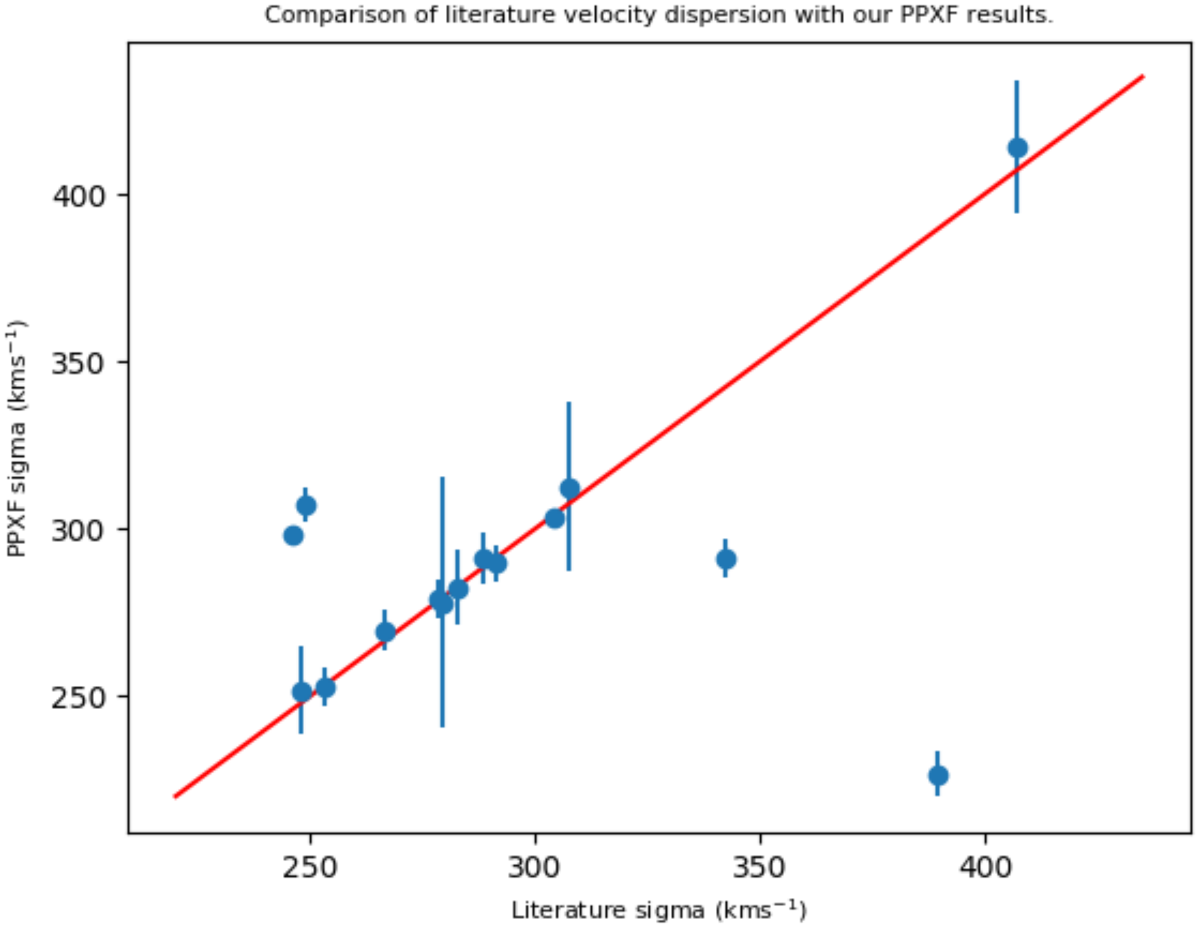

Figure 3.6: A comparison of literature velocity dispersion with the results of the PPXF analysis of the SALT pilot sample. The blue dots represent the literature and PPXF $\sigma$ values with the PPXF error bars. The red line is for equal literature and PPXF values. The majority of the velocity dispersions are in good agreement with HyperLeda results.

## 3.5 Discussion

The systemic velocities of the galaxies in the SALT sample have close values to HyperLeda whilst the errors of SALT PPXF sample are systematically smaller. This suggests that a combination of PPXF, the higher spectral resolution of SALT and the higher S/N ratio calculates the recessional velocity more precisely than previous methods used in HyperLeda.

The S/N ratios of velocity dispersion measurements in literature are often low or not listed at all. PPXF measurements require a minimum S/N of 50 per resolution element. This means that PPXF consistently provides velocity dispersion measurements with good S/N ratio and the use of the DER-SNR algorithm allows the calculation of the S/N ratio in a uniform fashion (Stoehr et al., 2008). This allows the improvement of the homogeneity of the quality of the velocity dispersion measurements even in cases where different telescopes are used.

Fig. 3.6 shows that most velocity dispersion measurements in the SALT sample are very similar to literature values with a few outliers. In Fig. 3.6, literature velocity dispersions are compared with the results of the PPXF analysis of the SALT pilot sample. This plot combines column three of Table 3.1 and column three of Table 3.5. The blue dots represent the literature and SALT $\sigma$ values with the error bars being derived from the SALT results. The red line is for equal literature and PPXF values (i.e. the closer a point is to this line, the closer the HyperLeda $\sigma$ values are to the results measured in this work). The majority of the velocity dispersions are in good agreement with HyperLeda results.

The uncertainties in HyperLeda velocity dispersion measurements have a direct impact on how the SMBH mass is predicted. In the HETMGS survey, for instance, 17% of the 100 galaxies that are predicted to have an SMBH SOI $\geq 0\overset{''}{.}10$ were found to have an SOI $\leq 0\overset{''}{.}08$ (van den Bosch et al., 2015). The SALT sample of high $\sigma$ ETGs suffers from these uncertainties due to the fact that HyperLeda $\sigma$ measurements for velocity dispersion values greater than 300 $\mathrm{km\,s^{-1}}$ are often too large by a significant amount (van den Bosch et al., 2015) and this is an effect that is seen in the outliers too. They tend to have HyperLeda $\sigma$ values that are too high. This could be the reason for the outliers in the SALT sample, as the results are in agreement with the anomalies found in van den Bosch et al. (2015).

An illustration of the uncertainties in HyperLeda is that for NGC 6868 there are 12 literature measurements of $\sigma$ ranging from 242.1 ±11.7 $\mathrm{km\,s^{-1}}$ to 314.0 $\mathrm{km\,s^{-1}}$. Its latest measurement is

284.1±6.6 km s$^{-1}$ by Campbell et al. (2014). HyperLeda lists the velocity dispersion of NGC 6868 as 252.3±4.0 km s$^{-1}$. This necessitates the finding of a consistent database of velocity dispersion measurements.

The common feature amongst the outliers is that they all seem to show emission lines, some low luminosity, like NGC 1400 and IC 1356, whereas others have high luminosity, like the H$\beta$,[NII] doublet at $\tilde{6}$600Å in NGC 6868 and ESO 137-029. These will be followed up with PPXF and Gas AND Absorption Line Fitting algorithm (GANDALF) which handles galaxy spectra that shows both emission and absorption lines. The errors in velocity dispersion are systematically smaller than HyperLeda which suggests that the conclusions made from the systemic velocity measurements are borne out. This suggests that measurements in the SALT sample provide an improvement.

The potential sources of the difference in the measurements between the HyperLeda values and the PPXF measurements include the slight dependence of PPXF velocity dispersion measurements on the Stellar Library used (Lalovic, 2010). Since only MILES stellar library is used, this effect cannot be quantified and deconvolved from the other potential causes. The better resolution of the SALT telescope and the better S/N ratio of the observed spectra may also have an effect on the velocity dispersion measurement. The better resolution and improved S/N ratio do improve the errors in the measurement and might be the primary reason for the improved error in the PPXF measurements.

HyperLeda velocity dispersion values are calculated from the average literature velocity dispersion values. These are usually from different S/N spectra and different telescopes with different spectral resolutions. This makes it impractical to quantify the contributions of the different effects listed above. Such a study is needed and would require more high S/N SALT spectra of HyperLeda galaxies.

The galaxy NGC6861 is singled out for further study with stellar kinematics techniques in the next chapter. It is a prime candidate for further study because it has a high $\sigma$ and is close enough in distance that it may be resolved with current IFU telescopes with AO instruments.

# Chapter 4

# Blackhole mass measurement : A multimodal Bayesian parameter estimation

## 4.1 Introduction

The correlations between the SMBH mass and characteristics of the host galaxy, such as velocity dispersion, bulge luminosity and Sersic profile, are standard methods of estimating the central mass (Kormendy & Ho, 2013). However, the measurement of the actual SMBH mass still has to be done. The observables mentioned earlier are thus good selection criteria to use for compiling samples of SMBH masses to measure. This is useful when considering the high cost in telescope time required for SMBH mass measurements. This chapter discusses the stellar dynamical method of SMBH mass measurement using Bayesian parameter estimation and JAM mass measurement method.

In this chapter we look at Bayesian method of parameter estimation applied to Jeans anisotropic multi-Gaussian (JAM) models. The JAM method of dynamical SMBH mass measurement has been superceded by the Schwarzschild orbit superposition method for dynamical mass measurements, however it still remains a useful too for SMBH mass measurement as it has a good correlation with other state of the art SMBH mass measurement methods. Studying the centres of ETGs provides an opportunity to explore relationships between their SMBH masses and such global properties as star formation history and galaxy mass. This may ultimately lead to a better understanding of the correlation between the mass of the SMBH and galaxy formation (Silk & Rees, 1998).

An IFU spectrograph with AO can be used to perform two-dimensional spectroscopy of a galaxy core with a spatial resolution ranging from $0\farcs025$ to $0\farcs25$, corresponding to a field-of-view ranging from $0\farcs8 \times 0\farcs8$ to $8'' \times 8''$ in 8 m class optical telescopes (Eisenhauer et al., 2003). Despite that limited field of view, the kinematic profiles of galaxies in the vicinity of the SMBH can be determined, which puts constraints on the mass of the blackhole. With the new generation of large optical telescopes, with apertures greater than 15 m, and AO technology, resolutions of $0\farcs01$ will be possible and sensitivity will be improved. This will improve the SMBH mass coverage in the local Universe by reducing the lower limit of the SMBH mass sample and enable the detection of high mass SMBHs that are further away. This will improve the statistics of measured SMBH.

In lenticular and spiral galaxies the SMBH mass correlates with the mass of the spheroidal component of the galaxy. The spheroidal component can be a classical bulge or a pseudobulge depending on its photometric characteristics. Differences between classical bulges and pseudobulges are discussed below. There has been an observed difference in the correlation between the SMBH mass and the mass of classical bulges and pseudobulges. The $M_{\rm BH} - \sigma$ and the $M_{\rm BH} - M_{\rm bulge}$ relations both have smaller error bars when a sample that only has classical bulges is used in the relation (Kormendy & Ho, 2013). Consequently, it is important to identify the disc-like pseudobulges and remove them from the sample for follow-up IFU observations.

### 4.1.1 Stellar dynamical modelling

In this method, spectroscopy is used to measure the profile of absorption lines formed in stellar atmospheres. The profiles are broadened by the collective motion of the ensemble of stars being observed. The broadened profile is assumed to be related to the dynamical velocity distribution of the stars. Photometric measurements of the galaxy are made to determine the surface brightness of the galaxy. The surface brightness is assumed to be related to the stellar mass distribution in the galaxy. By modelling the velocity distribution of the stars using the collisionless Boltzmann equation, combined with the mass distribution assumed from the surface brightness, the observed line profiles can be fitted by varying the $M/L$ ratio. This can then be used to infer a SMBH mass. Note that the recovery of the mass distribution function (DF) of a stellar system using only the line-of-sight quantities does not offer a unique solution.

The initial stellar dynamical mass measurements were almost always over-estimates. This is due to a combination of insufficient S/N and insufficient telescope resolution (Tonry, 1984). Once longslit spectroscopy was separated from atmospheric seeing through the use of HST STIS, it was discovered that, for instance, the central velocity dispersion of M32 is largely due to the blending of the blue shifted and red shifted components of the central rotational velocity.

The stellar dynamical modelling method of measurement was first claimed to measure the SMBH mass of M87 (Sargent et al., 1978; Young et al., 1978). It was subsequently confirmed for M32, when the HST provided sufficient resolution for the measurements to be reasonably secure Tonry (1984, 1987). The initial assumption, in that seminal work, was isotropic stellar velocity distribution. Although isotropy is unlikely, their results of $\sim 10^9$ $\mathrm{M}_\odot$ were confirmed using HST spectroscopic emission line data (Harms et al., 1994).

The major observational drawback of absorption line dynamics in ETGs, is that the surface brightness falls off quickly away from the galaxy core, leading to a low S/N ratio for the absorption lines in most of the galaxy.

From a modelling perspective, any unknown anisotropies of the stellar velocity distribution create problems in constraining the SMBH mass (Kormendy & Ho, 2013). This was established early as a challenge in the Jeans modelling because of the assumption that the galaxy is axisymmetric and it was mitigated by choosing galaxies that are more edge-on because of their low anisotropy (Tonry, 1984, 1987; Kormendy, 1988b,a).

The effect of this anisotropy on different types of classical bulges is illustrated below with the idealised example from Kormendy & Richstone (1995), of a spherically symmetric velocity ellipsoid that everywhere points at the centre. The collisionless Boltzmann equation's first velocity moment gives the mass $M(r)$ enclosed within radius $r$ as

$$M(r) = \frac{V^2 r}{G} + \frac{\sigma_r^2 r}{G}\left[-\frac{d\mathrm{ln}\nu}{d\mathrm{lnr}} - \frac{d\mathrm{ln}\sigma}{d\mathrm{lnr}} - \left(1 - \frac{\sigma_\theta^2}{\sigma_r^2}\right) - \left(1 - \frac{\sigma_\phi^2}{\sigma_r^2}\right)\right] \ , \tag{4.1}$$

where $V$ is the rotational velocity, $G$ is the gravitational constant, $\nu$ is the density of the tracer population whose velocity dispersion is being measured and $\sigma_r$, $\sigma_\theta$, $\sigma_\phi$ are the radial and azimuthal components of the velocity dispersion. The four terms inside the square bracket influence the value of the $\sigma_r^2$ term on the mass $M(r)$. The first two terms are usually positive whereas the last two (anisotropy) terms can be either negative or positive.

Core galaxies have shallow inner profiles with $0.5 \leq -\frac{d\ln\nu}{d\ln r} \leq 1$ (Gebhardt et al., 1996) and $-\frac{d\ln\sigma}{d\ln r}$ generally less than 1, whereas coreless galaxies have $-\frac{d\ln\nu}{d\ln r} \simeq 1.9 \pm 0.3$ and $-\frac{d\ln\sigma}{d\ln r}$ larger than in core galaxies (Kormendy & Ho, 2013). This results in the first two terms being $1 - 1.5$ for core galaxies and $\simeq 3$ for coreless galaxies. This problem can be solved by observing different mass tracers from the same part of a galaxy (Koopmans, 2006; Czoske et al., 2008; Barnabè et al., 2009, 2010), but in dark matter dominated parts of the galaxy it still cannot be resolved.

Currently, the most common method for determining SMBH mass using stellar dynamics in AGN cores is the dynamical modelling based on the Schwarzschild orbit superposition (Schwarzschild, 1979). Made-to-measure N-body SMBH mass modelling methods (Syer & Tremaine, 1996) are the most recent. However, these methods are not predictive and their results depend on how each method is implemented.

Jeans Anisotropic Multi-Gaussian (JAM) dynamical models are an SMBH mass measurement method that is capable of reproducing results in good agreement with the Schwarzschild dynamical models (Drehmer et al., 2015; Cappellari et al., 2010; Krajnović et al., 2009). There are known degeneracies in solving JAM models (Cappellari et al., 2007; Diakogiannis et al., 2014a), the resolution of which is still being investigated (Diakogiannis et al., 2014b).

The Schwarzschild and the made-to-measure models have become the preferred methods recently because they are more general. JAM models offer an advantage over the other two methods because they are predictive.

Initially, the JAM dynamical models were implemented using $\chi^2$ minimization of each parameter separately, which gives a local minimum but not necessarily a global minimum. To address this problem, they were then implemented using a Bayesian method to solve this multi-variate problem (Cappellari et al., 2013). In the next use the JAM modelling with Bayesian statistics to model the mass of the SMBH in the core of NGC 6861. In the next section the mathematical framework of Bayesian parameter estimation is discussed.

## 4.2 Bayesian parameter estimation

For most of the twentieth century, science has used a frequentist approach to statistics, where probability is defined as the relative frequency with which a result may be attained, given an infinite number of trials. Bayesian methods are being used increasingly due to the availability of computational power and their recognised theoretical soundness. The challenge of parameter estimation in the context of SMBH mass measurement is that it seeks to fit for several variables simultaneously. Markov Chain Monte Carlo (MCMC) techniques offer a computationally efficient way to numerically approximate a posterior distribution.

### 4.2.1 Bayes theorem

$P(X)$ is defined as the probability over all the values of a discrete variable $X$. The assumptions are that all the values of $X$ have positive non-zero probabilities,

$$P(X) > 0 \, \forall \mathrm{X} \ , \tag{4.2}$$

and the sum of all probabilities of $X$ is 1,

$$\Sigma P(X) = 1 \ . \tag{4.3}$$

The two fundamental rules of probability are the sum rule and the product rule. The sum rule states that the probability $P(X)$ of a proposition $X$ being true and the probability $P(\overline{X})$ of $X$ being false add up to 1.

$$P(X|H) + P(\overline{X}|H) = 1 \ , \tag{4.4}$$

where $H$ is any relevant background information. The product rule stipulates that the probability of two propositions $X$ and $Y$ being both true equals the conditional probability that $X$ is true given that $Y$ is true, multiplied by the probability that $Y$ is true.

$$P(X|Y,H)P(Y|H) = P(X,Y|H) = P(Y|X,H)P(X|H) \tag{4.5}$$

Since the probability of $X$ and $Y$ being true $P(X,Y|H)$ is the same as the probability of $Y$ and $X$ being true $P(Y,X|H)$ the equation combining eqn (4.5) for them gives

$$P(X|Y,H) = \frac{P(X|H)P(Y|X,H)}{P(Y|H)} \ . \tag{4.6}$$

This is the form that Bayes' rule takes. $P(X|Y,H)$ is called the posterior probability and is a measure of the belief in proposition after the data under study has been analysed. $P(X|H)$ is called the prior probability and represents the belief in the proposition prior to the data being analysed. $P(Y|X,H)$ is called the likelihood function and captures how the uncertainties in the measurement process are distributed. The final term $P(Y|H)$, is referred to as marginal likelihood or evidence.

The evidence is essential when Bayesian statistics is used for model selection. For applications in parameter estimation, however, the evidence acts as a normalisation constant and does not affect the shape of the posterior distribution.

This chapter discusses a Bayesian parameter estimation approach to running JAM models. It is then applied to both spherical and axisymmetric models of a Hernquist toy model with a central dark mass to investigate how well the JAM models can retrieve parameters that are known *a priori* and how the degeneracies in the modelling affect the results. MultiNest, a numerical sampling tool based on the nested sampling algorithm (Skilling, 2004), is used to solve for the parameters in JAM models.

### 4.2.2 Marginalisation

If the previous example from eqn (4.5) is extended and a conditional probability is defined, such that proposition $X$ is false and $Y$ is true $(P(\overline{X},Y|H))$, eqn (4.5) becomes

$$P(\overline{X}|Y,H)P(Y|H) = P(\overline{X},Y|H) = P(Y|\overline{X},H)P(\overline{X}|H)\ . \tag{4.7}$$

The sum rule can be restated as

$$P(X|Y,H) + P(\overline{X}|Y,H) = 1\ . \tag{4.8}$$

Combining eqns (4.7) and (4.5) one gets

$$P(X,Y|H) + P(\overline{X},Y|H) = [P(X|Y,H) + P(\overline{X}|Y,H)]P(Y|H)\ . \tag{4.9}$$

The right hand side can be simplified because the term in square brackets is 1 due to the sum rule in eqn (4.8). This can be written as

$$P(Y|H) = \sum_{k=1}^{N} P(X, Y_k|H) \ . \tag{4.10}$$

where $N$ is the total number of discrete parameter values that $Y$ can take on. Eqn (4.10) is the marginal likelihood or evidence. It is of great use in model selection as it is used to compare the plausibility of different models. It has limited use in parameter estimation as it is used there only as a normalising factor. In this study the use of the evidence is optional. It is used to choose parameter estimation results as different runs yield slightly different results. An example is a result where the M/L ratio and the SMBH mass parameters converge to an answer in one run, whereas in another run only the SMBH mass converges to an answer. Whereas, reporting the former result might be desirable, it is only prudent to do so if the evidence supports that as a better result.

## 4.3 Models and data

Elliptical galaxies, globular clusters and galaxy bulges have been known for a long time to follow the light distribution of

$$\log_{10}\left[\frac{I(R)}{I(R_e)}\right] = -3,331\left[\frac{R}{R_e} - 1\right] \ , \tag{4.11}$$

where $I$ is the surface brightness, $R$ is the radius projected onto the plane of the sky and $R_e$ is the effective radius of the isophote enclosing half of the galaxy light (de Vaucouleurs, 1948).

The de Vaucouleur profile, despite its accuracy in representing the surface brightness profile of ETGs, has a limitation of not being easy to represent the deprojected mass density $\rho(r)$ in analyses e.g. (Young et al., 1978). This necessitated the finding of other ways to represent the surface brightness profiles of these galaxies in terms of their mass density profiles (Michie & Bodenheimer, 1963; King, 1966; Jaffe, 1983; Hernquist, 1990; Navarro et al., 1997).

### 4.3.1 Hernquist kinematic models

To solve the problem of Jaffe models (Jaffe, 1983), which deviate from the de Vaucouleur's profile as radius approaches zero, Hernquist (1990) proposed a density distribution model defined by

$$\rho(r) = \frac{M}{2\pi}\frac{a}{r}\frac{1}{(r+a)^3} \ , \tag{4.12}$$

where $M$ is the total halo mass of the galaxy, $r$ is the radius and $a$ is a scale length.

We chose a toy model that is spherical because it is conveniently represented by Hernquist analytical models and a mass that is comparable to the stellar mass of the Milky Way Galaxy. We create an input Hernquist model of a spherical elliptical galaxy that has the following parameters,

- Total galaxy mass : $1.3 \times 10^{11}$ $\mathrm{M}_{\odot}$
- Blackhole mass : $2.3 \times 10^{9}$ $\mathrm{M}_{\odot}$
- Inclination angle : 45°
- $\mathbf{a} = 3.0 \times 10^3\,\mathrm{pc}$
- Mass to light ratio ($\Upsilon$) is assumed to be $1\frac{\mathrm{M}_{\odot}}{\mathrm{L}_{\odot}}$

Fig. 4.1 shows the velocity of stars in the gravitational potential of the input model as a function of radius. The simulation will attempt to reproduce this plot by using the JAM model with different combinations of parameters.

### 4.3.2 MultiNest

MCMC techniques are designed to traverse multimodal parameter spaces in a way that saves time and can quantify the evidence. MCMC has proved to be one of the most successful algorithms in the 21st century (Dongarra & Sullivan, 2000). One of the drawbacks of MCMC is the computational cost for evidence computation and this is an area where MultiNest offers an improvement.

Nested sampling (Skilling, 2004, 2006; Sivia & Skilling, 2006) is a Monte Carlo method that

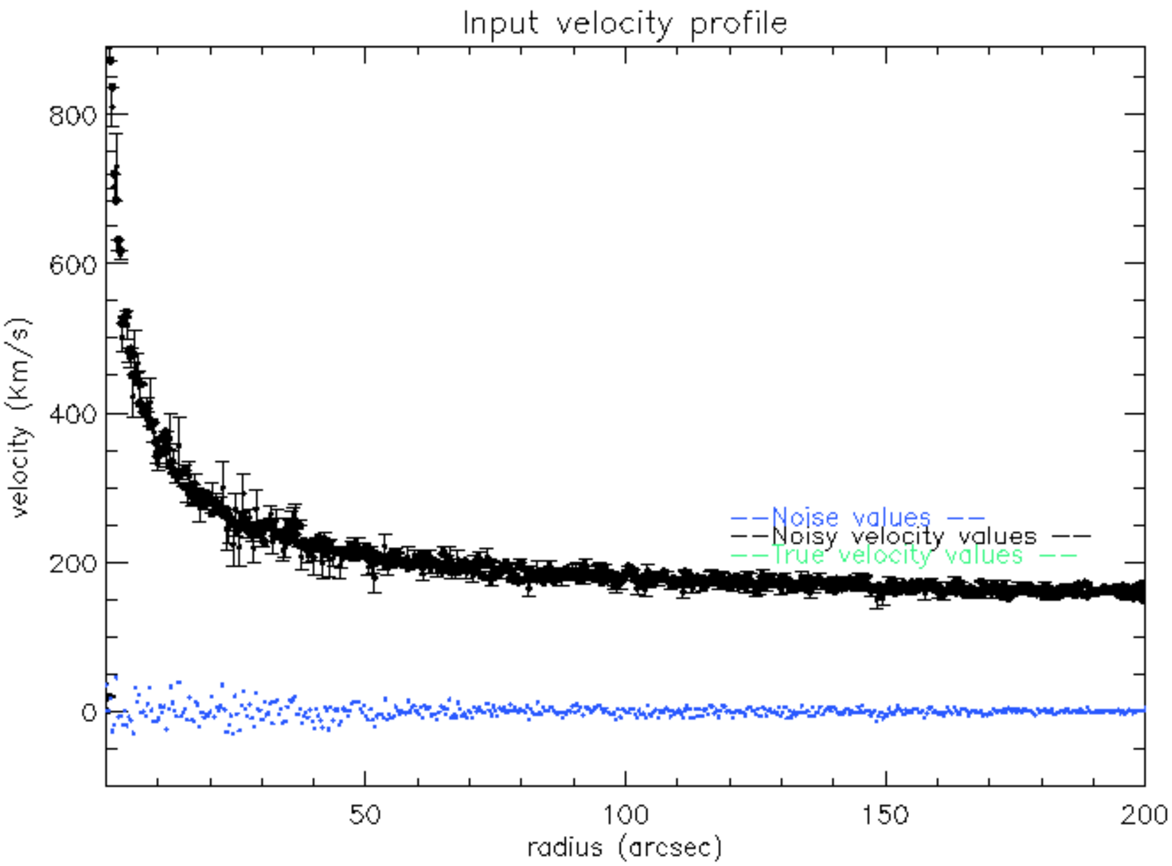

Figure 4.1: The kinematics of the input Hernquist model as a function of radius.

can be used for efficient computation of Bayesian evidence and provides posterior inferences. It transforms the multidimensional evidence integral

$$\mathcal{Z} = \int \mathcal{L}(\Theta)\pi(\Theta)d^N\Theta \ , \tag{4.13}$$

where $\mathcal{L}(\Theta)$ is the likelihood and $\pi(\Theta)d^N\Theta$ is the N-dimensional prior, into a one-dimensional integral by exploiting the relation between the likelihood and prior volume (Feroz & Hobson, 2008; Feroz et al., 2009). This algorithm has been implemented in MultiNest, which has found use in science, including several astronomy problems (Feroz et al., 2009; Bridges et al., 2009; Lochner et al., 2015; Feroz et al., 2009; Natarajan et al., 2017; Zwart et al., 2015).

## 4.4 JAM modelling

JAM modelling is achieved by solving the Jeans equations (Jeans, 1922) for the shape of the velocity ellipsoid of the galaxies. Its detailed derivation in spherical and axisymmetric forms is treated in Binney & Tremaine (2008).

JAM method has been used successfully for the mass measurement of SMBH (Cappellari et al., 2013) in galaxies in the nearby Universe. It relies on the $\chi^2$ minimization of the difference between the observed velocities and the JAM model velocity distribution.

According to the hierarchical structure formation scenario, massive galaxies are formed via mergers (Springel et al., 2005). These mergers are followed by changes in the structure and morphology of the resultant galaxy. ETGs (Es and S0s), whose blackhole masses will ultimately be measured, are believed to be formed by either gas-rich merging or by gas starvation of spiral galaxies followed by collisionless mergers (Faber et al., 2007).

A typical Milky Way sized galaxy has of the order $10^{11}$ stars and has had a few hundred crossing times in its lifetime. Because of the mean free path of stars in galaxies, the collisions between stars are not important in the dynamics of the stars. The galaxy can thus be treated as a collisionless system. The problem is viewed as a probability distribution function (PDF) $f(\mathbf{x},\mathbf{v},t)$ in six dimensional phase space $(\mathbf{x},\mathbf{v})$ where $\mathbf{x}$ represents the three dimensional spatial elements x, y, z and $\mathbf{v}$ are the velocity components $v_x\, v_y\, v_z$.

The majority of galaxies in the Universe, with the exception of bars but including fast-rotator ETGs and spiral galaxies, are axisymmetric and possess discs (Cappellari et al., 2007; Emsellem et al., 2007). Four global parameters are key to the characterisation of galaxy structure when studying the merging of galaxies and dark matter viz.,

- angular momentum, which increases with the amount of gas dissipation and varies during mergers.
- stellar population, which records the star formation history of the galaxy during gas-rich mergers.
- mass-to-light ratio ($\Upsilon$), which is affected by the stellar population and the dark matter fraction.

- The type of merger (wet or dry), which determines the amount of gas available for star formation after ther merger.

### 4.4.1 Solving the axisymmetric Jeans equation

When solving a system $\mathbf{f}(\mathbf{x},\mathbf{v})$ in steady-state under a smooth gravitational potential $\Phi$, the DF $\mathbf{f}(\mathbf{x},\mathbf{y})$ describes the probability that a star at position $\mathbf{x}$ has a velocity $\mathbf{v}$ of all the stars in the system. The DF must satisfy the steady-state collisionless Boltzmann equation (Binney & Tremaine, 2008). This analysis is covered in both Cappellari (2008) and Binney & Tremaine (2008). The collisionless Boltzmann equation,

$$\sum_{i=1}^{3}\left(v_i\frac{\partial f}{\partial x_i}-\frac{\partial \Phi}{\partial x_i}\frac{\partial f}{\partial v_i}\right)=0\ , \tag{4.14}$$

where $\Phi$ is the gravitational potential, $x_i$ and $v_i$ are the Cartesian coordinates for distance and velocity respectively, is a function of six variables that has an infinite family of solutions. To solve it, further simplifications and assumptions are needed to provide a practical application of the equation. One such way is to reduce it to only consider velocity moments instead of recovering the DF. This leads to the Jeans equation.

Eqn (4.14) can be written in standard cylindrical coordinates $(R,z,\phi)$ and assuming axial symmetry i.e. $\frac{\partial \Phi}{\partial \phi}=\frac{\partial f}{\partial \phi}=0$ to get

$$v_R\frac{\partial f}{\partial R}+v_z\frac{\partial f}{\partial z}+\left(\frac{v_\phi^2}{R}-\frac{\partial \Phi}{\partial R}\right)\frac{\partial f}{\partial v_R}-\frac{\partial \Phi}{\partial z}\frac{\partial f}{\partial v_z}-\frac{v_R v_\phi}{R}\frac{\partial f}{\partial v_\phi}=0\ . \tag{4.15}$$

Multiplying eqn (4.15) by $v_R$ and $v_z$ and integrating over all velocities will give the two Jeans equations (Jeans, 1922). A third Jeans equation falls away because it has all the terms that involve the multiplication by $v_\phi$ being equal to zero due to the axisymmetry condition.

The algorithm of the axisymmetric Jeans equation in cylindrical coordinates that is discussed in Cappellari (2008) is used to prove that when used together with Bayesian statistics and an MCMC algorithm it gives a more complete sampling of the multi-dimensional parameter space than the traditionally used $\chi^2$ minimisation. The axisymmetric Jeans equation in cylindrical coordinates is written as

$$\frac{\nu\overline{v_R^2} - \nu\overline{v_\phi^2}}{R} + \frac{\partial(\nu\overline{v_R^2})}{\partial R} + \frac{\partial\nu\overline{v_R v_z}}{\partial z} = -\nu\frac{\partial\Phi}{\partial R}\ , \tag{4.16}$$

and

$$\frac{\nu\overline{v_R v_z}}{R} + \frac{\partial(\nu\overline{v_z^2})}{\partial z} + \frac{\partial\nu\overline{v_R v_z}}{\partial R} = -\nu\frac{\partial\Phi}{\partial z}\ , \tag{4.17}$$

where the shorthand notation used is

$$\nu\overline{v_k v_j} \equiv \int v_k v_j f d^3\mathbf{v}\ . \tag{4.18}$$

If constant anisotropy is assumed throughout the galaxy such that $\overline{v_R^2} = b\overline{v_z^2}$ and the velocity ellipsoid is aligned with the cylindrical coordinates, the above equations reduce to

$$\frac{b\nu\overline{v_z^2} - \nu\overline{v_\phi^2}}{R} + \frac{\partial b\nu\overline{v_z^2}}{\partial R} = -\nu\frac{\partial\Phi}{\partial z}\ , \tag{4.19}$$

and

$$\frac{\partial(\nu\overline{v_z^2})}{\partial z} = -\nu\frac{\partial\Phi}{\partial R}\ . \tag{4.20}$$

The root-mean-square (rms) velocity as a function of radius in the galaxy ($V_{\rm rms}^2 = V^2 + \sigma^2$), where $V$ is the mean stellar velocity and $\sigma$ the velocity dispersion at a given radius, can be very well approximated with the second velocity moment $\overline{v_{\rm los}^2}$. Cappellari (2008, eqn 28) gives the second velocity moment as

$$\sum\overline{v_{\rm los}^2}(x',y') = 4\pi^{\frac{3}{4}}G\int_0^1\sum_{k=1}^{N}\sum_{j=1}^{M} v_{0k}\,q_j\,\rho_{0j}\,u^2 \times \frac{\sigma_k^2\,q_k^2(\cos^2 i + b_k\sin^2 i) + \mathcal{D}\,x'^2\sin^2\mathrm{i}}{(1-\mathcal{C}u^2)\sqrt{(\mathcal{A}+\mathcal{B}\cos^2 i)[1-(1-q_j^2)u^2]}} \times \exp\left[-\mathcal{A}\left(\mathrm{x}'^2 + \frac{(\mathcal{A}+\mathcal{B})\mathrm{y}'^2}{\mathcal{A}+\mathcal{B}\cos^2\mathrm{i}}\right)\right]\mathrm{du}\ , \tag{4.21}$$

where

$$\begin{aligned}
\mathcal{A} &= \frac{1}{2}\left(\frac{u^2}{\sigma_j^2} + \frac{1}{\sigma_k^2}\right) && (4.22)\\
\mathcal{B} &= \frac{1}{2}\left(\frac{1-q_k^2}{\sigma_k^2\, q_k^2} + \frac{(1-q_j^2)u^4}{\sigma_j^2[1-(1-q_j^2)u^2]}\right) && (4.23)\\
\mathcal{C} &= 1 - q_j^2 - \frac{\sigma_k^2\, q_k^2}{\sigma_j^2} && (4.24)\\
\mathcal{D} &= 1 - b_k\, q_k^2 - [(1-b_k)\mathcal{C} + (1-q_j^2)b_k]u^2 \ . && (4.25)
\end{aligned}$$

The $\chi^2$ minimisation in the axisymmetric JAM algorithm is evaluated by comparing the theoretical rms velocities calculated using the Jeans method with the 'observed' velocities in the input Hernquist model in a chosen region that has a good S/N ratio (in the case of the Hernquist model, the full model may be used as there is no noise.) The reduced $\chi^2$ statistic is calculated as

$$\chi^2 = \frac{1}{N}\sum_{0}^{N}\frac{(\text{Obs-JAM})^2}{(\text{Error})^2}\ , \qquad (4.26)$$

where $N$ is the number of measurement points of the velocities, Obs are the observed velocities as a function of radius, JAM are the velocities predicted by the JAM model with the given values of SMBH mass, velocity anistropy, $M/L$ ratio and inclination angle. Error represents the difference as measured between the observed and the predicted velocities. The predicted velocities are calculated with eqn (4.21) and the observed velocities come from the Hernquist model as seen in Fig. 4.1.

### The prior distribution and likelihood

The problem of the minimisation of the difference between the observed velocities and the JAM model velocity distribution is solved using MultiNest by revisiting eqn (4.6) and setting the prior distribution as specified in Table 4.1. Here three of the four parameters are set as flat priors and only the SMBH mass prior is set up in logarithmic scale due to its spanning several orders of magnitude.

JAM-Axi-A is a flat prior that is based on all that is known about ETGs whose SMBH mass measurements are done with JAM models. SMBHs have a mass $10^6 \leq M_{\rm BH} \leq 10^{10.5}$ according to observations and an inclination angle of less than 30° is difficult to measure the velocity

Table 4.1: Prior ranges used for the various parameters of the different JAM models.

| Model name | Velocity anisotropy ($\beta_z$) | Inclination angle (deg) | $M/L$ ratio ($\frac{\mathrm{M}_\odot}{\mathrm{L}_\odot}$) | SMBH mass ( $\mathrm{M}_\odot$) |
|---|---|---|---|---|
| JAM-Axi-A | [-0.5: 0.5] | [30 : 90] | [0.1:5] | [$10^6$ : $10^{10.5}$] |
| JAM-Axi-B | [-0.5: 0.5] | [40 : 55] | [0.1:5] | [$10^6$ : $10^{10.5}$] |
| JAM-Axi-C | [-0.1: 0.1] | [30 : 90] | [0.1:5] | [$10^6$ : $10^{10.5}$] |
| JAM-Axi-D | [-0.1: 0.1] | [40 : 55] | [0.1:5] | [$10^6$ : $10^{10.5}$] |
| JAM-Axi-E | [-0.5: 0.5] | [30 : 90] | [08:1.2] | [$10^6$ : $10^{10.5}$] |

dispersion because it is too face-on. The range of inclination angles will, therefore be limited between that and completely edge-on (30° $\leq$ inclination angle $\leq$ 90°). The velocity anisotropy range $-0.5 \leq \beta_z \leq 0.5$ applies for all ETGs. The $M/L$ ratio is limited to $0.1 \leq \upsilon \leq 5$ because it is known *a priori* that it is 1.0 (Binney & Tremaine, 2008). If that were not known, increasing range to 10.0 or above, would be justified. In JAM-Axi-B the inclination angle is limited to 40° $\leq$ inclination angle $\leq$ 55° based on the results of JAM-Axi-A. Based on the results of JAM-Axi-B the prior range of $\beta_z$ is expanded to $-0.1 \leq \beta_z \leq 0.1$. This allows for an investigation of the velocity anisotropy parameter $\beta_z$ in JAM-Axi-C and JAM-Axi-D. With a constrained inclination angle and velocity anisotropy result in JAM-Axi-D the prior range in JAM-Axi-E is used to constrain the SMBH mass.

MultiNest calculates $\chi^2$ for the JAM model under evaluation using the likelihood function ($\mathcal{L}$) as follows

$$\mathcal{L}(\Theta|Obs, H) = \frac{1}{(2\pi\sigma^2)^{\frac{N}{2}}}\exp\left(\frac{-\chi^2}{2}\right) \ , \tag{4.27}$$

where $\mathcal{L}(\Theta|Obs, H)$ is the likelihood function and N is the number of radial points where the observations are evaluated. In MultiNest the likelihood is expressed in logarithmic form as

$$\ln\mathcal{L} = \ln\left[(2\pi\sigma^2)^{\frac{N}{2}}\right] - \frac{\chi^2}{2} \ , \tag{4.28}$$

which is evaluated at every iteration. These are used to evaluate the posterior distribution which is represented in the results below.

### 4.4.2 Mass Modelling with MGE

MGE is a series expansion of galaxy images using two-dimensional (2D) Gaussian functions (Cappellari, 2002). The Gaussian functions are useful because both the convolution of the point spread function (PSF) and the deprojection of the observed galaxy photometry to get the intrinsic

Table 4.2: MGE surface brightness profile for the input model.

| Surface brightness $(I)$ $(L_{\odot}pc^{-2})$ | Sigma $(\sigma)$ | Axial ratio $q_j$ |
|---|---|---|
| 3472.42 | 4.24264 | 1.00 |
| 3142.11 | 8.76991 | 1.00 |
| 3006 | 17.249 | 1.00 |
| 2952.64 | 33.3016 | 1.00 |
| 2901.39 | 63.6555 | 1.00 |
| 2815.77 | 120.218 | 1.00 |
| 2655.03 | 222.934 | 1.00 |
| 2356.75 | 402.667 | 1.00 |
| 1868.47 | 704.025 | 1.00 |
| 1246.74 | 1191.75 | 1.00 |
| 676.846 | 1965.79 | 1.00 |
| 301.115 | 3185.8 | 1.00 |
| 113.785 | 5110.47 | 1.00 |
| 38.3325 | 8201.49 | 1.00 |
| 11.9323 | 13639.2 | 1.00 |
| 2.92862 | 26990.7 | 1.00 |

stellar luminosity density, can be easily achieved analytically (Emsellem et al., 1994). The MGE formalism is a simple parameterisation that is still general enough to be able to realistically reproduce the surface brightness profiles of multicomponent galaxies like spirals and lenticulars. This provides a huge advantage over the Fourier transform methods of ellipse fitting as MGE can easily represent deviations from elliptic isophotes, which are prevalent in lenticular galaxies and pseudo-bulges (Cappellari, 2002).

It has been used to model many galaxies (Emsellem et al., 1994; Cappellari et al., 2013). This algorithm has been converted into a robust and easy to use code for dynamical modelling of galaxies, available in both IDL and Python computer languages (Cappellari, 2002).

The MGE formalism solves photometric models using concentric Gaussians with a circular point spread function (PSF). Consider a system of coordinates $(x', y', z')$, centered on the nucleus of the galaxy, with $z'$ being along the line of sight. The projected MGE surface brightness profile $(\sum(R', \theta'))$ can be represented as

$$\sum(R', \theta') = \sum_{j=1}^{N} \frac{L_j}{2\pi\sigma_j^2 q_j'} exp\left[-\frac{1}{2\sigma_j^2}(x_j'^2 + \frac{y_j'^2}{q_j'^2})\right] \ . \tag{4.29}$$

Table 4.3: Different results for the Models.

| Model name | $\beta_z$ | Inclination angle (°) | $M/L$ ratio ($\frac{\mathrm{M}_\odot}{\mathrm{L}_\odot}$) | SMBH mass ( $\mathrm{M}_\odot$) |
|---|---|---|---|---|
| JAM-Axi-A | $-0.348 \pm 0.0475$ | $47.77 \pm 5.54$ | $0.214 \pm 0.079$ | $10^{10.13 \pm 0.223}$ |
| JAM-Axi-B | $-0.463 \pm 0.0364$ | $47.71 \pm 3.36$ | $0.1968 \pm 0.0074$ | $10^{10.153 \pm 0.018}$ |
| JAM-Axi-C | $-0.083 \pm 0.0178$ | $75.20 \pm 11.6$ | $0.2409 \pm 0.0066$ | $10^{10.085 \pm 0.017}$ |
| JAM-Axi-D | $-0.176 \pm 0.2674$ | $46.50 \pm 3.90$ | $0.2559 \pm 0.0082$ | $10^{10.059 \pm 0.023}$ |
| JAM-Axi-E | $0.506 \pm 0.0033$ | $87.54 \pm 1.50$ | $0.8017 \pm 0.0014$ | $10^{9.262 \pm 0.019}$ |

The MGE expansion of the Hernquist model is given in Table 4.2. The surface brightness is calculated as $I_j = \frac{L_j}{2\pi\sigma_j^2 q_j'}$ as seen in eqn (3.15), where $L_j$ is the total luminosity of the enclosed Gaussian, $\sigma_j$ is the dispersion of the Gaussian along the major axis in arcseconds and $q_j$ is the dimensionless axial ratio of the major and minor axis.

### 4.4.3 JAM modelling results

Several simulations with different priors were run to investigate the effects of the different priors on the convergence of the method. The prior ranges of the different simulations are represented in Table 4.3. The error in the input data was simulated and used as an added diagnostic. The simulated rms error in the JAM-Axi-E prior range results is $\sim 1.80 \pm 0.13\%$ compared to the 5% input error.

Running a simulation with the full prior space (JAM-Axi-A) converges to a SMBH mass that is about an order of magnitude higher than the true value. In the case where the SMBH mass is not known *a priori* it would be unfeasible to evaluate the accuracy of the simulation in determining the SMBH mass. The log evidence value is used to choose between simulation results. The model with the highest value for log evidence is chosen when there are several simulations that yield slightly differing results.

JAM-Axi-B has a prior range of $M/L$ ratios that the JAM-Axi-A converges to. This limited range allows the other parameters to converge. The results are shown in Fig. 4.3. Because the desired parameter is the SMBH mass, any simulation where SMBH mass does not converge is not considered. A well constrained $M/L$ ratio results in a better constrained SMBH mass.

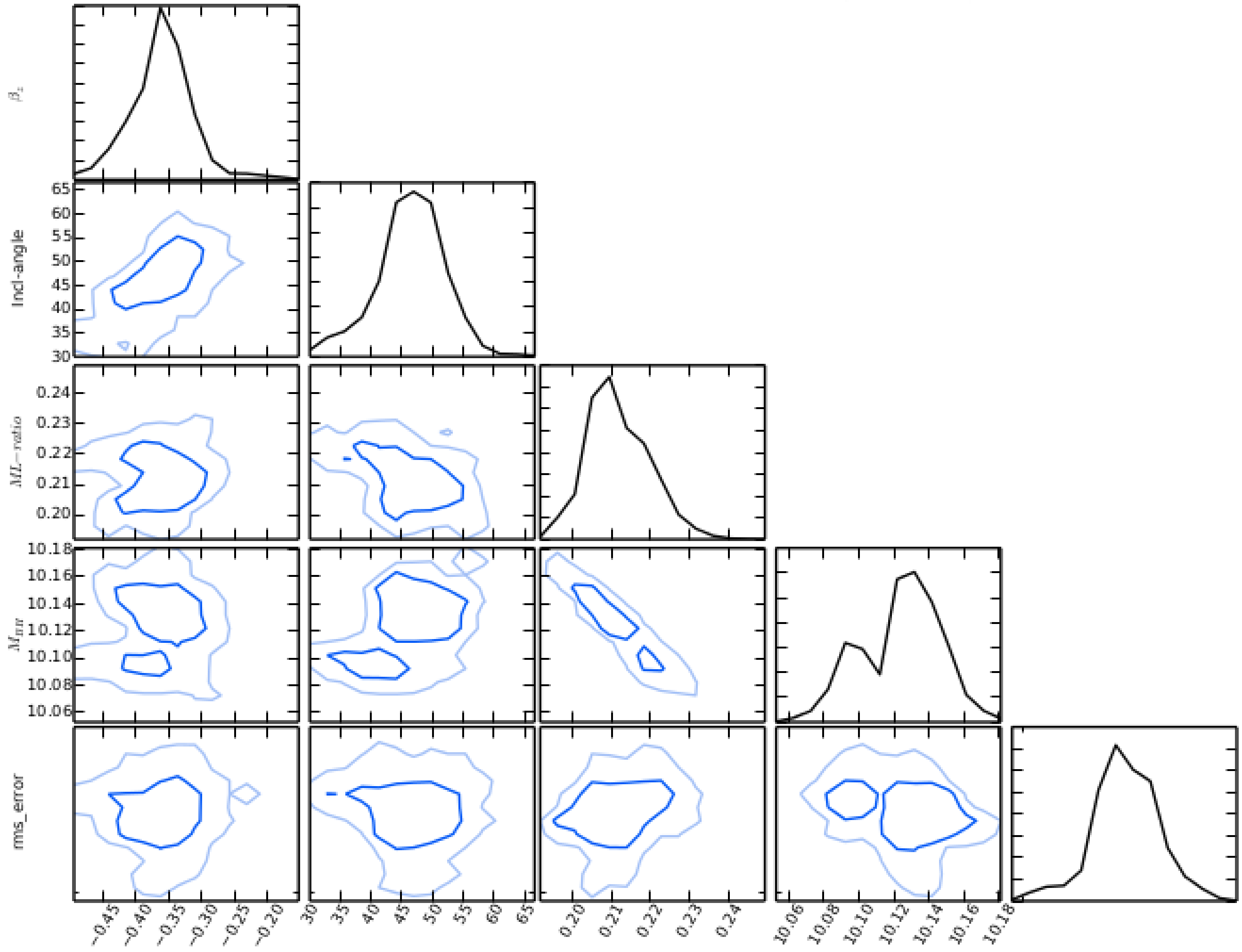

Figure 4.2: MultiNest results for axisymmetric JAM-Axi-A. The log evidence for the result is -2124. It shows a positive correlation between the inclination angle and the velocity anisotropy and a negative correlation between mass-to-light ratio and SMBH mass.

The effect of constraining the prior range of both the inclination and the velocity anisotropy is investigated next. Individually they cannot achieve the same effect as constraining the $M/L$ ratio. A simulation with the prior range $-0.1 \leq \beta_z \leq 0.1$ is run next and the results are shown in Fig. 4.4.

Fig. 4.3 shows the results of a simulation with the prior range $40° \leq$ inclination angle $\leq 55°$. The results show minimal improvement in the SMBH mass constrained as well as the log evidence of

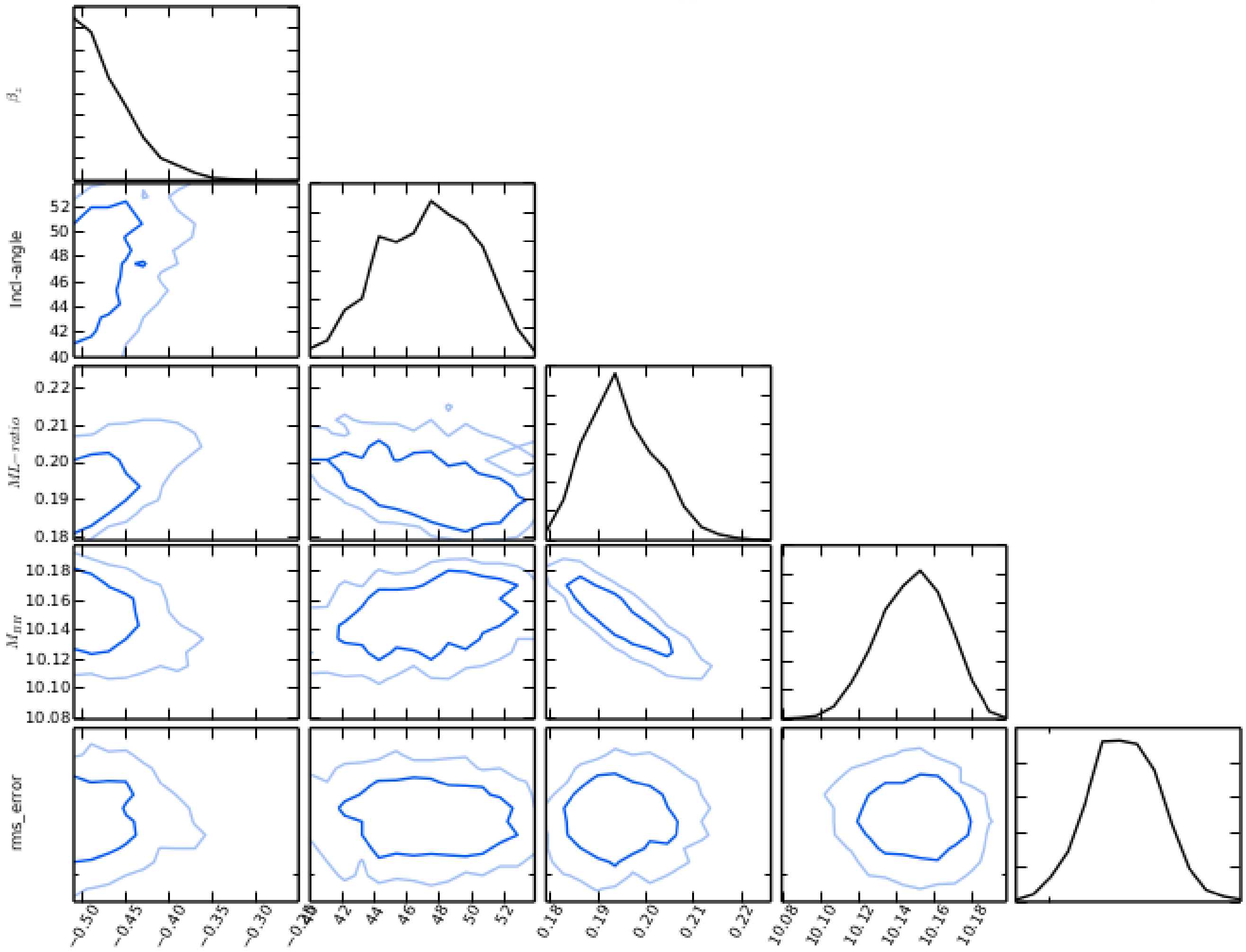

Figure 4.3: MultiNest results for axisymmetric JAM modelling with the prior range JAM-Axi-B. The log evidence for the result is -2118.

the simulation (-2118 instead of -2124). This suggests that, similar to the case of JAM-Axi-C, whose log evidence is -2129, the effect of $\beta_z$ and the inclination angle on the SMBH mass is not very great due to the weak correlation between SMBH mass and those other two parameters.

When they are both constrained together in JAM-axi-D the results, shown in Fig. 4.5, show little change from the initial results of JAM-Axi-A. The only additional aspect that is introduced in this simulation is an apparent bimodality in the results. This suggests that the two parameters $\beta_z$ and inclination angle are not correlated.

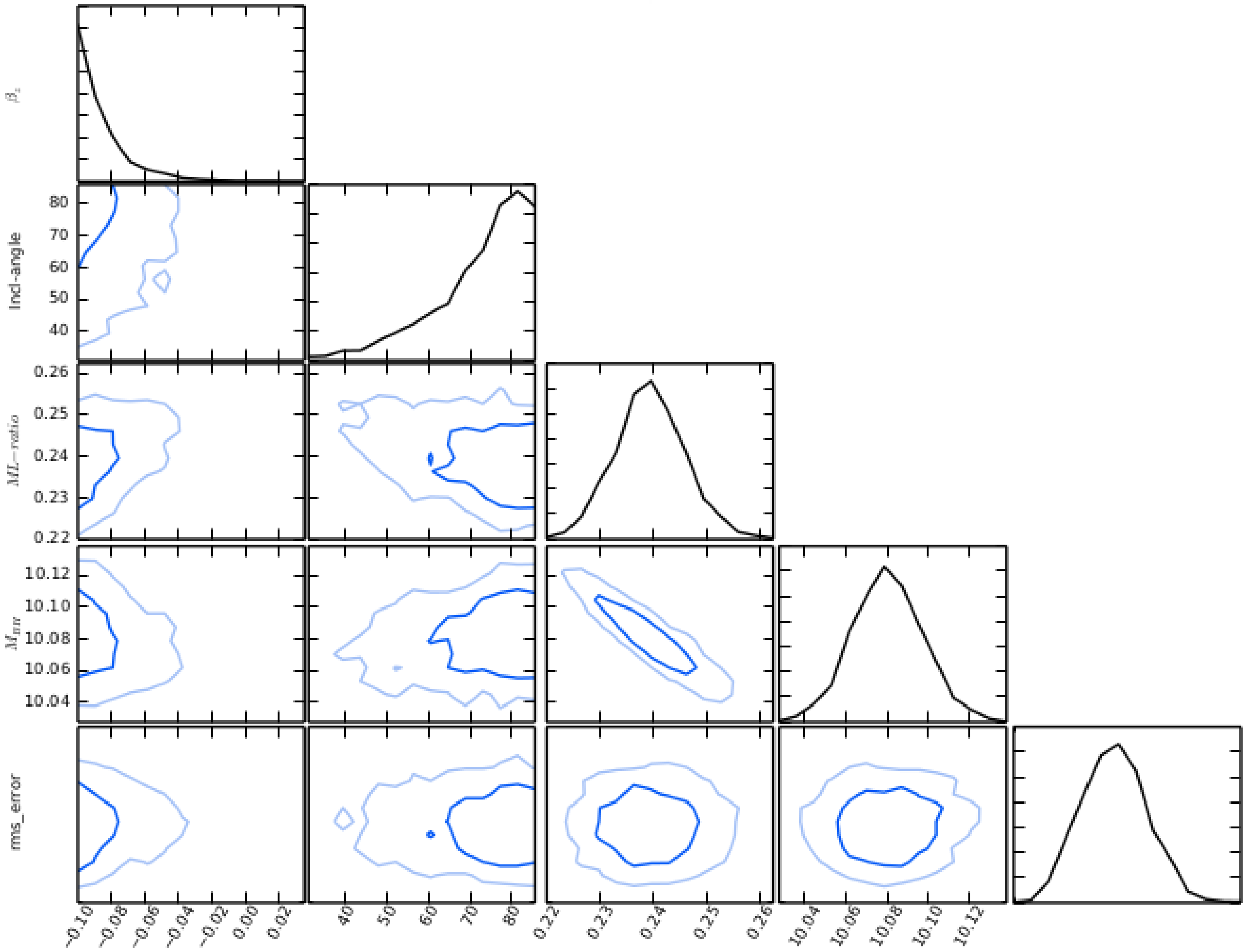

Figure 4.4: MultiNest results for axisymmetric JAM modelling with the prior range JAM-Axi-C. The log evidence for the result is -2129.

JAM-Axi-E has constrained the prior range of $M/L$ ratio to $1.0 \pm 0.2$ to investigate the effects of using a well constrained $M/L$ ratio on the SMBH mass measurement. The other priors are kept the same as JAM-Axi-A and the results are shown in Fig. 4.6. The log evidence value for the simulation (-2118) is very similar to the JAM-Axi-A and the SMBH mass is a vast improvement on the other simulations. The other priors do not converge to true values.

The results of the JAM axisymmetric model parameter estimation are shown below. The black-hole mass is constrained very well to a value of $\sim 10^{9.242}$ in the results. The other parameters show no convergence to a single value. The inclination angle shows the whole parameter range from 30° to 90° and the $M/L$ ratio converges to a value of $\approx 0.8$.

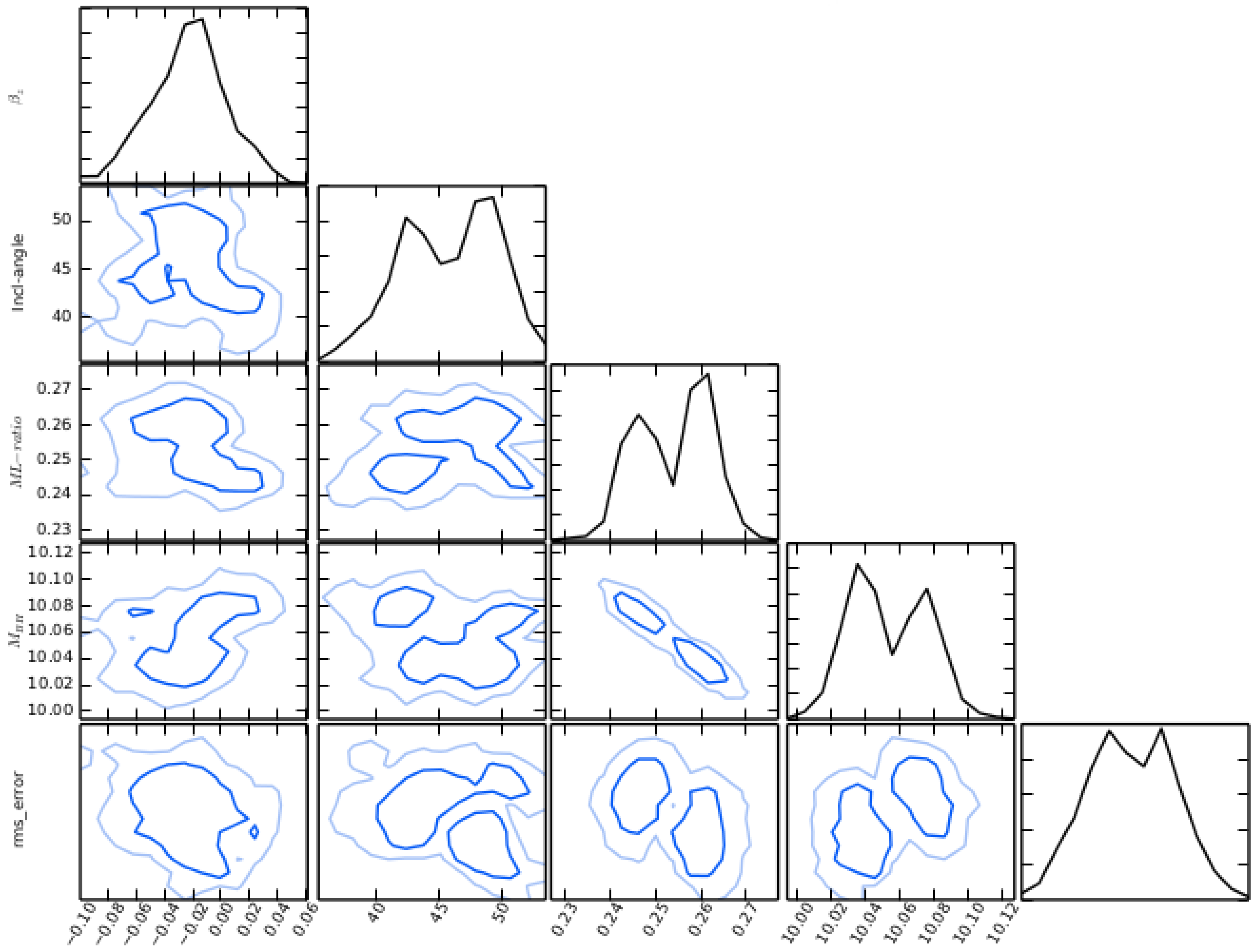

Figure 4.5: MultiNest results for axisymmetric JAM-Axi-D. The log evidence for the result is -2137.

The equally weighted posterior results of MultiNest give a better indication of how closely the results represented approximate the velocity distribution of the input model. Fig. 4.7 is a plot of the average velocity of all the models of the equally weighted posterior at every radial distance.

The mean model in Fig. 4.7 shows the $1\,\sigma$ error of the total results. The $1\,\sigma$ error is barely visible in the plot due to the possible solutions having little scatter. The velocities of the model and the solutions cross at around $15''$ and the solutions over-estimate the rms velocities at radii higher than $\approx 15$ whereas it under-estimates them at lower radii. This could be mitigated by fitting

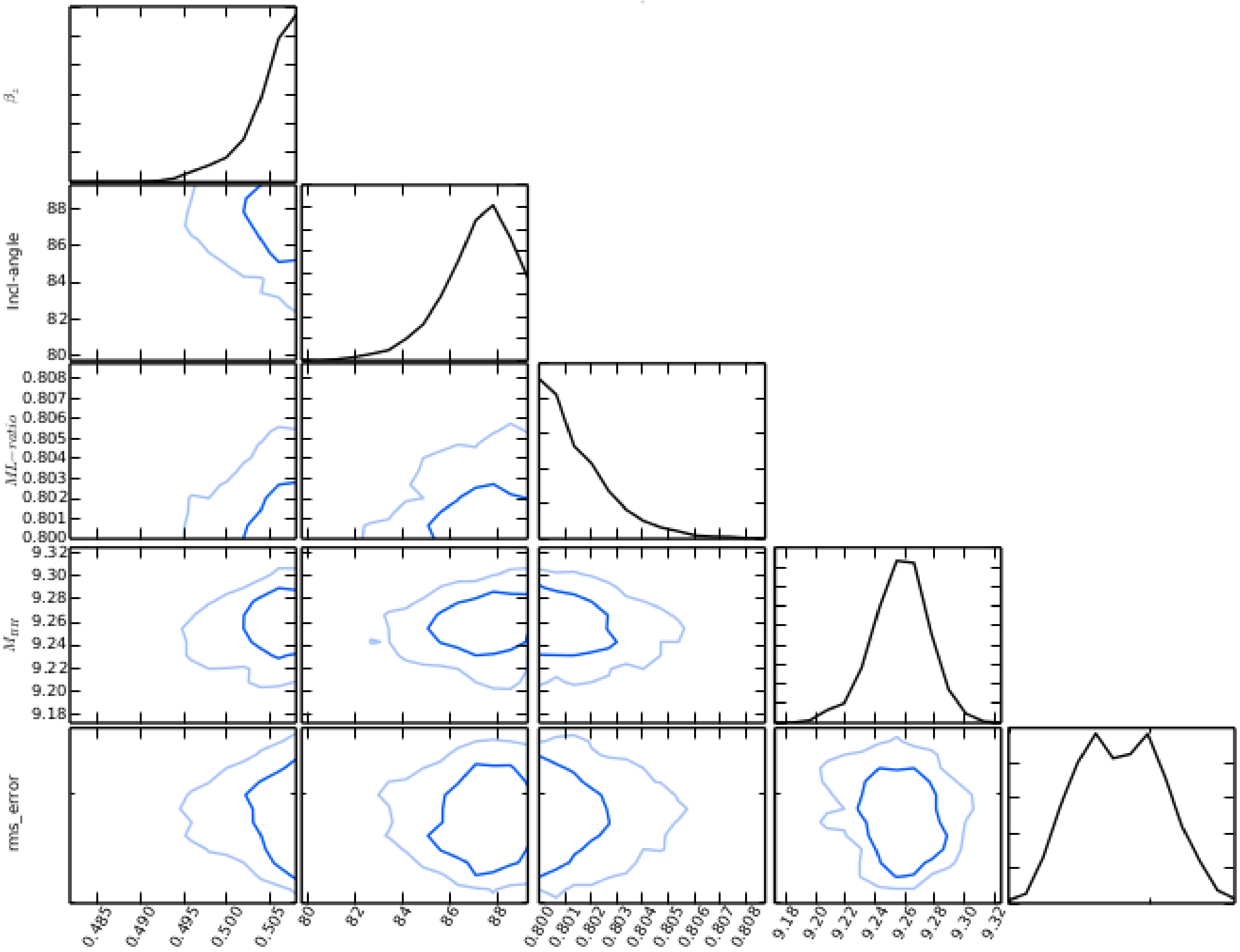

Figure 4.6: MultiNest results for axisymmetric JAM-Axi-E. The log evidence for the result is -2118.

only a limited radial distance closer to the core in the JAM model algorithm. This becomes the desirable strategy when there are other methods of constraining the global $M/L$ ratio. This would lead to a closer agreement between model and results towards the core due to fewer fitting points.

In practice, the limited field of view of high resolution IFU spectrographs limits the fitted area to within $5''$ of the core at best. This necessitates the alternative ways of constraining global $M/L$ ratio for better constraints on the stellar mass distribution within the galaxy. This usually takes the form of longslit spectroscopy or low resolution IFU spectra.

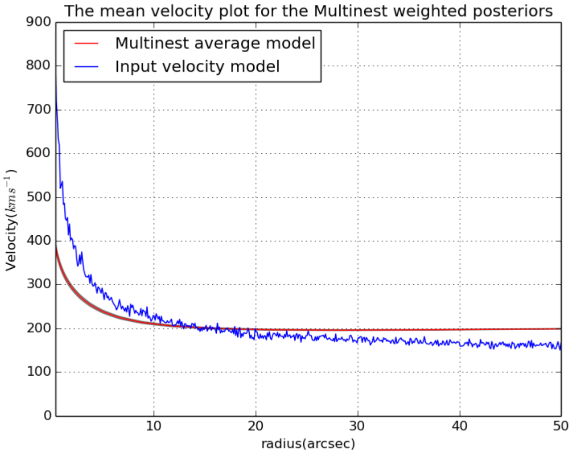

Figure 4.7: The blue graph shows the input model velocities as a function of radius and the red graph is the mean model of velocities from the equally weighted posteriors of the MultiNest simulation as a function of radius.

## 4.5 Discussion

A constant known problem in galaxy modelling is the mass-anisotropy-degeneracy. This is a degeneracy in stellar dynamical models that makes the measuring of the mass profiles of gas-poor galaxies difficult. This can be solved by constraining the mass distribution of the galaxy as part of the model. There are different mechanisms of achieving this and they involve using different mass tracers to constrain the mass interior to a radius using different observational methods, like HI rotation curves together with IFU data (Courteau et al., 2014). This helps constrain the $M/L$ ratio as a function of radius and the contribution of dark matter to the total galaxy mass. The contribution of dark matter to the galaxy mass at the effective radius $r_e$ can be between $10\% - 40\%$ in ETGs in the locaL Universe (e.g. Cappellari et al., 2013) and has been shown to almost double the modelled blackhole mass in the case of M87 (Gebhardt & Thomas, 2009), this makes the incorporation of the dark matter content in the modelling of the gravitational potential an important consideration.

The other technique is to use the strong gravitational lensing by galaxies to constrain the total mass of a galaxy. This is particularly useful for ETGs which generally do not have gas-dynamic tracers (Serra et al., 2012; Courteau et al., 2014). The use of IFU data without AO to study the 2D kinematics of the whole galaxy could also be useful, in conjunction with the core dynamics, in expanding the radius of the galaxy for which we can probe the galaxy dynamics.

Our results show that constraining the $M/L$ ratio is a much more effective way of improving the ability of the JAM models to measure SMBH mass. The other parameters have a marginal effect on the accuracy of the JAM models and they also have proved as difficult to constrain observationally as the $M/L$ ratio. This makes the search for observational methods of constraining $M/L$ ratio an important step in establishing it as a general and fairly accurate SMBH mass measurement technique.

The IFU data is very useful in providing the velocity stellar kinematics within a limited region of the core of the galaxy. This necessitates the caveat in JAM modelling that $M/L$ ratio is constant throughout the galaxy. In practice this is not necessarily true, as there have been studies showing that dark matter content in ETGs varies with radius (Treu & Koopmans, 2004; Poci et al., 2017). Dark matter dominated parts of a galaxy suffer from the difficulty of using stellar luminosity to infer mass. This method will be applied to a sample of galaxies that have already been analysed with other SMBH mass measurement methods to benchmark the results with the more accurate results from other methods and the use of other $M/L$ ratio observational constants. The technique discussed in this chapter is applied to the ETG NGC 6861 in the following chapter.

# Chapter 5

# Blackhole mass measurement of NGC 6861

## 5.1 Introduction

Accurate measurement of SMBH masses is crucial to the understanding of AGN radio jet formation and, potentially, jet composition. Jet composition is one of the open questions in AGN and BTRS studies. JAM dynamical models are capable of reproducing the values of SMBH masses that have good agreement with those determined by the Schwarzschild models (Krajnović et al., 2009; Cappellari et al., 2010). JAM models also provide a more physical insight into the dynamics of the galaxy and that makes them useful to perform even with the availability of the more state-of-the-art methods such as the Schwarzschild orbit superposition method and the made-to-measure methods.

In this chapter the JAM method is used with Bayesian parameter estimation, as discussed in the last chapter, on the S0 galaxy NGC 6861 from the SALT sample, to test how well it compares to results obtained using other methods of blackhole mass measurement. NGC 6861 is the second brightest galaxy in the Telescopium (AS0851) group which lies at a distance of 28 Mpc. NGC 6861 has shown signs of interaction with the brightest galaxy in its group, namely NGC 6868 (Machacek et al., 2010). It also has the peculiar characteristic of having a higher stellar velocity dispersion ($\sigma = 414$ km s$^{-1}$) than its more massive counterpart NGC 6868 ($\sigma = 254$ km s$^{-1}$). This gives it a predicted SMBH mass that is about an order of magnitude higher based on $\sigma$ compared to the mass based on galaxy mass.

Its distance and Southerly position in the sky make it resolvable with the VLT telescope. The line-of-sight velocity distribution (LOSVD) is calculated with the PPXF analysis tool and used in the JAM models with a MultiNest Bayesian engine to make the SMBH mass determinations. The JAM method of SMBH mass modelling uses the surface brightness distribution from the photometry of a galaxy and its $M/L$ ratio to work out the distribution of mass throughout the galaxy and it incorporates the spectroscopic data to calculate the velocity distribution of stars in the core of the galaxy, including in the SMBH's sphere of influence, to evaluate how much of the mass contained within that region is due to the SMBH. So the photometric and spectroscopic data are complementary in the process of SMBH mass measurement.

## 5.2 Observations and data reduction

The archival NIR spectroscopy observations of the NGC 6861 galaxy were done using the SINFONI IFU instrument of the VLT telescope in Chile. The data has a spatial scale of $0\farcs25$ which corresponds to a spatial resolution of about 33 pc at the NGC 6861 distance of 27.3 Mpc as listed in the HyperLeda database. The archival photometric data were observed with the HST-WFPC2 using the F814W and the F555W filters.

The HST-WFPC2 is an imaging photometer, mounted at the focal plane of the HST, with a spectral range coverage between 1150Å and 10500Å. It has an L-shaped wide field camera region of $150'' \times 150''$ with a spatial resolution of $0\farcs1$ per pixel that is attached to a $34'' \times 34''$ square planetary camera field with $0\farcs046$ resolution per pixel. Fig. 5.1 shows the layout of the planetary camera (PC) region in relation to the wide field camera region covered by the WF2, WF3 and WF4 portions of the CCD.

The HST-WFPC2 contains 48 filters that include a set of filters which approximate the Johnson-Cousins UBVRI filters. The photometric data were observed with the F555W and the F814W filters which are similar to the Johnsons-Cousins V and I filters respectively.

### 5.2.1 VLT SINFONI Observations

The IFU spectroscopy was observed in the K-band during the first semester of 2011 from 2011-04-14 to 2011-08-08. The galaxy NGC 6861 was observed in six observation blocks with each containing (Object-Sky-Object-Object-Sky-Object-Object-Sky) sequence and a telluric standard

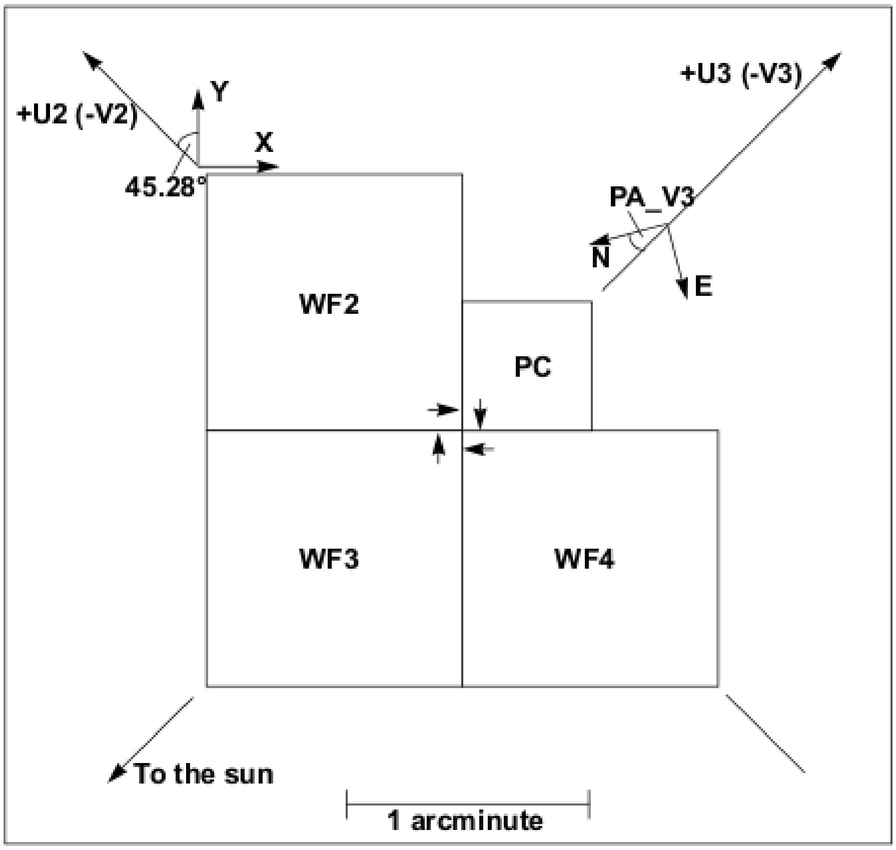

Figure 5.1: The schematic of the layout of the CCDs of the HST-WFPC2 showing the planetary camera (PC) and the Wide Field regions of the CCD. Figure taken from McMaster & et al. (2008)

star for each observation block.

Each of the spectra was taken with an integration time of 300 s. This is due to the instability of the luminosity of the sky in the NIR wavelength range. The upper layers of the atmosphere change temperature at timescales of just less than 600 s, and for the data reduction to work the integration time of the observations should be less than ten minutes.

### Data reduction

All the data reduction was done using the ESOREX command-line tool (ESO CPL Development Team, 2015). The SINFONI data reduction cascade is made up of the following steps – each with its own recipe

- **sinfo-rec-detlin**: this estimates when the detector becomes non-linear and writes the results in the form of a map of non-linear pixels stored in the file with the tag **BP-MAP-NL**. Input are 20 flat-field images with increasing intensity. These images are taken once per month and are part of the SINFONI science calibration plan.
- **sinfo-rec-mdark**: this collects three dark frames that are observed daily for each exposure time and uses them to create a master dark frame **(MASTER-DARK)** and a bad pixels map **(BP-MAP-HP)**.
- **sinfo-rec-mflat**: this collects all observed flat fields and creates a master flat field image **(MASTER-FLAT-LAMP)** and a master bad pixel frame **(MASTER-BP-MAP)**. The input data set consists of ten on/off lamp flat fields, taken each day, together with the output from sinfo rec detlin **BP-MAP-NL**, the output from **sinfo-rec-mdark BP-MAP-HP** and some other static calibration files.
- **sinfo-rec-distortion**: this calculates the coefficients that result from optical distortions (**DISTORTION**) of the image slicer and the distance between the slitlets (**SLITLETS-DISTANCE**). Input for this recipe are 70 images of a calibration fiber. These calibration frames are also acquired once per month.
- **sinfo-rec-wavecal**: this uses the arc lamp, distortion map, the master flat frame and the master bad pixel frame to create a wavelength map image where intensity corresponds to wavelength. The output files, which are used in the next step, contain the wavelength map (**WAVE-MAP**) and the position of each slitlet on the detector (**SLIT-POS**).
- **sinfo-rec-jitter** for PSF: this creates the data cube of the observation of the PSF standard star. This is used for calculating the point spread function of the telescope setup and calculation of the Strehl ratio.
- **sinfo-rec-jitter** for science data: this creates the data cube for the science object and does sky background reduction.

The accuracy of the wavelength calibration was compared to the positions of OH emission lines in the K-band as taken from the (Rousselot et al., 2000) atlas. Small shifts of about half a pixel were applied to the NGC 6861 IFU data.

**Telluric correction**

The transmission of electromagnetic radiation in the NIR depends heavily on the amount of hydroxyl (OH) molecules in the atmosphere as well as it's temperature and humidity. These are not stable conditions in the atmosphere at night. The atmosphere changes in a matter of minutes in the NIR part of the spectrum and as a result the telluric emission line removal is a crucial last step in NIR data reduction.

The telluric lines of the K-band are removed using the standard method as stipulated in Vacca et al. (2003), where each of the galaxy observations is taken alongside observations of a telluric standard star. Telluric standard stars are B-type stars that are either totally featureless or have only the Br $\gamma$ ($2.166\,\mu$m) absorption line in the K-band, due to the atmospheres of the stars. Because of their high temperatures, these stars are well approximated by the Rayleigh-Jeans portion of the blackbody spectrum in the K-band. When a telluric star has the Br $\gamma$ absorption line, it is removed by modelling it in the IRAF task **splot** using a Lorentzian line profile and subtracted from the continuum of the star's spectrum.

The star is then divided by a blackbody spectrum of the same temperature as the star using the esorex task **sinfo-util-spectrum-divide-by-blackbody**. This gives a normalized telluric spectrum. The dispersion direction of the telluric spectrum corresponding to each data cube was then shifted to minimise the residuals of the telluric lines.

### 5.2.2 HST photometric observations

This section is based on observations made with the HST, and obtained from the Hubble legacy archive (HLA), which is a collaboration between the space telescope Science institute (STScI/NASA), the space telescope European coordinating facility (ST-ECF/ESA) and the Canadian astronomy data centre (CADC/NRC/CSA).

The observations were made on the 1997-04-26 and the archival data was automatically reduced with the HLA pipeline. From the two HST high resolution images the dust lane of NGC 6861 is evident. The data reduction was completed using HLA's automatic data reduction pipeline. The point spread function (PSF) of the HST was calculated using TinyTim (Krist et al., 2011). The charge transfer efficiency (CTE), which is relevant for only point sources in low backgrounds, was not corrected for.

The HLA's automatic data pipeline performs data reduction steps to HST data that allow for use in a wide variety of astronomical applications. The output data had the following data reduction steps performed: mask dark correction, bias correction, flat fielding, sky subtraction and cosmic ray removal.

The details of the data reduction tasks performed by the HLA automatic pipeline, OPUS, are discussed in the WFPC2 Data Handbook. Here the steps performed are mentioned in the context of the general optical photometry data reduction. Flat fielding corrects for the varying sensitivity of the CCD pixels. Dark correction mitigates the thermal effects that are due to the CCD's interface of the oxide and silicon layers, and bias correction deals with the number of counts that an unexposed pixel in a CCD has. These may vary from pixel to pixel but all pixels experience the same effect.

Sky subtraction is carried out by MultiDrizzle, a routine that also combines the dithered HST images and removes both geometric distortion and cosmic rays, in the OPUS software. Cosmic rays typically affect seven pixels per event in the HST-WFPC2 and have a very low probability of occurring at the same spot in a CCD within the time it takes for an exposure. So taking several exposures of the same pointing allows for removal of the spurious cosmic rays from the CCD image. The recommended number of pointings is 2-4 per image, and OPUS will automatically remove them and provide an image of similar quality to Fig. 5.2. Some of the point sources were removed from the field and the MGE analysis, discussed in Section 5.3.2, was done on the cleaned image. The point sources that were not removed were those that did not affect the isophotes of MGE much. These point sources in general were less than $5\,\sigma$ brighter than their surroundings and tended to be on the edges of the galaxy.

## 5.3 Data analysis and results

The method of using stellar kinematics to measure SMBH mass uses the surface brightness of the galaxy and the velocity dispersion measurements to calculate the mass distribution in the galaxy. JAM modelling matches that mass distribution to the two-dimensional velocity dispersion measurements in the galaxy, particularly close to the galaxy core. Within the SMBH SOI

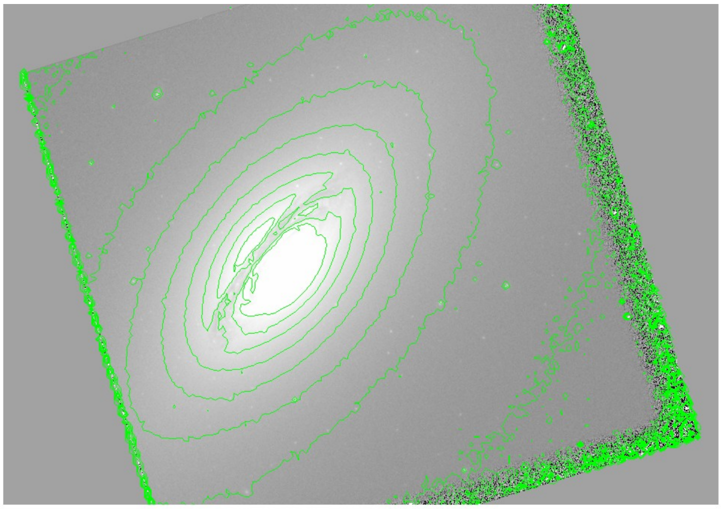

Figure 5.2: The raw HST Photometric image of NGC 6861 in the filter F814W.

the velocity dispersion increases due to SMBH mass. These measurements are put into the Jeans equation (eqn 4.21) and the optimal SMBH mass, $M/L$ ratio, velocity anisotropy and inclination angle are determined via an MCMC method using Bayesian statistics.

### Voronoi binning

Voronoi binning (Cappellari & Copin, 2003) is an adaptive binning method, aimed at preserving maximum spatial resolution for 2-D data given a constraint on the required minimum S/N ratio. It is based on Voronoi tesselation with nearly hexagonal lattices. Voronoi tesselation works by subdividing a region of the 2-D image based on the following 3 criteria,

- Topological criterion, where all the spaxels are used once and never repeated.
- Morphological criterion, where the bins should be as round or hexagonal as possible.
- Uniformity criterion, where the scatter in the S/N of the bins is minimised, such that the spatial resolution is not severely compromised.

This leads to the high S/N spaxels around the core of the galaxy being a one spaxel bins and then the further bins from the core having progressively more spaxels.

The S/N of 40 for each bin was chosen for Voronoi binning of IFU spaxels. The combined spectrum of each bin was fitted with the best combination of the template stars using the optimal systemic velocity and velocity dispersion. The results of the velocity dispersion analysis in Fig5.5 are based on this Voronoi binning.

### 5.3.1 Velocity dispersion analysis

The PPXF is a method of fitting one or more template spectra convolved with the LOSVD to the spectrum of a galaxy in logarithmically-binned wavelength or pixel space Cappellari & Emsellem (2004). PPXF allows for biasing towards a Gaussian distribution for both the velocity $\mathbf{V}$ and the velocity dispersion $\sigma$ by using Gauss-Hermite moments $h_3$ and $h_4$. The penalization factor $\lambda = 0.5$ achieves a satisfactory result (Cappellari & Emsellem, 2004).

PPXF relies on the availability of good template spectra for its success and the seven spectra discussed above work very well in modelling ETGs in the K-band. In the final analysis, four of these template spectra, viz. HD 0025211, BD-161418, 2MASSJ20411845+0016280 and 2MASSJ17093801-2718559 were needed to model the collapsed nuclear spectrum of the NGC 6861 data cube.

Table 5.1: The list of velocity template stars used in the PPXF analysis for NGC 6861.

| Star name | Spectral type |
|---|---|
| HD 0005425 | K4III |
| HD 0025211 | K4/5III |
| BD-151319 | K5III |
| BD-161418 | K7III |
| 2MASSJ20411845+0016280 | M0III |
| HD 0141665 | M5III |
| 2MASSJ17093801-2718559 | M5II-III |

The list of template stars in Table 5.1, supplied by M. Lyubenova (private communication), is used due to their proven usefulness in simulating spectra of ETGs in the NIR. The K-band spectra of these template stars are shown in Fig. 5.3. They are dominated by low mass giant stars, which are the population most likely to dominate the luminosity of ETGs. These template stars were also observed using the SINFONI instrument with the same setup as the NGC 6861

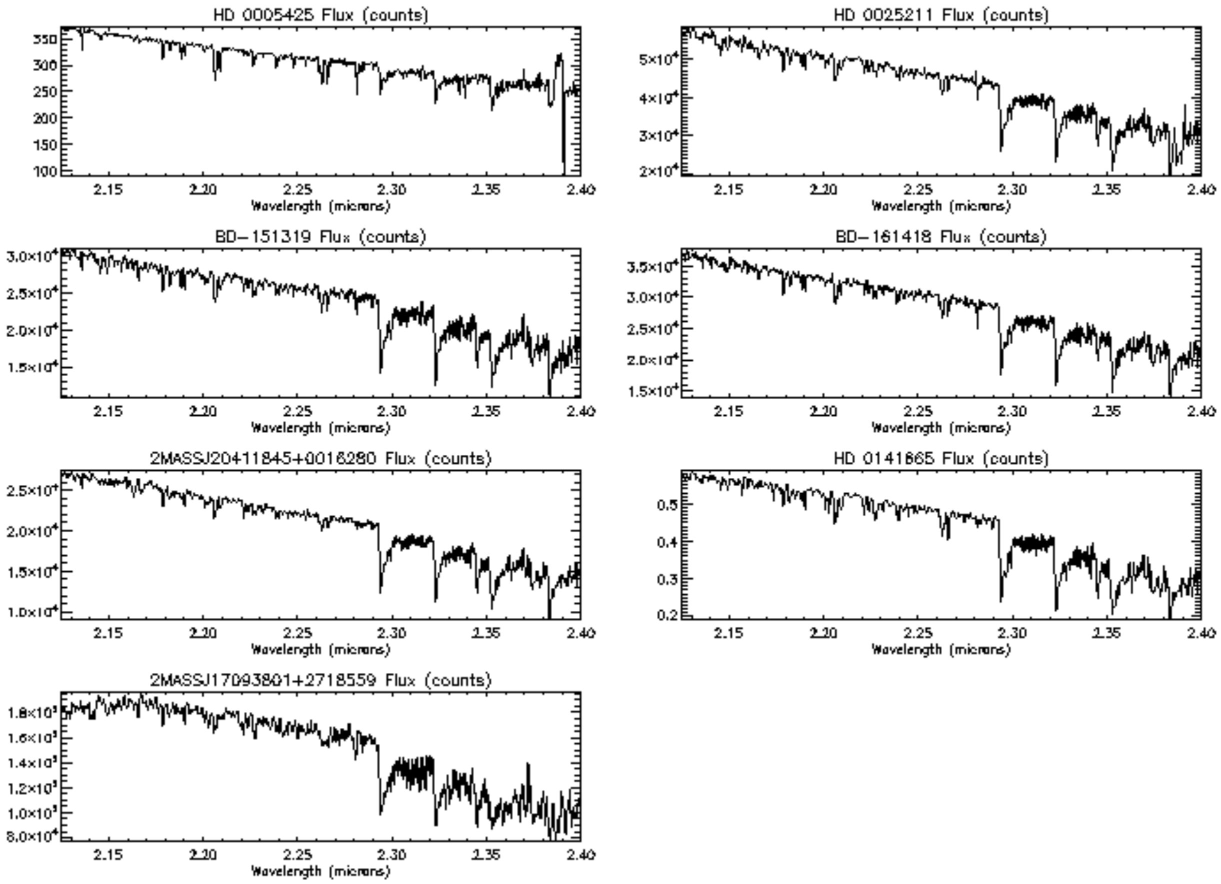

Figure 5.3: The K-band spectra of PPXF K and M giant template stars listed in table 5.1.

observations.

The ppxf fitting was performed in the spectral range between 2.2 $\mu$m and 2.4 $\mu$m, where several features, including the CO Band head, are prominent enough to allow PPXF fitting. The Na I feature at $2.2 - 2.22\,\mu$m is included because NGC 6861 is an ETG and the feature has been found to correlate well with velocity dispersion (Silva et al., 2008). The stellar photospheric CO absorption band head at 2.3 $\mu$m is intrinsically sharp and thus offers an excellent feature for probing stellar kinematics and it is more common in stars than the Br $\gamma$ absorption line.

The results of this fit are shown in Fig. 5.4. The bestfit results are combined into a single template star according the weighting listed in the result. This composite bestfit template is used to fit each of the Voronoi binned sections of the data cube. This provides a common template with which all the Voronoi bins were penalized for the sake of consistency.

The total PPXF results of the Voronoi binned cube are shown in Fig. 5.5. The results plotted in **Vsyst** show the first velocity moment with the systemic velocity removed. It is thus reduced to 2-D rotation of the galaxy. The results plotted in **Sigma** show the velocity dispersion of the galaxy core. The $\mathbf{h}_3$ & $\mathbf{h}_4$ results are for the corresponding Gauss-Hermite moments.

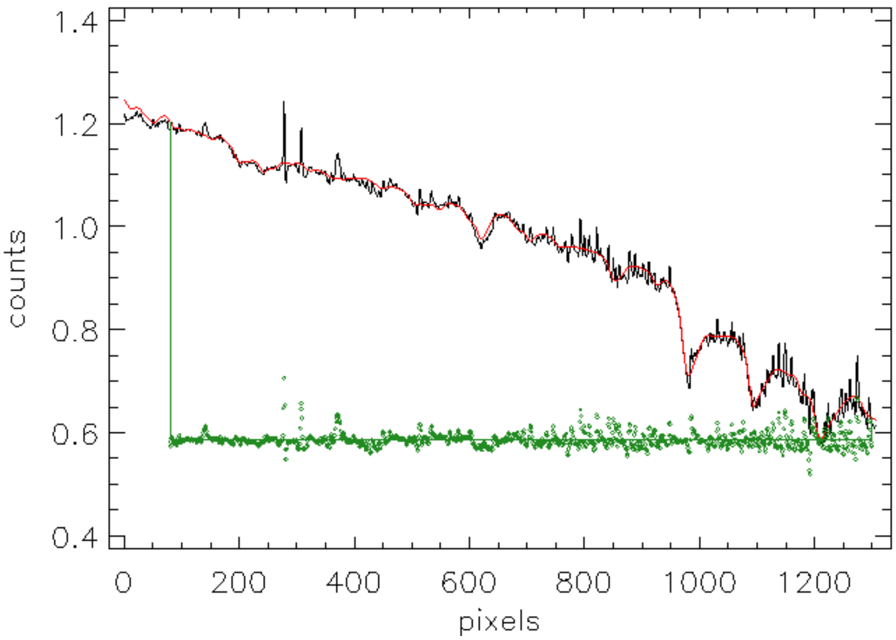

Figure 5.4: The besfit template for the collapsed SINFONI spectrum of NGC 6861. The red spectrum represents the bestfit composite spectrum of the template stars and the black spectrum is the collapsed SINFONI spectrum.

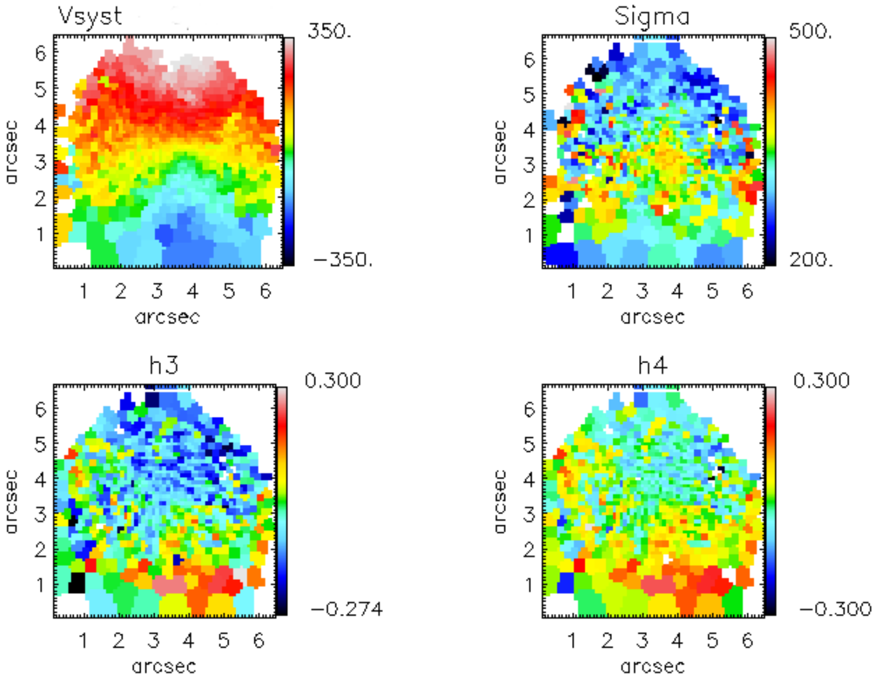

Figure 5.5: The PPXF results on the NGC 6961 SINFONI data derived from the CO band-head spectroscopy. Maps of systemic velocity (Vsyst), velocity dispersion (Sigma), and the Gaus-Hermite moments $h_3$ and $h_4$
are shown above.

### 5.3.2 Mass modelling with MGE

The S0 galaxy NGC 6861 has an inner disc that almost extends to the nuclear 1″ radius. This makes it difficult to do an MGE analysis on it as the colour of the bulge is non-uniform. To mitigate this problem the use of the pixels in the dust lane of the inner disk are suppressed in the MGE calculation. Fig. 5.6 shows a comparison of the isophotes, in black, that enclose the regions of equal surface brightness, and in red, the Gaussian model of the isophotes as modelled by MGE for the nuclear region of NGC 6861. This leads to a scenario where the anisotropy of the isophotes is determined by the radii of the galaxy beyond the dust lane.

Fig. 5.7 shows the comparison of the surface brightness of the full HST image of NGC 6861 in the WFPC2/F814 filter with the MGE model. The results of the MGE analysis are shown in Table 5.2. The first column shows the peak surface density within the isophote and the second column shows the dispersion along the major axis. The third column is the observed axial ratio of the Gaussian surface brightness model. These results form the photometric input into JAM modelling.

Table 5.2: Results of the Multi-Gaussian Expansion method of photometry of HST data for the nuclear region of NGC 6861.

| Surface density | Sigma pixels | qObs |
|---|---|---|
| 2.95636 | 0.380000 | 0.603830 |
| 13.5099 | 1.91448 | 0.825509 |
| 9.09019 | 2.27404 | 0.382152 |
| 66.9884 | 4.73356 | 0.568389 |
| 215.803 | 9.59135 | 0.567404 |
| 740.568 | 19.9916 | 0.570845 |
| 3038.01 | 47.9618 | 0.552701 |
| 24404.3 | 162.210 | 0.572987 |

Fig. 5.8 shows the goodness of fit between the MGE models and the image of NGC 6861 as a function of radius. The parameters of the Gaussians, represented by the solid lines in the left panel, are listed in Table 5.2. The right hand panel shows the errors in the goodness of fit of the Gaussians as a function of radius. The errors in the inner Gaussians are small and they increase in the outer Gaussians where imperfect flatfielding of the PC1 CCD near the borders, as shown

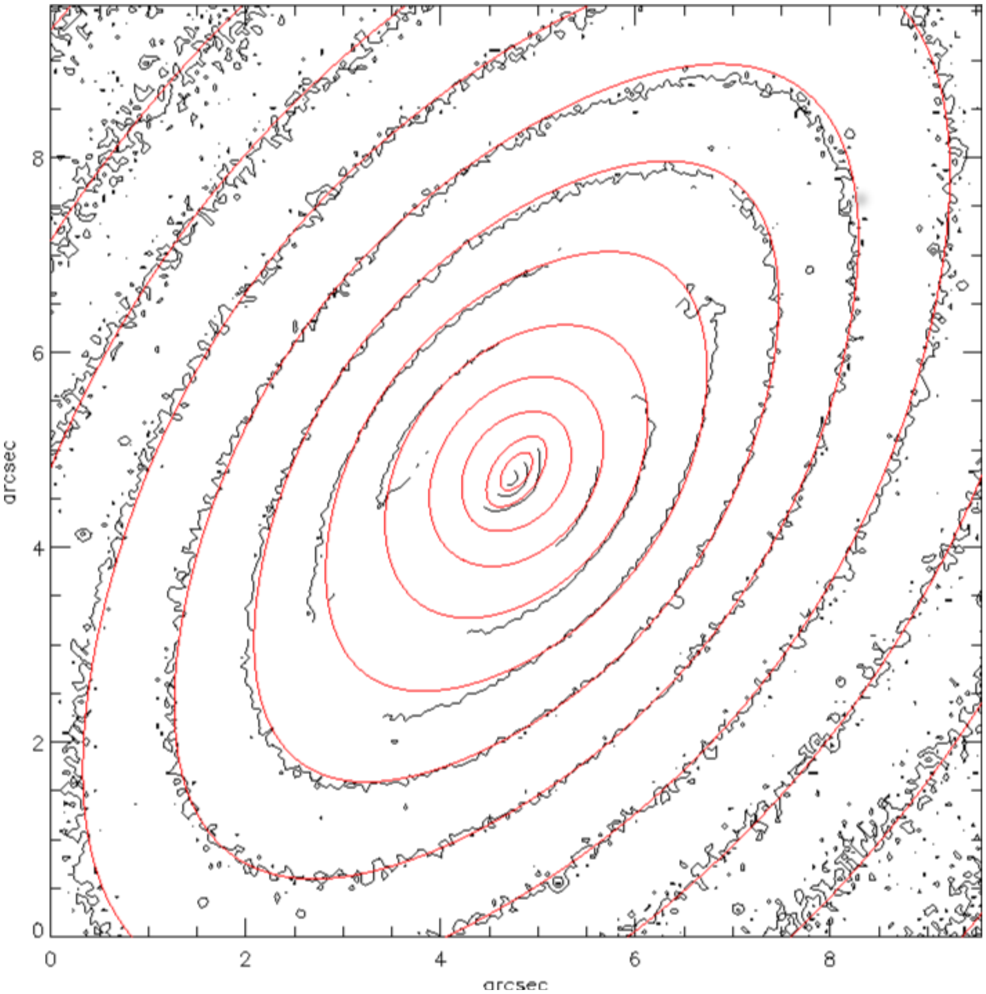

Figure 5.6: The nuclear MGE contours of the photometry of the WFPC2/F814 of the NGC 6861 galaxy for the nuclear surface brightness ellipsoids.

in Fig. 5.7, contributes to the errors.

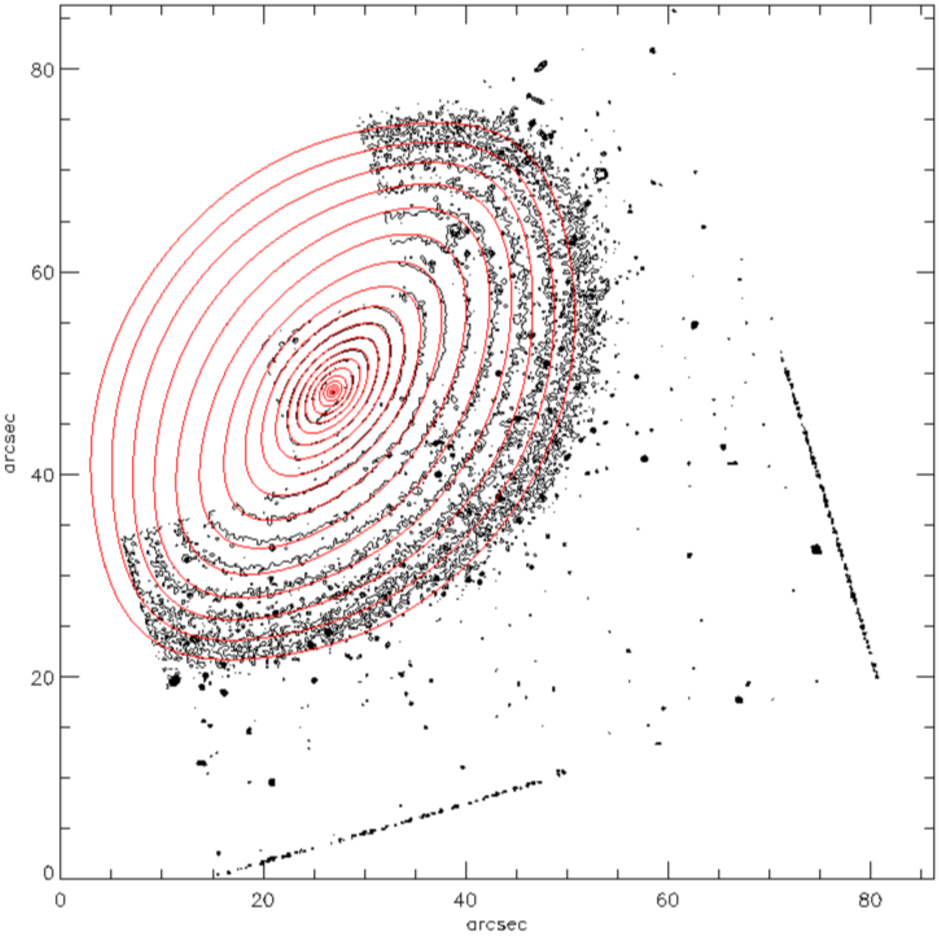

Figure 5.7: The MGE contours of the HST image of NGC 6861 for the total galaxy surface brightness. Imperfect flatfielding of the PC1 CCD near the borders contributes to the high errors at large radii.

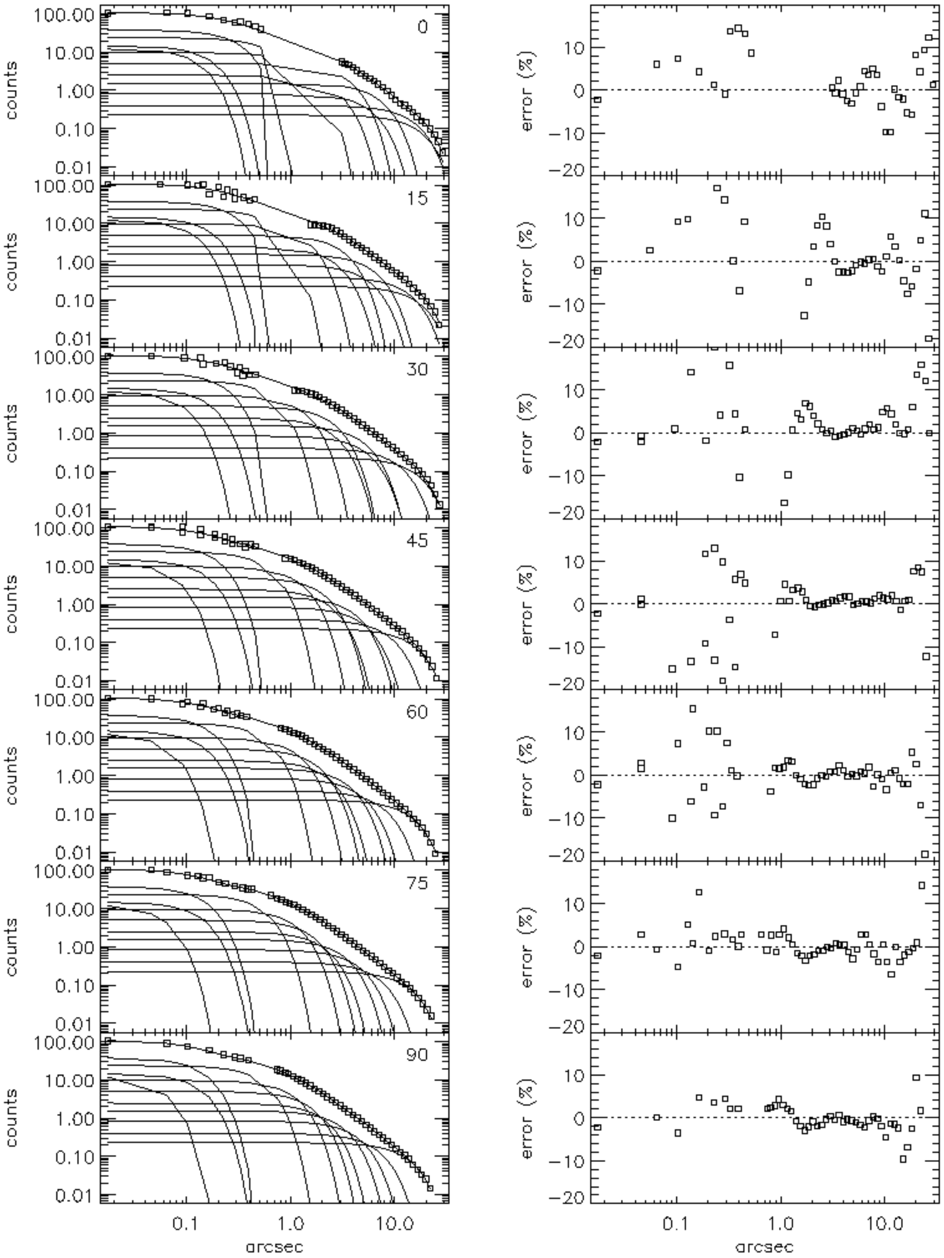

Figure 5.8: The MGE fitting of the WFPC2/F814 photometry of the NGC 6861 galaxy. Left panels show a comparison between the HST photometry (open squares with a line running through) and the convolved Gaussians composing the MGE model of NGC 6861 (solid lines), as a function of radius. Right panels show the relative errors of the MGE model compared to the data, as a function of radius. Different panels show different angular sectors.

### 5.3.3 JAM modelling and results

The JAM modelling is performed using the Bayesian code discussed in the Section 4.3 of the previous chapter. To solve for the four variables (SMBH mass, inclination angle, velocity anisotropy denoted by $\beta_z$ and $M/L$ ratio) constrained in JAM modelling, the prior ranges vary as stipulated in Table 5.3. The input surface brightness profile is the MGE result found in Table 5.2.

Table 5.3: Prior space for NGC 6861 models.

| Model name | $\beta_z$ | Inclination angle | $M/L$ ratio ($\upsilon$) | SMBH mass |
|---|---|---|---|---|
| Prior-A | $[-1.00 : 1.00$ | $[73 : 90]$ | $[0.0 : 10]$ | $[10^6 : 10^{10.5}]$ |
| Prior-B | $[-0.50 : 0.00]$ | $[73 : 90]$ | $[5.5 : 6.5]$ | $[10^6 : 10^{10.5}]$ |
| Prior-C | $[0.00 : 0.50]$ | $[73 : 90]$ | $[5.5 : 6.5]$ | $[10^6 : 10^{10.5}]$ |

The results, for a broad prior space as shown in Prior-A, do not effectively constrain a SMBH mass. This general prior is only constrained by the assumption that when the inclination angle is less than 30°, the second velocity moments in the JAM model cannot be accurately determined. This is further constrained by trial and error because, for observed axial ratio (qObs) results from NGC 6861 photometry, the JAM calculation breaks down for an inclination angle less than 73°. The $\beta_z$ is given the range $-1.0 \leq \beta_z \leq 1.0$, which has been found to be an anisotropy range where ETG velocities fall (Cappellari, 2008). The $M/L$ ratio range was chosen based on an interpretation of Jiang & Kochanek (2007) where they found the $M/L$ ratios of their sample of ETGs to be $7.2 \pm 0.5$. A range that goes higher than $M/L = 10$ is also perfectly acceptable. In all the priors, the SMBH mass range is $10^6 \leq M_\bullet \leq 10^{10.5}$ because that is the generally accepted range for SMBH masses. As discussed in the previous chapter, this method is not effective in constraining the $M/L$ ratio. The $M/L$ ratio range used by Rusli et al. (2013) for NGC 6861 is chosen instead.

The results of the model Prior-A are shown in Fig. 5.9, where the SMBH mass is unconstrained and the value for $M/L$ ratio is unrealistic. The value of the anisotropy parameter ($\beta_z$) falls outside of the accepted range of $[-0.5 \leq \beta_z \leq 0.5]$. The dark blue contour line denotes the $1\,\sigma$ confidence interval and the light blue contour line represents the $3\,\sigma$ confidence interval in all the triangle plots.

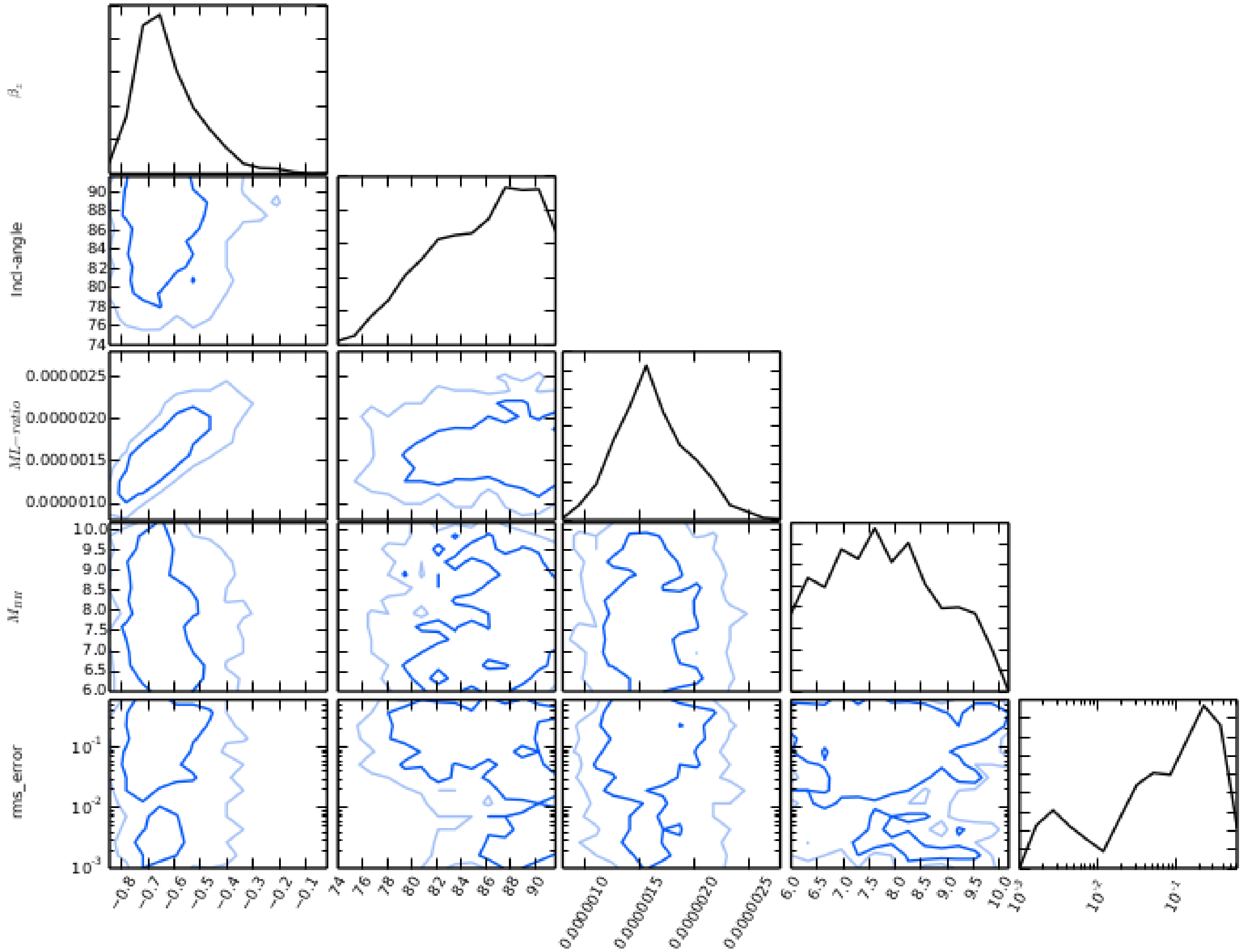

Figure 5.9: The results of model Prior-A. The triangle plot shows how the different priors are correlated. The $M/L$ ratio is positively correlated with the velocity anisotropy and the $M/L$ ratio is constrained to a lower number than feasible whereas the SMBH is not constrained at all.

The effect of limiting the velocity anisotropy parameter to a negative value is investigated as represented in Prior-B. The results are shown in Fig. 5.10 and it is evident from the plot for the results of $\beta_z$ that the parameter constrains to a positive value. The priors may be further constrained by using the range of inclination angles [73°:80°], which is justified by the measurement of the dust lane in the photometry of NGC 6861. Since a dust lane is supposed to be a disc, the calculation of $\cos i = b/a$, where $i$ is the inclination angle and the values of $b,\ a$ are the apparent major and minor axes respectively.

From these results the further constraint of a positive velocity anisotropy parameter is added, because NGC 6861 is a fast rotator (Cappellari, 2008). As discussed in the previous chapter, this method is not effective in constraining the $M/L$ ratio. The $M/L$ ratio range used by Rusli et al. (2013) for NGC 6861 ($5.5 < \Upsilon < 6.5$), is chosen and their results will be compared to the findings of this study. This leads to our model Prior-C which shows convergence shown in Fig. 5.11.

The results of constraining the priors to Prior-C give a SMBH mass $10^{9.47}$ $\mathrm{M}_{\odot}$ which agree very well with the results of (Rusli et al., 2013) for a model that excludes dark matter which give $2.2(2.1, 2.4) \times 10^{9}$ $\mathrm{M}_{\odot}$. The $M/L$ ratio that is constrained $5.50\frac{\mathrm{M}_{\odot}}{\mathrm{L}_{\odot}}$, instead of the value constrained by (Rusli et al., 2013) which is $5.9 \pm 0.2\frac{\mathrm{M}_{\odot}}{\mathrm{L}_{\odot}}$.

The apparent inclination angle of the galaxy NGC 6861 is about 73° based on the ratio of the lengths of the major and minor axes, which is $\sim 3.5$. The measurement is a rough one and even an 10% error would not affect the inferred inclination angle too much. Fig. 5.12 shows the dust lane from which the ratio of the minor and major axes is measured. The prior space for the inclination angle can, therefore, be limited to [73°:80°] to see how this affects the SMBH value constrained by the model. This should provide a more physically realistic result because the current value for the parameter almost constrains the galaxy inclination to completely edge-on.

The impact of a tighter constraint on the inclination angle is investigated above. This limited prior space for the inclination angle does not converge and cannot constrain the inclination angle values. This suggests a value that is in line with the results in Prior-C. The results, therefore, for a SMBH mass are the same as those discussed earlier for Prior-C and the inclination angle of 89°.

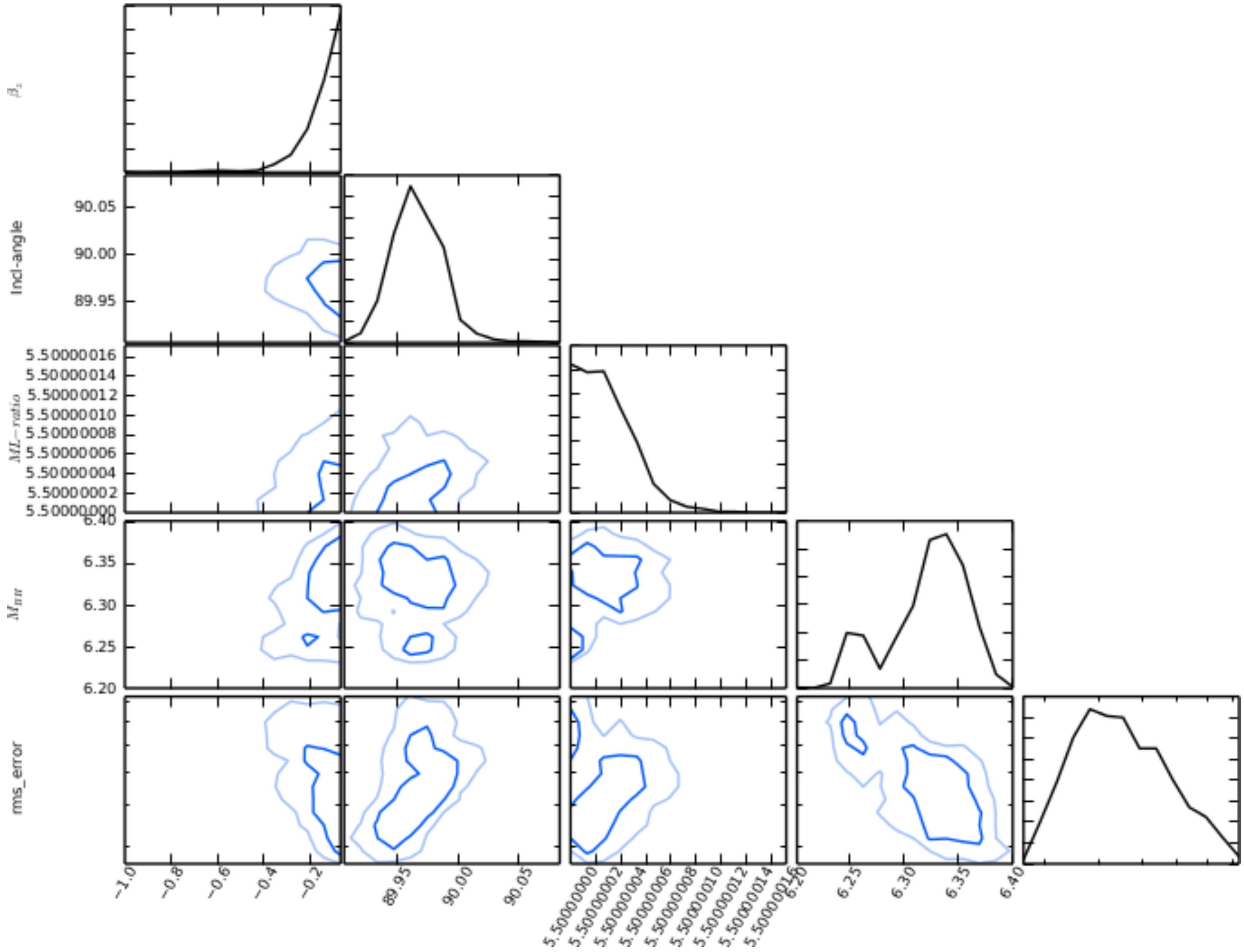

Figure 5.10: The results of model Prior-B. The $\beta_z$ value is unconstrained and leans towards a value $> 0$.

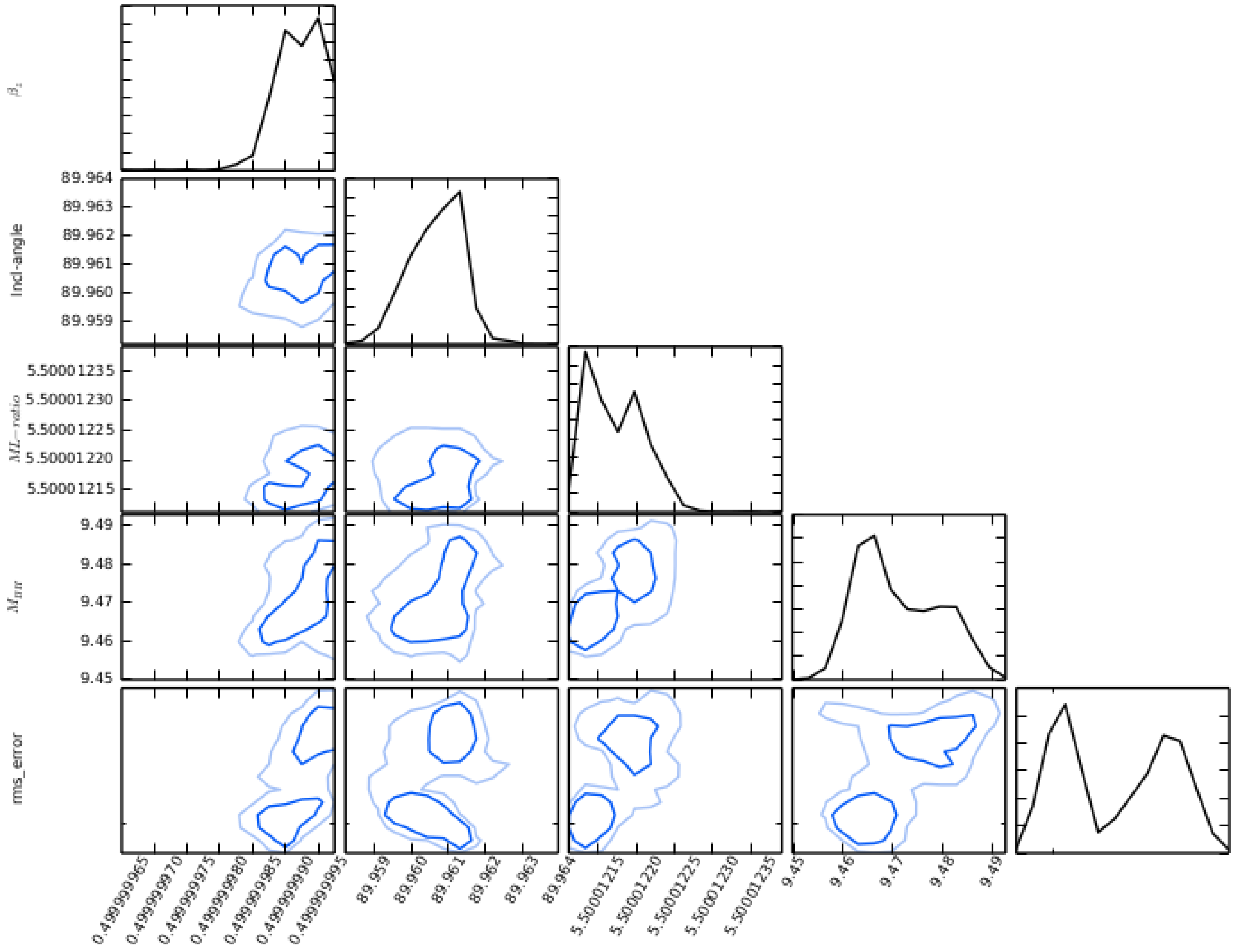

Figure 5.11: The results of model Prior-C. The triangle plot shows convergence of the model and the values of the parameters.

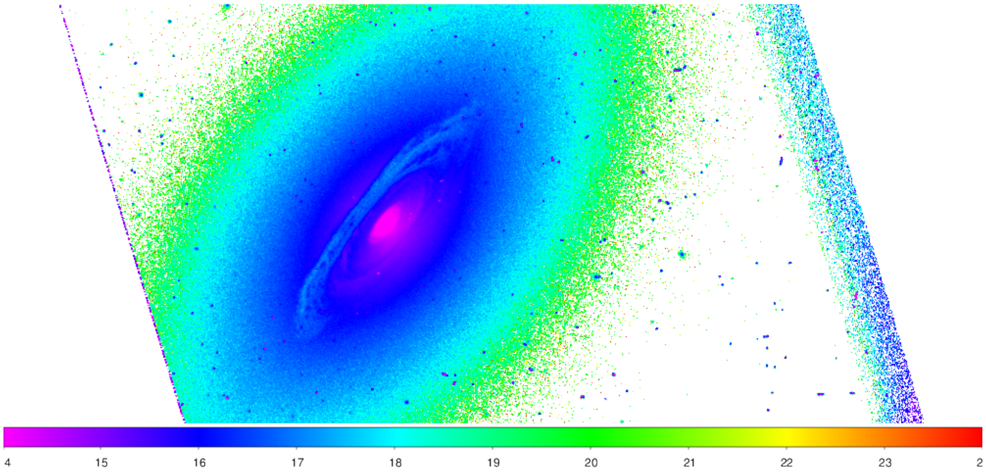

Figure 5.12: Rainbow coloured 555 nm image of NGC 6861 showing the Central Dust Lane. The ratio of the apparent minor axis to the major axis of the dust lane is $\sim 3.5$

## 5.4 Discussion

The SMBH mass of NGC 6861 was measured using three integral Schwarzschild orbit superposition models (Rusli et al., 2013). The results are in good agreement with those they attained and they fall well within the 0.3 dex scatter of the $M_{\rm BH} - \sigma$ relation. The JAM method works better in constraining SMBH mass if there is another way of constraining the $M/L$ ratio and the inclination angle. This is a promising result, as it shows that a Bayesian method can be applied to the problem in a multi-variate manner, and fall within the accepted error bars of historical results. With a bigger sample of SMBH mass measurements, it can be determined whether this addition to the modelling increases the accuracy.

The extra benefits of using a Bayesian analysis and an MCMC sampling of the parameter space do justify this addition if it is not detrimental to the accuracy of the method and it is not computationally expensive to a prohibitive degree.

For the purposes of comparison, there are measurements of the SMBH mass in NGC 6861 in literature. The mass of the blackhole in the core of NGC 6861 has been measured by the gas kinematics technique using the emission line data from HST Space telescope imaging spectrograph (STIS) (Beifiori et al., 2009) and Schwarzschild orbit superposition method using VLT SINFONI IFU data, HST-WFPC2 and European Southern Observatory's MPG/ESO Wide Field Imager data (Rusli et al., 2013). Beifiori et al. (2009) constrained the SMBH mass to a maximum of $1.5 \times 10^9$ M$_\odot$ for inclination angle 33° and a minimum of $3.6 \times 10^8$ M$_\odot$ for an inclination angle of 81°. Rusli et al. (2013) found a mass of $2.2 \pm 0.2 \times 10^9$ M$_\odot$ without dark matter modelling and $2.0 \pm 0.2 \times 10^9$ M$_\odot$ if the effects of dark matter in the galaxy are included.

These results, therefore, suggest that this, like other models to which MultiNest has been applied, can benefit from the extra information that Bayesian methods and Monte Carlo sampling have to offer. The need to have other methods of constraining the $M/L$ ratio has to be kept in mind when planning a project to measure an SMBH mass of a galaxy.

The inclination angle that is constrained in the results is about 89° and is different from the 81° of Rusli et al. (2013). Our results also show that SMBH mass and inclination angle are positively correlated. This suggests that an independent method to constrain the inclination angle may improve the accuracy of the results.

# Chapter 6

# Estimating blackhole mass by virial mass estimate in redshift $0 < z < 3$

## 6.1 Introduction

Tracing galaxy clusters and groups via BTRSs at high redshift depends on the presence of SMBHs and AGNs as well as the sizes of the radio jets they produce. The literature gives contradictory results on the correlation between radio luminosity and SMBH mass. One of the early studies of the correlation between SMBH mass and radio loudness was by Woo & Urry (2002), who used a combined sample of 452 radio-loud and radio-quiet AGNs and reported that radio luminosity does not depend strongly on SMBH mass. Using a sample of 6000 optically selected SDSS quasars at the redshift range $0.1 \leq z \leq 2.1$, McLure & Jarvis (2004) found radio loudness of galaxies to be strongly correlated with SMBH mass, and that radio-loud quasars have systematically higher SMBH masses ($0.16\,\mathrm{dex}\,M_{\odot}$) than radio-quiet quasars on average. The SMBH masses in the McLure & Jarvis (2004) study were measured using the VME method discussed in the next section. The VME method is based on correlations between the FWHM of certain BLR lines and SMBH mass in galaxy cores sampled in the local Universe. Some studies, such as Park et al. (2013), have reported a moderate radio luminosity correlation with SMBH mass. All these results were obtained with different samples and thus comparing the results may not necessarily be straightforward.

In this chapter we look at the black hole mass measurement for high redshift quasars. The method that is used is calibrated using the results of SMBH mass measurement in the local Universe (Kaspi et al., 2000; Peterson et al., 2004). This illustrates how the SMBH mass measurement at all redshifts is an integral part of understanding the evolution of radio loud AGNs. The radio loudness of AGNs, where the ratio of 5 GHz luminosity to B-band luminosity is greater than 10, is due to the radio luminosity of the radio jets, which is believed to be positively correlated with jet power and jet length. Studying the evolution of quasar blackhole masses with redshift will help the investigation of how prevalent high mass SMBHs were at earlier epochs and how that affects the formation of BTRSs and their efficacy as galaxy cluster tracers in the young Universe.

Constraining the correlation between SMBH mass and radio loudness also has a direct influence on how we can incorporate radio jets in cosmological simulations. Within this context, the last couple of decades have seen renewed interest in estimating the central blackhole masses of high redshift AGNs and quasars. The major impetus for this interest has been the results of the RM programmes carried out on low redshift quasars and Seyfert galaxies (Wandel et al., 1999; Kaspi et al., 2000; Peterson et al., 2004), which found correlations between the BLR radius and the continuum flux at some wavelengths and between the blackhole mass and the FWHM of the H$\beta$ emission line, which are discussed in section 6.1.1. These correlations have allowed VME methods to be calibrated for 34 low-redshift AGN (Kaspi et al., 2000). Taking advantage of these correlations, in this chapter, the study of blackhole masses and the search for low mass SMBH is extended to redshift $0 < z < 3$.

There is a dearth of low mass ($\mathrm{M}_\bullet \leq 10^{7.5}\,\mathrm{M}_\odot$) SMBHs measured at high redshift. The VME methods and the availability of more sensitive optical telescopes help in the search for low mass SMBH at high redshift. Data from the Northern Gemini multi-object spectrograph (GMOS-N) in Mauna Kea, Hawaii are used to measure SMBH masses of high redshift quasars so as to increase the statistics of these mass measurements, particularly for low mass SMBHs at high redshift. Assuming SMBH mass correlates with radio luminosity, increased sensitivity of the new generation of radio telescopes will allow us to probe the lower SMBH mass range of the high redshift quasars.

Due to the reliance that RM measurements of $R_{\mathrm{BLR}}$ have on high accuracy monitoring programmes that last up to several years, such measurements are currently only available for a small sample of AGNs (Bentz & Katz, 2015). For estimating the blackhole masses of large samples of AGNs, a crucial result arising from the Kaspi et al. (2000) study is that $R_{\mathrm{BLR}}$ strongly correlates with the AGN monochromatic continuum luminosity at rest wavelength of 5100 Å. McLure & Jarvis (2002) found a correlation between the BLR and the monochromatic luminosity at the rest wavelength of 3000 Å. It is possible, by exploiting this correlation, to produce

VME measurements based on continuum luminosity and H$\beta$ FWHM measurement (Kaspi et al., 2000) and to extend them to the UV with the FWHM measurements of Mg II and C IV emission lines. The effectiveness of this technique has led to a rise in the number of AGN blackhole masses thus studied with a scatter of 0.39 dex (McLure & Dunlop, 2003).

The principal assumption underlying the VME methods is that the dynamics of the BLR are dominated by the gravity of the SMBH. Under this assumption, an estimate of the central SMBH mass can be gained from

$$M_{\rm BH} \approx G^{-1} R_{\rm BLR} V_{\rm g}^{2} \ , \tag{6.1}$$

where $R_{\rm BLR}$ is BLR radius, $G$ is the gravitational constant and $V_{\rm g}$ is the velocity of the line emitting gas, as traditionally estimated from the FWHM of the H$\beta$ emission line.

The VME method's assumption of the gravity being the primary driver of the kinematics of the BLR is subject to the same uncertainties as the RM technique. There are systematic uncertainties such as the angle of inclination relative to the flattened accretion system, or the effects of the unknown angular radiation pattern coupled with the broad radial emissivity distribution (Krolik, 2001). These are difficult to quantify. The possibility of other processes in AGNs, such as magnetically driven winds, being equally responsible for the $V \,\alpha\, R^{-1/2}$ (where $R$ is radius and $V$ is velocity), has not been totally ruled out (Krolik, 2001).

There has been evidence demonstrating that the VME methods produce accurate results (McLure & Jarvis, 2002; McLure & Dunlop, 2003). For the small number of objects for which it is possible to do so, Peterson & Wandel (2000) have shown that the motions of broad-line gas are consistent with being virialised, with the velocity widths of emission lines produced at different radii following the expected $V \,\alpha\, R^{-1/2}$ relationship. Moreover, the blackhole mass estimates produced by the VME method are in agreement with the predictions of the $M_{\rm BH} - \sigma$ relation (Gebhardt et al., 2000; Ferrarese et al., 2001).

### Estimating the BLR radius

The FWHM of some prominent broad emission lines such as the H$\alpha$, H$\beta$, Mg II and the C IV lines in AGNs and quasars have been used, after removing the contaminantion lines such as N II and Fe II, to estimate the BLR radius. For SMBH masses estimated without the use of the RM technique, there has to be a method for estimating the $R_{\rm BLR}$ term of the equation (6.1). The

$R_{\mathrm{BLR}}$ can be estimated well using the AGN's continuum luminosity (Kaspi et al., 2000; Peterson & Wandel, 2000). The results of McLure & Jarvis (2002) and McLure & Jarvis (2004) are used for the $R_{\mathrm{BLR}}$ - $\lambda L_{\Lambda}$ at 3000 Å because they cater for redshifts $z \geq 0.7$ which is where the sample of high redshift quasars lies – throughout this Chapter we use $\lambda L_{\Lambda}$ to denote the continuum flux at wavelength $\Lambda$ and FWHM(Ion) to denote the FWHM of the emission line of that particular ion such that $\lambda L_{3000}$ is the continuum luminosity at the rest wavelength 3000 Å and FWHM(Mg II) is the FWHM of the Mg II emission line. These were fitted with the bi-variate correlated errors and intrinsic scatter (BCES) method of Akritas & Bershady (1996) to get

$$R_{\mathrm{BLR}} = (26.4 \pm 4.4) \left[\frac{\lambda L_{5100}}{10^{37}\mathrm{W}}\right]^{(0.61\pm0.10)} , \tag{6.2}$$

for H$\beta$ by McLure & Jarvis (2002) and

$$R_{\mathrm{BLR}} = (18.5 \pm 6.6) \left[\frac{\lambda L_{3000}}{10^{37}\mathrm{W}}\right]^{(0.62\pm0.14)} , \tag{6.3}$$

for Mg II by McLure & Dunlop (2004).

### 6.1.1 UV blackhole mass estimator

The RM SMBH mass measurements are done using the H$\beta$ emission line and the inferred mass estimates for high redshift SMBH masses are based on the assumption that the same physics is applicable at high redshift. The Mg II emission line is a low ionisation line like the H$\beta$ line. Both emission lines are therefore expected to be photo-ionised at the same region of the BLR. Mg II is found in the UV ($\lambda$2803 Å) and by finding a correlation between it and the H$\beta$ line the VME methods can be extended to the UV wavelength range. A similar rationale may be used for the C IV emission line ($\lambda$1549 Å). This expands the redshift to which the VME methods may be used to a maximum redshift of $z = 4.5$.

The FWHM of the H$\beta$ emission lines are used to measure the BLR radius at redshifts lower than 0.9, whereas Mg II and the C IV lines in AGN and quasars have been used to estimate BLR radii at redshifts higher than 0.9.

McLure & Jarvis (2002) used a sample of 17 Seyfert galaxies and 17 quasars that had been reverberation mapped for SMBH masses to find a correlation between H$\beta$ and Mg II FWHM line measurements and the SMBH mass. They found a very tight relation between the two lines

$\mathrm{FWHM(H\beta)} \equiv \mathrm{FWHM(Mg\,II)}^{1.002(\pm 0.14)}$. This led to the Mg II ($\lambda\lambda$2797 Å, 2803 Å) emission line being used alongside the H$\beta$ ($\lambda$4861 Å) line as a measure of $M_{\mathrm{BH}}$ once the following relation was found between the SMBH mass derived using the Mg II line ($M_{\mathrm{BH}}$(Mg II)) and RM SMBH masses ($M_{\mathrm{BH}}$(RM))

$$\log\, M_{\mathrm{BH}}(\mathrm{RM}) = \log\, M_{\mathrm{BH}}(\mathrm{Mg\,II}) - 0.16\ , \tag{6.4}$$

where the 0.16 offset was meant to ensure the log $M_{\mathrm{BH}}$(RM) : log $M_{\mathrm{BH}}$(Mg II) ratio of unity. They found a best-fitting calibrated formula for Mg II measured SMBH masses to be

$$\frac{M_{\mathrm{BH}}}{\mathrm{M}_{\odot}} = 3.37 \left(\frac{\lambda L_{3000}}{10^{37}\,\mathrm{W}}\right)^{0.47} \left(\frac{\mathrm{FWHM(Mg\,II)}}{\mathrm{km\,s^{-1}}}\right)^{2}\ , \tag{6.5}$$

where $\lambda L_{3000}$ is the continuum flux at 3000 Å and FWHM(Mg II) is the FWHM of the Mg II line.

They calibrated the H$\beta$ SMBH mass measurement to

$$\frac{M_{\mathrm{BH}}}{\mathrm{M}_{\odot}} = 4.74 \left(\frac{\lambda L_{5100}}{10^{37}\,\mathrm{W}}\right)^{0.61} \left(\frac{\mathrm{FWHM}(H\beta)}{\mathrm{km\,s^{-1}}}\right)^{2}\ , \tag{6.6}$$

The accuracy of the calibration is
$<\log\, M_{\mathrm{BH}}(\mathrm{RM}) - \log\, M_{\mathrm{BH}}(\mathrm{Mg\,II})> = 0.00(\pm 0.40)$ ,
and they found the relation between the SMBH mass measurements of H$\beta$ and Mg II lines to be

$$\log M_{\mathrm{BH}}(\mathrm{H}\beta) = 1.00(\pm 0.08) \log M_{\mathrm{BH}}(\mathrm{MgII}) + 0.06(\pm 0.67)\ , \tag{6.7}$$

which is consistent with a linear relation.

Vestergaard & Peterson (2006) recalibrated the study using all available RM results up to 2004 from Peterson & Horne (2004) and Onken et al. (2004). The recalibration, using units of erg s$^{=1}$, led to a new C IV and H$\beta$ VME method's formula of

$$\frac{M_{\mathrm{BH}}}{\mathrm{M}_{\odot}} = 10^{6.91(\pm 0.02)} \left(\frac{\lambda L_{5100}}{10^{44}\,\mathrm{erg\,s^{-1}}}\right)^{0.50} \left(\frac{\mathrm{FWHM}(H\beta)}{10^{3}\mathrm{km\,s^{-1}}}\right)^{2}\ , \tag{6.8}$$

and

$$\frac{M_{\mathrm{BH}}}{\mathrm{M}_{\odot}} = 10^{6.66(\pm 0.01)} \left(\frac{\lambda L_{1350}}{10^{44}\,\mathrm{erg\,s^{-1}}}\right)^{0.53} \left(\frac{\mathrm{FWHM(C\,IV)}}{10^{3}\,\mathrm{km\,s^{-1}}}\right)^{2}\ , \tag{6.9}$$

They found a large scatter of $\simeq 0.47$ dex between the C IV and H$\beta$ mass measurements.

Vestergaard & Osmer (2009) used quasars from a combination of the bright quasar survey (Schmidt & Green, 1983), large, bright quasar survey (Foltz et al., 1987; Hewett et al., 2001) and quasars from the SDSS fall equatorial stripe (Fan et al., 2001) to calibrate for the Mg II line using both the C IV and the H$\beta$ lines. They also calibrated the BLR radius in this relation for continuum fluxes at $\lambda\lambda$1350, 2100, 3000 and 5100. The resultant relation is

$$\frac{M_{\rm BH}}{\rm M_{\odot}} = 10^{\gamma} \left( \frac{\lambda L_{\Lambda}}{10^{44}\,{\rm erg\,s^{-1}}} \right)^{0.47} \left( \frac{\rm FWHM(Mg\,II)}{10^{3}\,{\rm km\,s^{-1}}} \right)^{2} , \tag{6.10}$$

where $\lambda L_{\Lambda}$ are the continuum fluxes at 1350 Å, 2100 Å, 3000 Å and 5100 Å and the values of $\gamma$ are 6.62, 6.79, 6.89 and 6.96 for the afore-mentioned respective values of $\lambda \rm L_{\Lambda}$.

## 6.2 Sample data and reduction

Our sample of galaxies is taken from the seventh Cambridge redshift survey (7CRS) radio catalogues. It is a representative sample of radio galaxies with 151 MHz flux densities $\geq$500 mJy from redshifts $0.8 \leq z \leq 3.0$ (McGilchrist et al., 1990). It covers a sky area of 0.022 sr, containing 130 radio sources, that is subdivided into three sub-areas. 7C-I and 7C-II sub-areas overlap with 5C6 and 5C7 fields of the original 5C Survey Pearson & Kus (1978). The 7C-III sub-area is a sample of 54 radio sources lying in an area of radius 3° centered on $18^{h}\,00^{m}\,00^{s}, +66^{\circ}\,00'\,00''$ (Lacy et al., 1995). 7C-I has 37 sources centered on $02^{h}\,14^{m}\,00^{s}, +32^{\circ}\,00'\,00''$ (epoch B1950.0), covering a sky area of 0.0061 sr. 7C-II is a 0.0069 sr sky area centered on $08^{h}\,17^{m}\,00^{s}, +27^{\circ}\,00'\,00''$ (epoch B1950.0) sample with 39 sources.

There are 23 quasars in the 7CRS sample (Willott & et al., 1998). We list, in Table 6.1, a 14 member sub-sample of those 7CRS quasars for which there are K-band imaging observations, together with their radio luminosities and NIR magnitudes. The 151 MHz observations were done with the Cambridge radio telescope (McGilchrist et al., 1990). The K-magnitudes of the 7CRS quasars were observed with the United Kingdom Infrared Telescope (UKIRT) in Mauna Kea, Hawaii (Willott et al., 2002). In this chapter we quote redshifts from Willott et al. (2002), which are determined from spectra taken with the intermediate dispersion spectrograph and imaging system (ISIS) longslit instrument of the William Herschel telescope (WHT) in Tenerife.

The GMOS-N telescope is an 8 meter class telescope and has better spectral resolution than the

Table 6.1: Redshift, 151 MHz radio luminosity and the K-band magnitude of the sample of 7CRS quasars.

| Galaxy name | Redshift (z) | $S_{151}$ (Jy) | $\log_{10}(\frac{L_{151}}{\mathrm{W\,Hz^{-1}\,sr^{-1}}})$ | $M_K$ |
|---|---|---|---|---|
| 5C6.251 | 1.665 | 0.561 | 26.776 | -24.84 |
| 5C6.291 | 2.910 | 3.728 | 27.692 | -26.62 |
| 5C6.95 | 2.877 | 0.827 | 27.512 | -23.09 |
| 5C6.160 | 1.624 | 0.982 | 26.964 | -24.72 |
| 5C6.237 | 1.620 | 1.665 | 27.106 | -26.58 |
| 5C6.264 | 0.832 | 0.948 | 26.373 | -23.50 |
| 5C6.282 | 2.195 | 0.605 | 27.068 | -23.91 |
| 5C6.286 | 1.339 | 0.676 | 26.720 | -24.34 |
| 5C6.288 | 2.982 | 1.405 | 27.640 | -24.42 |
| 5C7.70 | 2.617 | 2.084 | 27.809 | -24.97 |
| 5C7.87 | 1.764 | 0.843 | 27.132 | -23.28 |
| 5C7.194 | 1.738 | 1.701 | 27.301 | -26.20 |
| 5C7.195 | 2.034 | 0.889 | 27.174 | -24.16 |
| 6CE0824+3535 | 2.249 | 2.42 | 27.56 | |

WHT. It can also get good S/N ratio spectra of high redshift quasars quicker than the WHT. The observations were taken in the second semester of 2007 (Program ID: GN-2007B-Q-94) between the dates 2007-09-02 and 2008-01-30. Some details of the observations of the 7CRS quasar sub-sample are listed in the Table 6.2.

The telescope settings for the observations were designed to catch either the Mg II emission line for galaxies in the redshift range $0.8 \leq z \leq 2.2$ or the C IV emission line for galaxies in the redshift range $2.2 \leq z \leq 4.5$. There is a slight overlap in the theoretical redshift ranges that can be used by the two lines and the upper range of the C IV line is not reached with any of the quasars in the sample.

### 6.2.1 Data reduction

The Gemini IRAF tasks performed in the data reduction are listed below,

- gsflat
- gsreduce
- gstransform

Table 6.2: Details of the GMOS-N spectroscopic observations of the quasar sub-sample.

| Galaxy name | Time | Observation date |
|---|---|---|
| 5C6.251 | 4×300 | 2007-09-07 |
| 5C6.291 | 6×900 | 2007-11-22/23 |
| 5C6.95 | 4×600 | 2007-09-21 |
| 5C6.160 | 4×300 | 2007-09-09 |
| 5C6.237 | 4×300 | 2007-11-23 |
| 5C6.264 | 3×600 | 2007-12-26 |
| 5C6.282 | 2×900 | 2007-11-19 |
| 5C6.286 | 4×600 | 2007-12-26 |
| 5C6.288 | 3×900 | 2008-01-19 |
| 5C7.70 | 6×900 | 2007-11-19/23 |
| 5C7.87 | 8×900 | 2007-12-18 |
| 5C7.194 | 4×300 | 2007-12-20 |
| 5C7.195 | 4×900 | 2007-12-18 |
| 6CE0824+3535 | 8×900 | 2008-01-19 |

- gsappwave
- gemcombine
- gsextract
- gscalibrate
- gsskysub
- gscombine

These tasks achieve data reductions steps that are similar to those undertaken for the SALT longslit spectroscopy data reduction in Chapter 2. There was no illumination correction performed for GMOS-N data.

The first spectroscopy data reduction steps involved were bias subtraction and flat fields. GMOS tasks involved were **gsbias** and **gsflat** with **gsreduce** being used to subtract the flat field and bias values from the science frames.

The next step in the data reduction process was the observation of arc lamps and galaxy spectra. The arc lamps contain gas(es) for which there are *a priori* spectra. These are used to establish how light is dispersed in the telescope and the CCD. GMOS automatically performs this task using the **gswavelength** function. The wavelength solutions are then applied to the galaxy spectra using GMOS's **gstransform** task.

The spectrum is extracted from the CCD with **gsextract** after the background sky spectrum has been removed with GMOS's **gsskysub**. Flux calibration is then done with **gscalibrate**.

The last step is the combining of spectra of the same galaxy that were taken to increase S/N ratio and to ensure that in the event of cosmic rays falling on the spectrum there are at least two extra spectra to allow for minimum statistical comparison of the true spectrum. The task **gscombine** is used GMOS data.

Seven of the 14 quasars in our sample did not have a high enough S/N ratio, of the Mg II and the C IV lines, to allow for a meaningful emission line FWHM measurement. This would affect the SMBH mass determination negatively hence they were dropped from the sample.

Six of the usable quasar spectra are based on the Mg II line, which is embedded in a broad Fe emission line. The wings of the Mg II emission line are strongly blended with the Fe emission line and not subtracting the Fe emission may lead to underestimated FWHM of the Mg II ion (Vestergaard & Wilkes, 2001).

The first step in measuring the FWHM of Mg II is that the template of the Fe II+Fe III line is reconstructed and combined with a power law continuum spectrum and fitted to the quasar spectrum around the Mg II line. The Fe template spectrum that is used is the I Zw 1 template from Vestergaard & Wilkes (2001). The power law continuum that, together with the Fe spectrum, is removed from the observed spectrum leaves the Mg II component as residual. The Mg II spectrum has a narrow line component, where the velocity dispersion is $< 1200\text{kms}^{-1}$ and a broad line component with velocity dispersion $> 1200\text{kms}^{-1}$. The broad emission line is modelled with 2 Gaussians of equivalent FWHM that are centered on 2795.523Å and 2802.698Å respectively. This broad line FWHM is used to determine the velocity dispersion of the BLR and the narrow component is used to account for the emission from the narrow line region of the quasar. The value of the modelled continuum flux at the wavelength of 3000Å is used to estimate the radius of the BLR.

For the C IV line we use a simple linear fit between 1450Å and 1610Å. We determine the continuum flux at 1350Å and the FWHM is determined by fitting a combination of a narrow and broad Gaussians. The broad line Gaussian is used in the calculation of the velocity of the BLR.

In Fig. 6.1 below, the results of a Gaussian fitting of the FWHM are shown for the different quasars. The green curve below the spectrum (in black) shows the deduced continuum flux level of the quasar, from which the BLR radius may be inferred as discussed in the introduction section. The blue curve above it in the six Mg II spectra is a fit of the Fe emission spectrum. This line has to be removed when fitting the Gaussian of the Mg II emission line to reduce its contamination of the line fit and continuum flux level at $\lambda$3100Å. This contamination does not affect the C IV emission line. The purple curve is the Gaussian fit of the Mg II and C IV emission lines from which the FWHM is measured to infer the SMBH mass. The SMBH masses calculated for the sample are listed in Table 6.3.

## 6.3 Results and analysis

Some quasars have broad absorption lines (BAL) that are due to high velocity gas outflows in the galaxy. These broad absorption lines overlap with the C IV and Mg II broad emission lines causing the measurement of their FWHM to be challenging. These BALs have to be modelled out of the Gaussian emission lines when measuring the FWHM and hence the inferred SMBH mass.

### 6.3.1 Results

In Fig. 6.2 the sample of 7CRS quasars is compared with the sample from McLure et al. (2004) and the 3CR sub-sample of radio sources from McLure et al. (2006). This sample is comprised of narrow line radio galaxies that span three decades in radio luminosity and a redshift range of $0.4 \leq z \leq 0.6$. Their blackhole masses were determined using the correlation of the blackhole mass with the mass of the spheroidal component of ETGs. This correlation has a tighter dispersion ($\Delta M_{\rm BH} \approx 0.3\,{\rm dex}$) than the virial mass estimate of galaxy blackhole masses ($\Delta M_{\rm BH} \approx 0.4\,{\rm dex}$).

The correlation between blackhole mass and 151 MHz radio luminosity is studied for these radio galaxies and whether adding the quasar sample affects the correlation. If the quasar sample does not form a subset of the radio-loud galaxy sample, then it would suggest the correlation between

Table 6.3: Results of the sample of 7CRS quasars.

| Galaxy name | Ion name | $M_{BH}$ ($\log M_\odot$) | Redshift ($z$) |
|---|---|---|---|
| 5C6.237 | Mg II | 9.285 | 1.620 |
| 5C6.264 | Mg II | 6.003 | 1.624 |
| 5C6.160 | Mg II | 9.051 | 0.832 |
| 5C6.95 | C IV | 8.158 | 2.877 |
| 5C6.251 | Mg II | 6.546 | 1.665 |
| 5C6.286 | Mg II | 8.522 | 1.339 |
| 5C7.87 | Mg II | 8.867 | 1.764 |

optical AGN activity and low-frequency luminosity extends to the low mass blackholes. This would be in direct disagreement with the findings at $L_{1.4\,\mathrm{GHz}}$ of Best et al. (2005) which found optical activity of AGNs to be uncorrelated with $L_{1.4\,\mathrm{GHz}}$ luminosity.

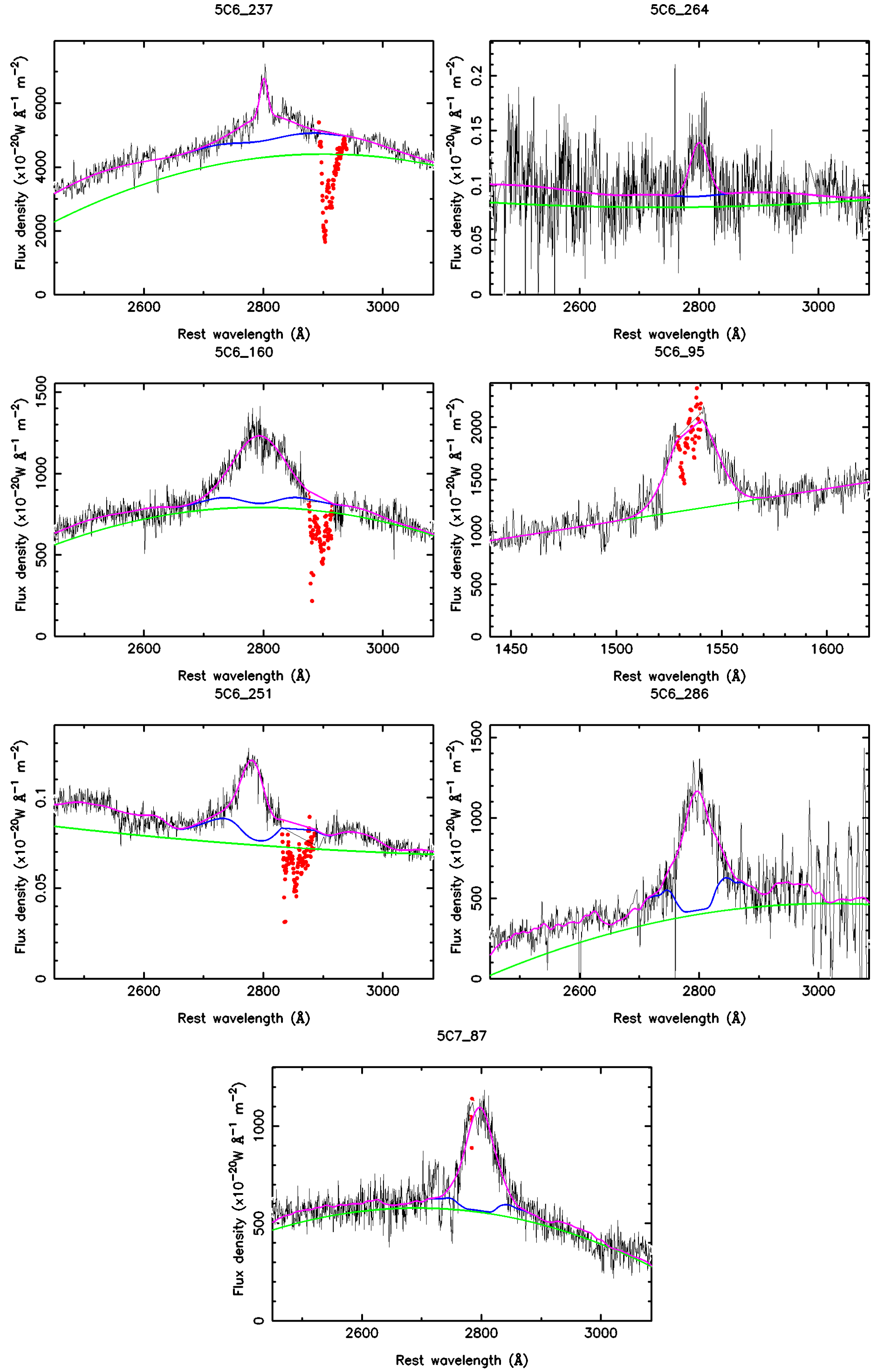

Figure 6.1: The results of the FWHM measurements of the quasars. The other members of the sample do not have good enough S/N in the observed range to make a secure FWHM measurement. The red dots represent the BALs in the vicinity of C IV and Mg II emission lines.

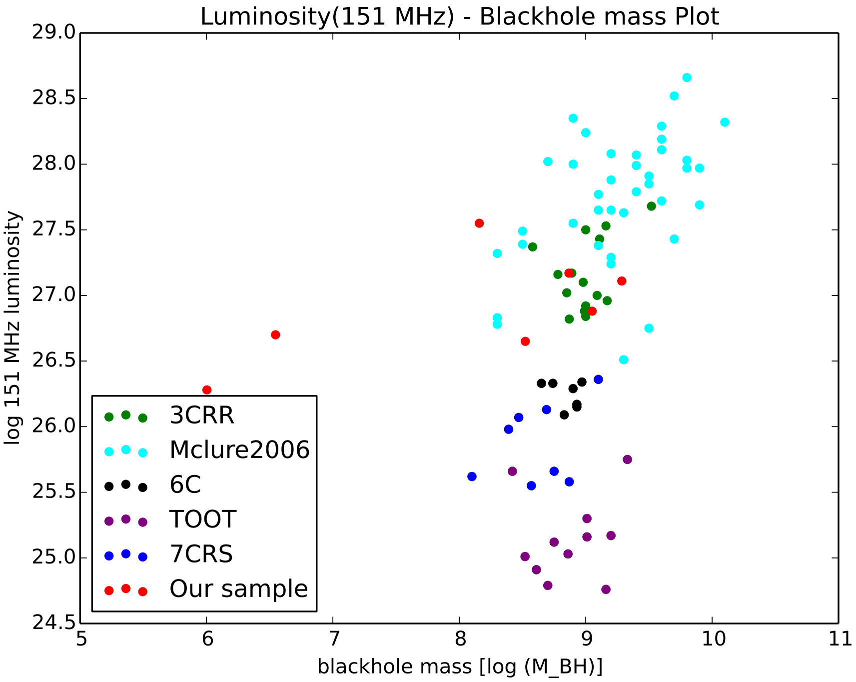

Figure 6.2: A comparison of the quasar sample with the combined sample of quasars at $z \approx 0.5$ from the 3CRR, 6CE and the TOOT catalogues (McLure et al., 2004) as well as McLure et al. (2006) 3CR sub-sample of radio quasars.

The results suggest that the 7CRS quasars are a separate sample from the radio loud AGN sample. The two samples seem to follow different $M_{BH} - L_{151}$ slopes which appear to overlap at the $\log(L_{151}) \approx 27.5\,\mathrm{W\,Hz^{-1}\,sr^{-1}}$. Looking at the points from the sample in Fig. 6.2, one notices that the high SMBH mass quasars have $L_{151}$ luminosity values that overlap with the results from McLure et al. (2004), whose SMBH masses are themselves higher than $10^8$ $\mathrm{M_\odot}$ whilst the low SMBH mass quasars from the sample show a low $L_{151}$ luminosity that gives rise to the different $M_{\mathrm{BH}} - L_{151}$ slope. The low number of measured SMBH masses of our quasar sample make the conclusive determination of the difference in the slopes unfeasible. With more data points, it will be possible to make statistical comparisons of the two populations.

## 6.4 Discussion

The low mass SMBHs exist at high redshift but are rarely observed. The potential effect they have on the relation between black hole mass and host galaxy characteristics can be studied once enough of them are found to allow for meaningful statistics to be derived. This has to be viewed in conjunction with the correlation between blackhole mass and low frequency radio luminosity.

At the highest redshifts, only the C IV line can be used in the visual wavelength regime for VME SMBH mass measurement, because both the H$\beta$ and the Mg II get redshifted to NIR wavelengths. It becomes important to evaluate the effect of the greater dispersion between H$\beta$ and the C IV line results and the offset that has been found between them. The causes for these need further investigation (Richards et al., 2011).

The search for massive galaxy clusters is expected to go back to $z = 2$. This redshift range is covered by the H$\beta$ and Mg II emission lines, hence the problems with the correlation between H$\beta$ and C IV ought not to affect the study of the efficacy of AGN radio jets as tracers of high redshift galaxy clusters.

Park et al. (2013) used 1.4 GHz, 22 GHz and 43 GHz radio data to study the correlation of the blackhole mass and radio luminosity. They found no significant correlation at all those wavelengths. Their results might be affected by the narrow range of SMBH mass ($10^{7.7}M_{\odot} \leq M_{BH} \leq 10^{8.7}M_{\odot}$) in their sample. This requires further investigation because the high frequency radio data, which is less affected by obscuration by the optically thick torus, should be showing more correlation between SMBH mass and radio luminosity.

Our sample is combined with the samples from McLure et al. (2004) and McLure et al. (2006) and the results suggest a moderate correlation between SMBH mass and 151 MHz radio luminosity. The Pearson rank and the t-statistic for the combination of the samples from McLure et al. (2004) and McLure et al. (2006) are 0.4127 and 41.7837, suggesting a high level confidence for a moderate correlation. These change to a Pearson rank of 0.553 and t value of 61.3473 when this sample is added, thus confirming the moderate correlation between blackhole mass and 151 MHz radio luminosity when low mass SMBH are included. These results correspond to better than 99% confidence level for the moderate of correlation. This is in disagreement with the findings of Best et al. (2005) which found no correlation at 1.4 GHz. This may mean that the correlation exits only at low frequencies, which may provide insights into the physics of the different regions of the AGN cores.

The quasars 5C6.264 and 5C6.251 have SMBH masses lower than $10^7\,\mathrm{M}_\odot$ and appear as outliers in the plot in Fig. 6.2. The narrow SMBH mass range of both the Park et al. (2013) and sample with which we are comparing our results could be the reason why we are seeing the low mass SMBHs (those who's mass falls outside the defined narrow range) being outliers. The other possible scenario is that the radio loud quasars form a group that has a different slope in the 151 MHz radio luminosity vs SMBH mass correlation from the narrow line radio galaxies that are studied. The outliers my sample form a line with a different slope that overlaps with the 3CRR and the Mclure2006 samples. In both cases, more sources would provide the statistics needed to investigate the cause of the dichotomy.

McLure et al. (2006) points out that the moderate correlation is due, in part, to the addition of the TexOx-1000 radio source redshift survey (TOOT) sample (Hill & Rawlings, 2003), to their data. This is borne out in our results and, in Fig. 6.2, this sample seems to overlap very well with the McLure et al. (2006) and 3CRR samples in the data and to a lesser extent the 6C data. More data would improve the statistics and help constrain the strength of the correlation between the SMBH mass and the 151 MHz luminosity.

# Chapter 7

# BTRSs and their host environments[1]

## 7.1 Radio galaxy-stellar mass correlation

The largest radio jets are found in the most massive galaxies in the Universe, however, there does not seem to be a correlation between the stellar mass of the host galaxy and the jet size. ETGs are the more prevalent galaxy type at the high mass end of the galaxy mass function (Heckman, 1983). To study the largest AGN jets, one has to look at the most massive galaxies and their environments.

SMBHs are found at the cores of all massive galaxies (Kormendy & Richstone, 1995). They are believed to be the engines that power the radio jets of AGNs. Kauffmann et al. (2003) found that the fraction of AGNs in the nearby Universe grows steadily from 10% for galaxies with stellar mass of $10^{10}$ $M_\odot$, to about 80% for $10^{11}$ $M_\odot$ galaxies. It flattens out at about 100% for masses greater than $10^{12}$ $M_\odot$. Hence, the greater the mass of a galaxy, the more likely it is to contain an AGN.

The prevalence of radio-loud galaxies was found to rise steeply from 0.01% for stellar masses of $3 \times 10^{10}$ $M_\odot$ to about 30% for $5 \times 10^{11}$ $M_\odot$ (Best et al., 2007). Therefore, there is a heavy mass dependence of jet length, and that should be taken into account when predicting the results of BTRSs that can be observed. The optical properties of radio-loud ellipticals are indistinguishable from those of radio-quiet ellipticals (Kormendy & Djorgovski, 1989). Fanaroff-Riley galaxies have kpc-scale relativistic jets emanating from their hosts. Due to projection effects and other biases, it is challenging to constrain the number of extended radio sources that are BTRSs. A look at

---

[1] This Chapter is adapted from the journal article Mguda et al. MNRAS **446**,3310-3318(2015)

the different simulations of AGN jet interactions with the ICM reveals the difficulty that past studies had faced. Each simulation that has been done chooses different values for the variables in the bending equation discussed in (Section 1.3.3).

AGN jets have observed lengths in the range $\simeq 10^{1-3}$ kpc (Hardcastle et al., 1998; Blanton et al., 2000), whereas others observed them to be in sub-kpc range (Alberdi et al., 1993), with better resolution and sensitivity offered by SKA and its pathfinders, we may still find that there a continuous distribution of jet lengths that goes from sub-parsec to Megaparsec range. Many properties of AGN jets, such as jet density, ICM density and average jet velocities are still not well understood. The lack of understanding of these open questions adversely affects the ability to match numbers of simulated galaxies to observed BTRSs. This has proven to be a limitation when studying specific aspects of jet bending and jet-ICM interactions because these studies would be better served by well constrained jet physics. This chapter explores two methods of achieving this generality, and the results of one of them are compared to observations. Both methods are equally applicable to the MareNostrum Universe simulation, and their results are comparable. The Ferrari (1998) analysis is chosen, insofar as it applies to cluster environments, and tweaked only where it is necessary. It is compared to a method pioneered by O'Dea & Owen (1987) that is based on the minimum pressure that a jet should have in order to propagate in the ICM.

This Chapter uses the MareNostrum Universe simulation (Gottlöber et al., 2006), as a representative portion of the Universe in which to study the motions of galaxies in their group and cluster environments. This is done in an effort to find a method of constraining the number of BTRSs that can be observed with radio surveys. Focus is limited to AGN jets with large linear size ($r \geq 50\,\text{kpc}$), which are generally found in massive galaxies, where $\mathrm{M_{gal}} \geq 10^{11}\ \mathrm{M_\odot}$. The following assumptions are made,

- There is a minimum ram pressure that AGN jets of length greater than 50 kpc require in order to show bending. This critical ram pressure is introduced as a simplification that allows the use of a simple abundance matching scheme to determine the masses of the galaxies inferred from the simulation.
- The critical ram pressure will be applied based on the bending equation without regard for the differences between FR I and FR II galaxies' jet physics.

The following section discusses the method used to infer the existence of BTRSs from the results of the MareNostrum Universe simulation. The identification of galaxy halos from the dark matter distribution in the simulation is reviewed as well as the matching of simulated galaxy halos to observed galaxy masses. Determination of ram pressure from the characteristics of the galaxy halos and their environments is also discussed.

## 7.2 Simulation and methodology

The results of the MareNostrum Universe simulation, described in detail by Gottlöber et al. (2006), at the present epoch, are used to constrain the velocities of galaxies and the densities of their environments. These values are the inputs to the bending equation that allow for a way to infer the ram pressure that an AGN jet would experience from its environment. Using the entropy conserving GADGET-2 code, the MareNostrum Universe simulation follows the non-linear evolution of the gas and dark matter cosmic density fields from $z = 40$ to the present epoch in 135 time steps of $10^8$ years each (Springel, 2005). It employs the flat $\Lambda$CDM model with the following parameters: $\Omega_\mathrm{m} = 0.3$, $\Omega_\Lambda = 0.7$, $\Omega_\mathrm{b} = 0.045$, $\sigma_8 = 0.9, h = 0.7$ within a co-moving box with $500\,h^{-1}$ Mpc sides. It models both dark matter and baryonic components using $1024^3$ particles per species. The mass of each gas particle is $1.5 \times 10^9$ $h^{-1}\mathrm{M}_\odot$ and the mass of each dark matter particle is $8.3 \times 10^9$ $h^{-1}\mathrm{M}_\odot$. It uses smoothed particle hydrodynamics technique to solve the equations of gas dynamics adiabatically by excluding radiative processes and star formation.

### 7.2.1 Halo finding

Since galaxy formation follows the dark matter distribution, the presence of its overdensity is used as a tracer of galaxy halo existence. The hierarchical friends-of-friends (FoF) algorithm of Klypin et al. (1999) is employed, with progressively shorter linking lengths of $b_n = \frac{b}{2^n}$ with $n = 0, 3$, to classify clusters and groups ($n = 2$) and galaxies ($n = 3$) respectively.

The FoF algorithm classifies two particles to be ‘friends’, meaning ‘members of the same group’, if they are separated by a distance less than a certain linking length. It then merges all pairs of particles that fall within the linking length, $b$, into one group. In this algorithm, the linking length, $b$ is the only free parameter (Klypin et al., 1999). The linking length is defined in units of the mean particle separation $\bar{l}$ as $b = l/\bar{l}$, where $l$ is the mean distance between the particles being classified. It has been used successfully to define groups and clusters in simulations (Huchra & Geller, 1982; Press & Davis, 1982; Einasto et al., 1984).

The advantages of the FoF algorithm are the single free parameter — which makes it easy to implement — as well as its ability to allow for any shape for structures of the halos and independence from the halo centre. The latter makes it useful for classifying triaxial halos in simulations. Its drawbacks are that it is difficult to interpret the halo mass, and that halo masses are sensitive to numerical resolution and the presence of substructure.

A linking length of $b_0 = 0.17$ times the mean particle separation corresponds to a virial overdensity, where clusters can be separated from voids (Gottlöber et al., 2006). A linking length of $b_n$ corresponds to a density of $8^n$ times the mean particle density in the simulation. For a galaxy, $n = 3$ is used to get $b_3 = 0.02125$, which is 512 times the virial overdensity. This is applied to any $b_3$ overdensity of at least 36 dark matter particles or more for a galaxy, to avoid spurious dark matter particle associations. It is the motion of these galaxies through their host halos that is used to calculate the ram pressure experienced by the AGN jets.

### 7.2.2 Determining the critical ram pressure

The method described below is used to find the ram pressure in the simulation and compare it to the ram pressure necessary to form BTRSs in observations. The average ram pressure required to bend radio jets may be used to extract data parameter values from the MareNostrum Universe simulation by modifying the analysis pioneered by Ferrari (1998). In the analysis, which does not discriminate between NATs and WATs or the different types of FRGs, the average number density $6.74 \times 10^{-3}\,\mathrm{cm}^{-3}$ used by Ferrari (1998), is adopted for the average density of the jet. This is written as a ratio of the critical density of the universe as $\eta = \frac{\rho_{\mathrm{jet}}}{\rho_{\mathrm{crit}}}$, where the WMAP baryon density ($\rho_{\mathrm{crit}} = 0.25\,\mathrm{m}^{-3} \pm 0.01$) is used (Bennett, 2003). This results in a dimensionless number $\eta = 27000$.

The position of a radio galaxy in its host group/cluster is usually associated with the morphology of its bent jet. Hence one can investigate the conditions for jet bending at different radii in clusters to gain insights into NATs and WATs. NATs are usually observed to be situated in the outskirts of galaxy groups and clusters. This has led to the long-held belief that they are a product of the ram pressure experienced by the AGN jets of a galaxy moving through the ICM (Miley et al., 1972). WATs are usually associated with BCGs (O'Donoghue et al., 1993), which are always located near the centres of the clusters (Sakelliou & Merrifield, 2000). BCGs generally have a low velocity relative to their host cluster which suggests that ram pressure may be equally reliant on the velocity and ambient density for the creation of the bent morphology.

The ICM in poor clusters (groups) has a density range of $10^{-5}\mathrm{cm}^{-3} \leq n_e \leq 10^{-4}\mathrm{cm}^{-3}$ and a temperature range of $10^5\mathrm{K} \leq T \leq 10^7\mathrm{K}$, whereas the ICM in rich clusters has a density range of $10^{-3}\mathrm{cm}^{-3} \leq n_e \leq 10^{-2}\mathrm{cm}^{-3}$ and a temperature range of $10^7\mathrm{K} \leq T \leq 10^8\mathrm{K}$ (Pisano et al., 2004; Davé et al., 2001). Venkatesan et al. (1994) argued that the velocity of the host galaxy with respect to the ICM should be of the order of 1000 $\mathrm{km\,s^{-1}}$ for ram pressure to be the cause of the bent tail morphology. Far lower galaxy velocities have been found in some BTRS in literature. For the jets of AGNs to be visibly bent, the ram pressure caused by the jet on the ambient medium must be of the same order of magnitude as the ram pressure caused by the motion of the galaxy through the ambient medium. This also takes into account the radius of curvature that the jet has to have for it to be discernibly bent. O'Dea & Owen (1985) calculated a mean relative velocity of $\approx$ 547 $\mathrm{km\,s^{-1}}$ for a sample of observed NATs in rich clusters. Using the bending equation in (1.3.3), with $R_\mathrm{P} = 1\,\mathrm{kpc}$, $R_\mathrm{bend} = 20\,\mathrm{kpc}$ and $\rho_\mathrm{jet} = 1.5 \times 10^{-3}\,\mathrm{cm}^{-3}$ O'Dea & Owen (1985); Jetha et al. (2006) found the minimum galaxy velocities needed to achieve bent morphology to be $\simeq$ 870 $\mathrm{km\,s^{-1}}$ for a sample of WATs. The values $R_\mathrm{P} = 1\,\mathrm{kpc}$ and $R_\mathrm{bend} = 20\,\mathrm{kpc}$ are a useful ratio between the jet pressure scale height and the jet radius of curvature.

For FR I galaxies, the average jet velocity $\beta = \frac{v}{c}$ was found to be $0.54c \pm 0.03$, where the jets flare (Arshakian & Longair, 2004). Analysing different samples and using different methods of analysis, the jet speeds for FR II galaxies was found to vary between $0.5c \leq v \leq 0.7c$ (Wardle & Aaron, 1997; Arshakian & Longair, 2004).

The average velocity of the jet $v_\mathrm{jet} = 0.008c$ is also used as the average value along the whole jet (Ferrari, 1998). The following dimensionless constants are defined $\zeta = \frac{R_\mathrm{bend}}{R_\mathrm{P}} = 20$ and $\eta = \frac{\rho_\mathrm{jet}}{\rho_\mathrm{crit}}$ and the bending equation is rearranged to be

$$\rho_\mathrm{ext} v_\mathrm{gal}^2 = \frac{\eta}{\zeta} \times (0.008c)^2 \ , \tag{7.1}$$

where $\eta = 27000$, which gives us

$$\rho_\mathrm{ext} v_\mathrm{gal}^2 = \eta\zeta \times (0.008c)^2 = 7.7645 \times 10^9 \rho_\mathrm{crit}(\mathrm{km\,s^{-1}})^2 \ , \tag{7.2}$$

where $\rho_{\rm ext}$ is expressed as a ratio of the ICM density divided by the critical density of the universe ($\rho_{\rm crit}$).

This allows the extraction of these quantities directly from the simulation by calculating the average velocity of the dark matter particles that form the galaxy. Using the average velocity of the gas particles that lay between a 50 kpc and 100 kpc radius of the core of the galaxy, the velocity of the galaxy can be calculated with respect to the surrounding gas. This is significant, as the gas density and gas velocities measured correspond to the volume of the ICM that will be interacting with the potential AGN jets. This makes it easy to compare the calculation of the ram pressure due to the environment to a single quantity (jet's internal pressure). A galaxy core is chosen to consist of at least 36 dark matter particles. This corresponds to a total dark matter mass of $\geq 2.99 \times 10^{11}$ $\mathrm{M}_{\odot}$. The simulation provides velocity and position for each of the gas and dark matter particles. These are used to calculate the average density, the average velocity and position of gas particles in displacement bins of 0.1 dex.

### A method based on observed radio luminosity

The average jet values that are used in the Ferrari (1998) analysis cannot be easily discerned from radio jet observations. An alternative method would be to use the jet luminosity as a proxy for the ram pressure that the jet exerts on its environment. O'Dea & Owen (1987) pioneered a method which is based on the assumption that, for the bending equation, there is a minimum amount of the jet's ram pressure on the environment ($\rho_{\rm jet} v_{\rm jet}^2$) that can be inferred from the radio luminosity of the jet. This analysis is similar to the Ferrari (1998) analysis, but it has the advantage that the minimum pressure ($P_{\rm min}$) can be directly inferred from observations. It has been used successfully in BTRSs found in galaxy groups to calculate the bending of jets (Freeland & Wilcots, 2011; Morsony et al., 2013).

The aforementioned minimum pressure is a result of the energy due to the magnetic field, relativistic protons and electrons as well as non-relativistic (thermal) forces that are acting on the jet.

$$P_{\rm min} = \frac{B_{\rm min}^2}{8\pi} + \frac{E_{\rm min}}{3\phi V} + nKT \ , \tag{7.3}$$

where $B_{\rm min}$ is the minimum magnetic field pressure and $E_{\rm min}$ is the minimum pressure from relativistic particles. The thermal energy part has $n$ for the number of particles, $K$ for the Boltzmann constant and $T$ for temperature. They are respectively given by

$B_{\rm min} = [2\pi(1+k)C_{12}L_{\rm rad}(V\phi)^{-1}]^{\frac{2}{7}}$ G and
$E_{\rm min} = [V\phi(2\pi)^{-1}]^{\frac{4}{7}}[L_{\rm rad}(1+k)C_{12}]^{\frac{4}{7}}$ erg,
where $C_{12}$ is a constant that depends on the radio luminosity's spectral index $\alpha$ and the frequency cutoff, $k$ is the ratio of the relativistic electron energy to the relativistic proton energy, $V$ is the volume of the radio source and $\phi$ is the form filling factor of the source volume (O'Dea & Owen, 1987).

The analysis assumes the following,

- The thermal energy is much less than the energy from the magnetic field and the relativistic particles ($nKT\ \approx 0$).
- The synchroton spectrum is integrated from 10 MHz to 10 GHz and the spectral index $\alpha\ =\ -0.55$.
- The relativistic electrons and relativistic protons have equal energies (i.e. $k\ =\ 1$).
- The jets are cylindrical and uniformly filled with relativistic particles and the magnetic field (i.e. $\phi\ =\ 1$).

This gives an equation of the minimum pressure $P_{\rm min}$ as,

$$P_{\rm min} = (2\pi)^{-\frac{3}{7}}\frac{7}{12}[C_{12}L_{\rm rad}(1+k)(\phi V)^{-1}]^{\frac{4}{7}}\,{\rm erg\,cm^{-3}}\ . \tag{7.4}$$

A parameter $\aleph$ is introduced such that, from the bending equation, the ram pressure on the jets due to galaxy motion through the ICM is of the order of unity with the jet bending angle and the minimum pressure internal to the jet ($\rho_{\rm ext}v_{\rm gal}^2\ \approx\ \frac{R_{\rm bend}}{R_{\rm P}}\aleph P_{\rm min}$). Freeland & Wilcots (2011) measured $P_{\rm min}$ for their sample of seven radio galaxies. From that sample the mean value was determined to be $2.4\times10^9\rho_{\rm b}(\ {\rm km\,s^{-1}})^2$ where $\rho_{\rm b}$ is the average baryon density in the Universe. The minimum and maximum $P_{\rm min}$ values in their sample were $1.0\times10^9\rho_{\rm b}(\ {\rm km\,s^{-1}})^2$ and $4.1\times10^9\rho_{\rm b}(\ {\rm km\,s^{-1}})^2$ respectively. This results in an average ram pressure value of

$$\rho_{\rm ext}v_{\rm gal}^2\ =\ 2.4\times10^9\rho_{\rm b}({\rm km\,s^{-1}})^2\ , \tag{7.5}$$

where the density of the environment ($\rho_{\rm ext}$), is expressed as a ratio of the ICM density divided by the critical density of the universe.

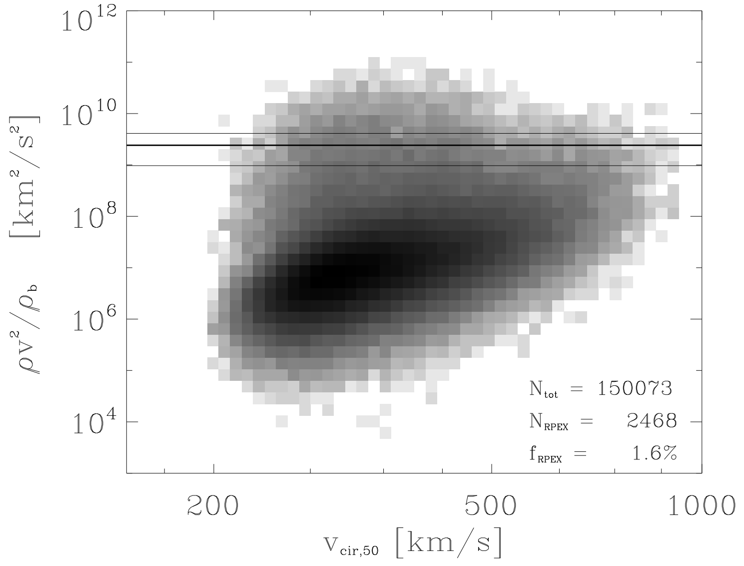

Figure 7.1: The number of galaxy halos that have sufficient ram pressure to have bent jets using the minimum pressure formalism of O'Dea & Owen (1987). The x-axis is the circular velocity in $\mathrm{km\,s^{-1}}$ due to the gravitational potential of the dark matter particles and the y-axis is the ram pressure due to the motion of the galaxy through the ICM as a ratio of the mean density of the Universe ($\rho_b$). The three horizontal lines shown correspond to the $1.0 \times 10^9 \rho_b$ $\mathrm{km\,s^{-1}}$, $2.4 \times 10^9 \rho_b$ $\mathrm{km\,s^{-1}}$ and $4.1 \times 10^9 \rho_b$ $\mathrm{km\,s^{-1}}$ from bottom to top. The lower average ram pressure within the jet ($1.0 \times 10^9 \rho_b$ $\mathrm{km\,s^{-1}}$) translates 3.2% of galaxies being potential BTRSs and $2.4 \times 10^9 \rho_b$ $\mathrm{km\,s^{-1}}$ and $4.1 \times 10^9 \rho_b$ $\mathrm{km\,s^{-1}}$ yield 1.6% and 1.1% potential BTRSs respectively.

Fig. 7.1 shows the results of the ram pressure based on average values for internal jet velocity in the MareNostrum Universe simulation. The x-axis is the circular velocity in $\mathrm{km\,s^{-1}}$ due to the gravitational potential of the dark matter halos and the y-axis is the ram pressure due to the motion of the galaxy through the ICM as a ratio of the mean density of the Universe ($\rho_b$). The three horizontal lines shown correspond to (from bottom to top) $1.0 \times 10^9 \rho_b$ $\mathrm{km\,s^{-1}}$, $2.4 \times 10^9 \rho_b$ $\mathrm{km\,s^{-1}}$ and $4.1 \times 10^9 \rho_b$ $\mathrm{km\,s^{-1}}$. Throughout the rest of the chapter the results of the middle line ($2.4 \times 10^9 \rho_b$ $\mathrm{km\,s^{-1}}$) are used for ram pressure based on jet luminosity which yields 2468 potential BTRSs. It is possible, by tweaking some of the free parameters in the bending equation, to get exactly the same results using the two different approaches. They both provide a self-consistent way of addressing the problem of a statistical approach to searching for

BTRSs in simulations and galaxy surveys. The rest of the chapter continues using the results of the minimum synchroton pressure of the jet due to its having more potential BTRSs. The two methods are expected to yield results that are qualitatively similar.

### 7.2.3 Comparing simulated galaxy mass with observed stellar mass

Abundance matching, discussed below, is used to compare the masses of our MareNostrum simulated galaxies with the SDSS galaxy stellar masses from Bell et al. (2003). Bell et al. (2003) used the K-band luminosity function to translate the luminosity of the Sloan Digital Sky Survey Early Data Release (Stoughton, 2002) in conjunction with the Two Micron All Sky Survey Extended Source Catalogue (Jarrett et al., 2000) into stellar masses of the galaxies.

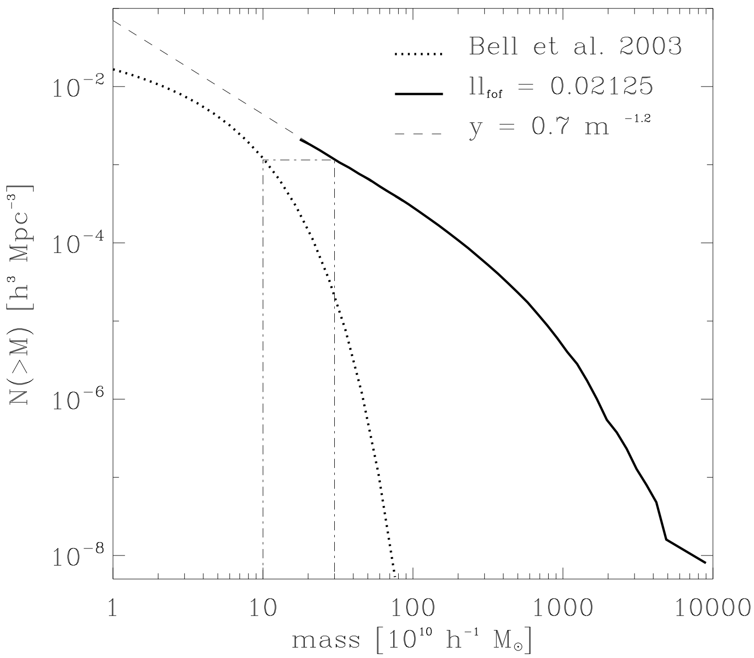

Figure 7.2: Abundance matching of the results of Bell et al. (2003) with MareNostrum Universe simulation. The cumulative number density of the Schechter luminosity function derived by Bell et al. (2003) (dotted line) is matched with the MareNostrum simulated galaxies (dark solid line). The range of stellar masses of the corresponding SDSS galaxies is $8 \times 10^{10}\ h^{-1}\mathrm{M}_{\odot} \leq \mathrm{M}_{*} \leq 7 \times 10^{11}\ h^{-1}\mathrm{M}_{\odot}$.

To match the abundances of the simulated galaxies to SDSS/2MASS galaxy stellar masses, the cumulative number densities of the different galaxy masses derived in Bell et al. (2003) as well as the cumulative number densities of MareNostrum simulated galaxies, whose cores have more than 36 dark matter particles, are compared. Both number densities are then matched, such that equal abundances translate to equivalence of the observed galaxy stellar mass to the simulated galaxy dark matter mass.

Fig. 7.2 shows the abundance matching results of the MareNostrum galaxy halos of 36 dark matter particles or more, with the stellar masses of SDSS from Bell et al. (2003). The x-axis represents the mass and the y-axis the abundance of galaxies of a certain mass. The dotted curve represents the mass function of galaxies from Bell et al. (2003) and the solid curve is the mass function of the galaxy dark matter halos in the MareNostrum Universe. Looking at Fig. 7.2, the thin solid box on the plot shows that 36 dark matter particles, which have a simulation mass of $2.99 \times 10^{11}$ $\mathrm{M}_{\odot}$, have the same abundance as a galaxy of mass greater than $1.0 \times 10^{11}$ $h^{-1}\mathrm{M}_{\odot}$. This allows a translation of the simulation results into observable quantities for the purposes of comparison. This gives an order of magnitude estimation of what can be expected from observations. These data can be used to infer how many radio-loud galaxies are likely to be BTRSs.

## 7.3 Results

By using a linking length $b = 0.17$ all clusters in the simulation can be located. This allows the measuring of the mass of the dark matter within the cluster. Within each cluster, the coordinates of the centre of mass of the cluster can be determined, which may be influenced by the presence of substructure and be off the geometric centre. This would then facilitate the measuring of the distance from the centre of mass of the simulated galaxies to the core of the nearest clusters as well as the masses of those cluster environments.

The parent cluster of a galaxy can affect the jet in two ways, namely

- The mass of the cluster determines the gravitational potential around which the galaxy rotates and this in turn determines the circular velocity that the galaxy can reach.
- The mass of the cluster determines the density of the gas within the cluster as well as the density profile.

This section discusses the characteristics of the cluster environments, where the conditions for bending the jets can be found. The important parameters under consideration are, the mass of the total cluster and its radius. The density and velocity of the galaxy are only used for the calculation of the bending equation.

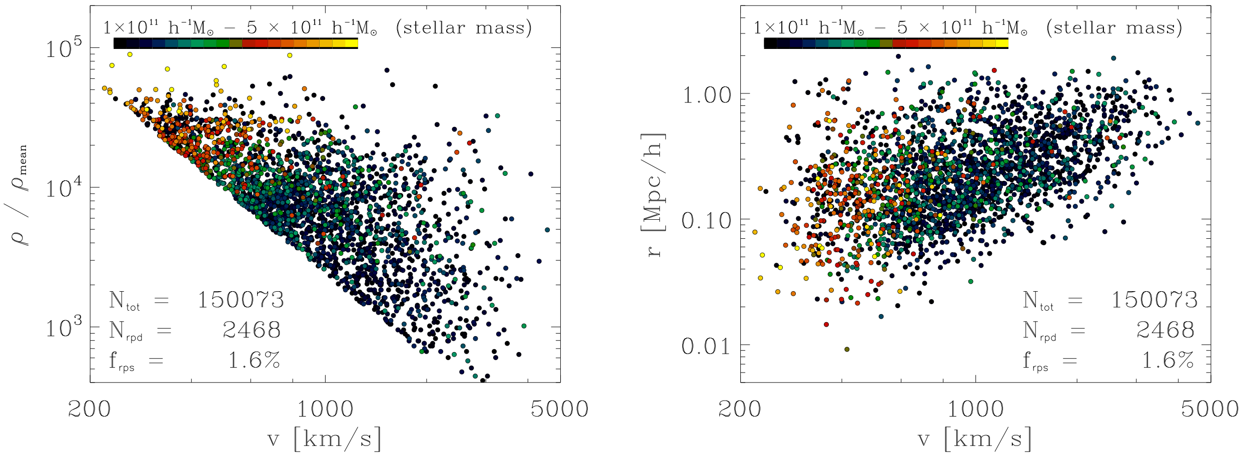

Figure 7.3: *Left panel:* The average density of the environment versus velocity for candidate galaxies, which fulfill the bending criterion (Section 7.2.2). The color coding reflects the stellar masses as derived from the abundance matching procedure discussed in Section 7.2.3. The high mass galaxies with low velocities may correspond to WATs, whereas the high velocity subhalos are more often observed as NATs. *Right panel:* The distance to the host halo's centre of mass versus velocity for the same set of candidate galaxies as displayed above. High mass galaxy candidates (shown in red and in yellow) tend to have low relative velocities and are located close to the centre of the clusters, where wide angle tails are observed.

There are 150 073 total galaxies in the MareNostrum Universe simulation that consist of 36 or more dark matter particles, and 1.6% of them are in environments where, if they have jets of requisite length, they would be BTRSs. This percentage is better expressed as the ratio of radio-loud galaxies in the particular mass bin (i.e. 1.6% of radio-loud galaxies are expected to be BTRSs). This is a better way to translate the results of this study to observations because it takes into account the galaxy mass dependence of the length of the jets. Fig. 7.3 shows the distribution and velocities of the galaxies that are potential BTRSs. In both plots, the x-axes represent the velocity at which the galaxy is travelling through the environment. The left hand panel in Fig. 7.3 has a y-axis that represents the density of the environment as a ratio of the mean density of the Universe. That panel also shows a cutoff line above which the 2468 BTRS candidates are found. This line corresponds to the critical ram pressure at the particular galaxy velocity. The high stellar mass galaxies, shown in yellow and in red, are usually ETGs. They are concentrated in the high density environments, in the upper left hand corner of the left panel. Fig. 7.3 shows that there are only a few environments where the density is higher than $4 \times 10^4 \rho_\mathrm{b}$. It can be inferred that these densities are found in the most massive galaxy clusters. There are also very few BTRSs that have velocities higher than 2000 $\mathrm{km\,s^{-1}}$. Such velocities would generally be found in the most massive clusters, of which there is a limited amount in the MareNostrum simulation. In the right panel of Fig. 7.3 the y-axis represents the distance from the center of the cluster in units of $h^{-1}$Mpc in the simulation. Most of the BTRSs lay between 50 $h^{-1}$ kpc and 1.00 $h^{-1}$Mpc from the centre of the cluster. The same high stellar mass BTRS candidates occur at distances from less than 100 $h^{-1}$ kpc all the way to 1.00 $h^{-1}$Mpc from the cluster core. The lower velocity BTRS candidates can only be found in high density regions of clusters. This suggests that massive clusters can have high densities up to a radius of about 1 $h^{-1}$Mpc.

### 7.3.1 BTRS cluster environments

The velocity of the galaxy increases the further one goes from the cluster core, and the gas density decreases. This gives rise to the question of the importance of ICM density in jet bending as a function of cluster mass. To constrain this gas density-galaxy velocity dichotomy, the masses of the clusters and the gas density in the environments where BTRSs can be found, are investigated. This allows the classification of the clusters as groups (poor clusters) or (rich) clusters. With this, the probability of the ram pressure being the cause of the bent morphology in BCGs is probed.

Fig. 7.4 compares the distribution of potential BTRSs, when the ram pressure is measured at the radius ($r$) from zero to 50 $h^{-1}$ kpc (blue dotted histogram), versus measuring at the radius 50 $h^{-1}$ kpc $\leq r \leq$ 100 $h^{-1}$ kpc. Looking at the results plotted in Fig. 7.4, where the x-axis represents the velocity of the galaxy halo with respect to its environment and the y-axis is the number of galaxies that have a particular range of velocities, there is very little difference in choosing

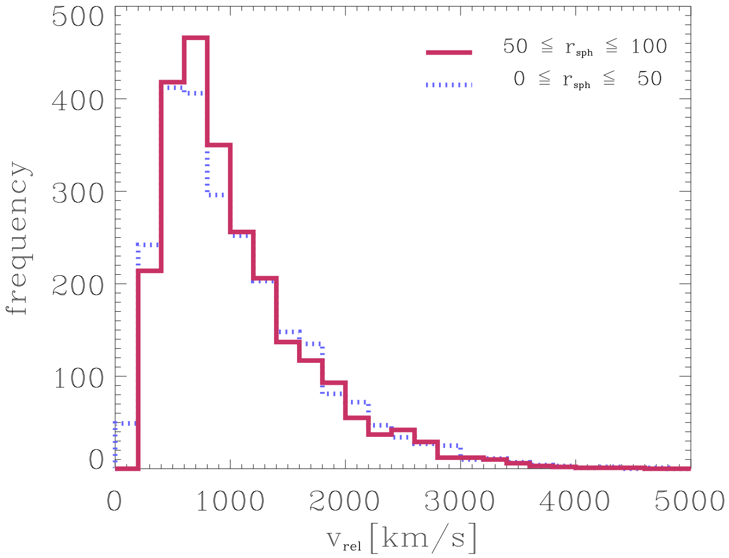

Figure 7.4: The number of BTRSs from the simulation found by calculating the jet bending within 50 $h^{-1}$ kpc radius (solid red histogram) of the galaxy core compared to calculating bending at the radius between 50 $h^{-1}$ kpc and 100 $h^{-1}$ kpc (dotted blue histogram). Both radii yield results that are qualitatively similar. Assuming a longer jet radius would yield similar results to using a jet radius of less than 50 $h^{-1}$ kpc.

to measure ram pressure at the radius 50 $h^{-1}$ kpc $\leq r \leq$ 100 $h^{-1}$ kpc in comparison to using the radius of 0 $h^{-1}$ kpc $\leq r \leq$ 50 $h^{-1}$ kpc. In observations, the gas that is found within the galaxy is seen to be moving with the galaxy's stellar and dark matter content, except in special cases such as ram pressure stripping or galaxy-galaxy interactions. It is, therefore, believed not to be part of the ICM. A galaxy's stellar extent is observed to be far less than the dark matter halo. The need for the consideration of ICM effects and the general sizes of dark matter halos, which are less than 50 $h^{-1}$ kpc in radius, makes the choice of the larger radius to be more appropriate for analysis in this study. There is a conundrum when looking to measure jet-ICM interactions in that, at the low mass end of the galaxies, stellar masses of $10^{11}$ $M_\odot$ are expected, which corresponds to $10^8$ $M_\odot$ black hole masses in empirical relations. Huarte Espinosa & Mendoza (2007) found the length of an AGN jet to be $r_{\rm jet} \propto 100 \times M_{\rm BH}^{\frac{1}{3}}$ in parsecs and that these blackholes create AGN jets that barely exceed 50 $h^{-1}$ kpc in length. This argument can, therefore, be used to justify the choice of jet radius of host galaxies with masses greater than $10^{11}$ $M_\odot$ to be greater than 50 $h^{-1}\,\mathrm{kpc}$.

Results in Fig. 7.4 also show the velocities of the galaxies to peak at about 1000 $\mathrm{km\,s^{-1}}$ with a long high velocity tail. The low velocity end begins at 400 $\mathrm{km\,s^{-1}}$ with only a few cases of lower velocity BTRSs. This result is borne out by observations for both NATs and WATs (O'Dea & Owen, 1985; Jetha et al., 2006).

### 7.3.2 Dependence on cluster mass

Fig. 7.5 shows the fraction of galaxies that are potential BTRSs as a function of cluster mass. The x-axis shows the cluster mass in mass bins of $\log 0.5\ h^{-1}\mathrm{M}_\odot$, whereas the y-axis shows the number of BTRSs in each mass bin. The black solid line corresponds to the fractions of BTRSs found based on $2.4 \times 10^9 \rho_\mathrm{b}(\ \mathrm{km\,s^{-1}})^2$, and the grey area above and below the line, corresponds to the lower limit ($1.0 \times 10^9 \rho_\mathrm{b}(\ \mathrm{km\,s^{-1}})^2$) and the upper limit ($4.1 \times 10^9 \rho_\mathrm{b}(\ \mathrm{km\,s^{-1}})^2$) respectively. Logarithmic growth of the percentage of BTRSs as a function of cluster size is observed. The fraction for clusters of mass $10^{13.5}\ h^{-1}\mathrm{M}_\odot \leq M_\mathrm{Cluster} \leq 10^{14.0}\ h^{-1}\mathrm{M}_\odot$ is less than 0.005, from which can inferred that galaxy group/cluster masses lower than this cannot form BTRSs due to galaxy velocity dispersion alone. The other consideration, however, is that there are $\approx 6000$ clusters in that mass bin (Gottlöber et al., 2006) and less than half of that number in the $10^{14.0}\ h^{-1}\mathrm{M}_\odot \leq M_\mathrm{Cluster} \leq 10^{14.5}\ h^{-1}\mathrm{M}_\odot$ mass bin. The actual numbers of simulated BTRSs show a different distribution.

The particle mass resolution of the MareNostrum Universe simulation does not allow for probing of galaxies with masses lower than $1.0 \times 10^{11}\ \mathrm{M}_\odot$. One of the limitations of using FoF algorithm, which is prone to find spurious particle associations when using too few particles to resolve galaxies, is the necessity of using a large number of dark matter particles to represent a galaxy halo in the simulation. The choice of 36 dark matter particles is a compromise between sufficient galaxy mass resolution and ameliorating the problem of spurious associations.

There are virtually no clusters with a mass less than the $10^{13.5} - 10^{14.0}\ h^{-1}\mathrm{M}_\odot$ mass bin that host BTRSs. It is an expected result because the clusters' central density and kinetic energy of member galaxies are largely produced by the gravitational potential well of the host cluster. The high mass clusters do show more capacity to produce high velocity galaxies. Galaxies that are closer to the clusters' core are expected to have lower relative velocities and that would be

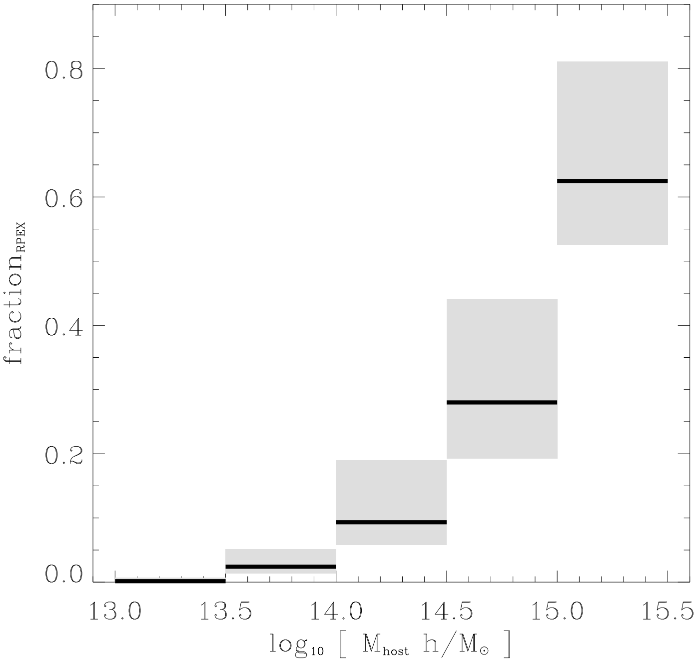

Figure 7.5: The fraction of BTRSs as a function of the mass of the host cluster. The high mass end of the histogram is limited by the highest mass clusters in the simulation. The x-axis shows mass bins of cluster dark matter halos and the y-axis shows the fraction of galaxy dark matter halos that are potential BTRSs in each cluster mass bin.

one of the reasons why the fraction of high velocity galaxies is not higher at the high mass end of the clusters.

Fig. 7.6 shows the number of simulated BTRSs as a function of host cluster mass. The x-axis represents the cluster mass bins and the y-axis, the number of potential BTRSs in each mass bin. The black solid line corresponds to the fraction of BTRSs found based on $2.4 \times 10^9 \rho_\mathrm{b}(\ \mathrm{km\,s^{-1}})^2$, and the grey area above and below the line, corresponds to the lower limit $(1.0 \times 10^9 \rho_\mathrm{b}(\ \mathrm{km\,s^{-1}})^2)$ and the upper limit $(4.1 \times 10^9 \rho_\mathrm{b}(\ \mathrm{km\,s^{-1}})^2)$ respectively. It becomes evident that the dearth of high mass clusters ($\mathrm{M_{DM}} \geq 10^{15}\ h^{-1}\mathrm{M}_\odot$), leads to the low absolute number of BTRSs in spite of their high percentage in that mass bin. The median cluster mass bin for BTRSs is $10^{14.0}\ h^{-1}\mathrm{M}_\odot - 10^{14.5}\ h^{-1}\mathrm{M}_\odot$. The (rich) clusters are usually observed to be more massive than this, whereas (poor clusters)/groups are observed as less massive. This shows that BTRSs are

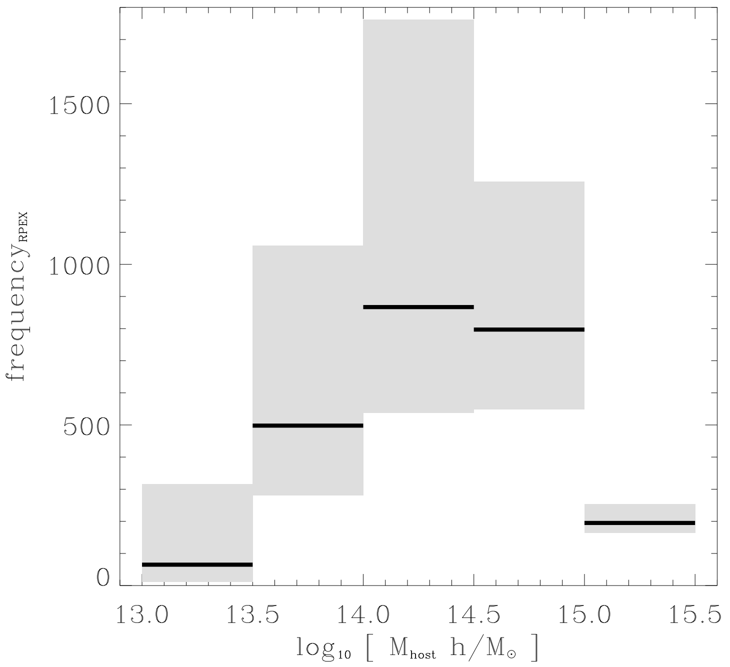

Figure 7.6: The number of BTRSs as a function of the mass of the host cluster. The high mass end of the histogram is limited by the highest mass cluster in the simulation.

equally likely to be found in clusters and in groups. Blanton et al. (2000) found similar results with slightly more than 50% of BTRSs found in (rich) clusters.

### 7.3.3 Statistics of galaxies with the critical ram pressure

The 2468 potential BTRSs with masses higher than $4.15 \times 10^{11}\ h^{-1}\mathrm{M}_\odot$, found using the analysis of Ferrari (1998) at $z = 0$, is shown in Fig. 7.5. The mean cluster mass that hosts potential BTRSs is found to lie in the $10^{14.5}\, h^{-1}\mathrm{M}_\odot$ mass bin. This means that there is equal probability of finding BTRSs in poor and in rich clusters. The number of potential BTRSs falls sharply for cluster masses lower than the $10^{13.5} - 10^{14}\ h^{-1}\mathrm{M}_\odot$ mass bin.

### 7.3.4 Distance of the BTRSs from the cluster cores

For BTRSs to be used as tracers of cluster cores, where they are likely to be shown with respect to the cluster core and whether they are only found in clusters, needs to be constrained. They have already been found to be equally likely to be in (rich) clusters (mass $\geq 10^{14.5}\ h^{-1}\mathrm{M}_\odot$) and (poor clusters)/groups (mass $\leq 10^{14.5}$ $h^{-1}\mathrm{M}_{\odot}$).

An investigation of whether BTRSs have a preferred location within their host clusters follows below. The distribution of BTRSs in the different mass bins, as a function of distance from the cluster centre, is shown in Fig. 7.7. This distribution illustrates the importance of both the velocity at which the galaxy is travelling through the ICM, and the density of the ICM. The gas density is higher closer to the cluster core, and falls off the further away one moves from the core. The circular velocity increases the further one goes from the core and flattens out at some radius due to dark matter. BTRSs preferentially lie at a radius 200 $h^{-1}$ kpc $\leq$ *Distance* $\leq$ 400 $h^{-1}$ kpc. For low mass clusters (mass $\leq 10^{14.0}$ $h^{-1}\mathrm{M}_{\odot}$) they occur within 200 $h^{-1}$ kpc the cluster core. For the highest mass clusters (mass $\geq 10^{15.0}$ $h^{-1}\mathrm{M}_{\odot}$), the fraction of galaxies that are BTRSs remains high even at the radius of 800 $h^{-1}$ kpc. The radius of 200 $h^{-1}$ kpc $\leq$ *Distance* $\leq$ 400 $h^{-1}$ kpc

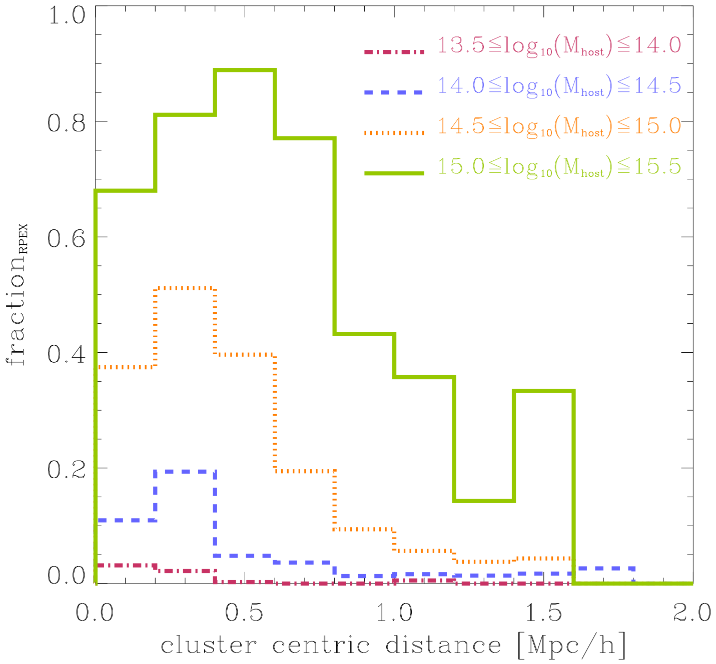

Figure 7.7: Results of the fraction of BTRSs that lay close to the core of their host clusters. The x-axis shows the distance to the cluster core and the y-axis shows the fraction of galaxies that are potential BTRSs. Each host mass bin is represented individually. Across all cluster masses, most BTRSs are found between 200 $h^{-1}$ kpc and 400 $h^{-1}$ kpc from the cluster core except for low mass 13.5 $h^{-1}\mathrm{M}_{\odot} \leq \log_{10}(M_{\mathrm{host}}) \leq 14.0$ $h^{-1}\mathrm{M}_{\odot}$ host clusters.

is assumed to be the ‘sweet spot’ where the gas density and the cumulative mass of the cluster produces enough ram pressure to bend AGN jets.

The distribution of BTRSs in clusters in the mass bins $10^{14.5}\ h^{-1}\mathrm{M}_\odot - 10^{15.5}\ h^{-1}\mathrm{M}_\odot$ (green line and orange dotted line in Fig. 7.7) shows that a BTRS that is found at a distance greater than 400 kpc from the cluster core is likely to imply a massive cluster.

## 7.4 This work

In this study the jet beam stiffness for FRGs is assumed to follow the Kaiser & Alexander (1997) (KA97) and Kaiser et al. (1997) (KDA97) mechanisms. The only difference would be that, as argued by Best (2009), for FR I galaxies, the jets have evolved enough that the ICM environment has enough density to turn the jets turbulent before they can terminate in the hotspot. Bird et al. (2008) found that the distribution of tailed radio sources in the FIRST Survey was consistent with a jet maximum lifetime of $1.75 \times 10^7$ years, with a duty cycle (i.e time between jet ejection episodes) of about $8 \times 10^8$ years. The input assumptions of KA97 and KDA97 were,

- Jet power (Q) : $5.0 \times 10^{37}\,\mathrm{W} < Q < 5.0 \times 10^{42}\,\mathrm{W}$
- Constant central density ($\rho_0$) : $7.2 \times 10^{22}\,\mathrm{kg\,m^{-3}}$
- Scale length ($a_0$) : 2.0 kpc
- Axial Ratio ($R_\mathrm{T}$) : 2.0
- Radial density power law index ($\beta$) : 1.9
- Injection index (p) : 2.14
- Adiabatic index of the ICM ($\Gamma_\mathrm{x}$) : $\frac{5}{3}$
- Adiabatic index of the Cocoon ($\Gamma_\mathrm{c}$) : $\frac{4}{3}$
- Adiabatic index of the Magnetic field energy density ($\Gamma_\mathrm{B}$) : $\frac{4}{3}$

Because there is such a variety of characteristics such as the length, bending angle, speed of the jet ejecta, luminosity and temperature of tailed radio sources, choosing average values for the different characteristics becomes challenging. The parameter space that is used in this study is about an order of magnitude in range and discusses how the different input assumptions with respect to the characteristics of the radio-loud AGNs can affect the results.

The reader is referred to Bird et al. (2008) for a full treatment of the parameter space for the above assumptions as well as the sensitivity of the results to a change in each of the inputs. The results are very robust within the range of parameters chosen and the axial ratio of the lobe has the most pronounced effect of all the inputs because it introduces projection effects. The axial ratio can change the maximum age of radio jets by more than $\sim 2$ times the fiducial lifetime. The result was sensitive to projection effects such that the median projected distance is 36% of the intrinsic length for sources that are uniformly distributed in age. Only jet lengths greater than 40 kpc are considered (at this length criterion Bird et al. (2008) found the ratio of FR Is to FR IIs to be about 1.0.)

The use of BTRSs as tracers of galaxy clusters at high redshift has been tested for $z \geq 1$ (Blanton et al., 2000). It has worked reasonably well for galaxies in $z \leq 1$ clusters but it has yet to be proven in deep ($z$ up to $> 2$) large scale radio surveys. Only $\simeq 50\%$ of galaxies in the low redshift Universe are in clusters, with the rest being in the field and in groups. This work is a first step in bringing together the numerical studies of bent AGN jets with the observational success of this method at $z \leq 1$.

For the technique to be useful at high $z$, there has to be tighter constraints on the assumptions of the interaction of AGN jets and their environments. The FIRST survey showed results where these BTRSs were found in both galaxy clusters and galaxy groups. This shows that there is a need to refine the assumptions about BTRSs capability of tracing galaxy clusters. In the next chapter there is an investigation of the use of cosmological simulation results, assuming the ansatz that BTRSs are caused by ram pressure, to refine the use of BTRSs as tracers of purely massive clusters.

## 7.5 Summary

This Chapter shows that, assuming that the bending of BTRS jets is caused by ram pressure acting on the jet due to its motion through the ICM/IGM, the fraction of large AGN jets that are likely to form BTRSs can be constrained. The accuracy of this method is subject to the ability to constrain the jet physics and the density of ICM in galaxy clusters and IGM in galaxy groups.

From the results of the MareNostrum Universe Simulation, the median cluster mass bin for formation of BTRSs is $10^{13.5} - 10^{14.0}\ h^{-1}\mathrm{M}_{\odot}$. There is a lower mass limit of $10^{13.5} - 10^{14.0}\ h^{-1}\mathrm{M}_{\odot}$ mass bin for the existence of BTRSs, beneath which there is not an appreciable number of potential BTRSs that may form. The lower mass limit corresponds to the cluster mass where both the fraction of galaxies with relative velocities greater than 1000 $\mathrm{km\,s^{-1}}$ and their number density approaches zero. This may be due to the dark matter particle mass resolution of the MareNostrum Universe simulation.

For high mass clusters, the ICM is dense up to large radii and the cumulative mass is high enough at these radii to produce the high velocities that are responsible for the high velocity tail. The results show that for low mass clusters ($M_{\mathrm{Cluster}} \leq 10^{14.5}\ h^{-1}\mathrm{M}_{\odot}$), the BTRSs should preferentially be found within 400 kpc of the group core, whereas for high mass clusters this preferred radius increases to 800 kpc. Except for the lowest mass clusters ($M_{\mathrm{Cluster}} < 10^{14}\ h^{-1}\mathrm{M}_{\odot}$), there is a probability of BTRSs being on the outskirts of the cluster or group. The conclusion is that finding a BTRS at a radius greater than 500 kpc from the cluster/group core is a better tracer of galaxy cluster than its mere presence within a cluster. The fact that the fraction of galaxies that experience enough ram pressure to induce bending rises to ≈20% in the $10^{14.5}\ h^{-1}\mathrm{M}_{\odot} - 10^{15.0}\ h^{-1}\mathrm{M}_{\odot}$ mass bin and ≈50% in the $10^{15.0}\ h^{-1}\mathrm{M}_{\odot} - 10^{15.5}\ h^{-1}\mathrm{M}_{\odot}$ mass bin, suggests that finding more than one BTRS in close proximity is also a better tracer of galaxy cluster than its mere presence within a cluster.

# Chapter 8

# Summary and future work

SMBHs, which are ubiquitous in massive galaxies, are believed to have co-evolved with their host galaxies (Silk & Rees, 1998). The AGN feedback is believed to be one of the major forces regulating galaxy evolution and star formation. Understanding AGN evolution in the early Universe will provide insights to how galaxies evolved. Knowing how the SMBH mass−bulge mass relation evolved with redshift may provide constraints on whether massive galaxies form around massive SMBHs or the massive SMBHs form at the bottom of the the gravitational potential wells of massive galaxies.

Galaxy clusters are at the junction between astrophysics and cosmology in that they form the building blocks of cosmological large scale structure and are also the environments where the most massive galaxies form. Their abundance, internal structure and distribution in the Universe carry an imprint of the initial linear density perturbations and the cosmic expansion history. These linear perturbations of the density field are assumed to be Gaussian in nature. This astounding regularity is borne out in the tight scaling relations between cluster properties and cluster mass and the universality of the cluster mass function as well as its bias when expressed as a function of the peak height ($\nu$) of the initial Gaussian perturbations of the collapsing objects of any given mass (Kravtsov & Borgani, 2012).

Galaxy clusters are important as a proof-of-concept in the hierarchical structure formation paradigm. The prediction of the $\Lambda$CDM model is that galaxy clusters cannot have formed much earlier that redshift $z \simeq 2$. Observing a cluster whose redshift is significantly higher than this prediction would decidedly disprove the $\Lambda$CDM model. Galaxy clusters are a useful probe for the Dark Energy equation of state (Weinberg et al., 2013) and General Relativity at large scales (Lombriser et al., 2009).

The observational challenge of finding clusters at high redshift using optical and NIR surveys is that the Malmquist bias is much more acute at such high $z$ and it becomes difficult to determine whether a galaxy is a member of a cluster, group or a field when all you can see are the brightest members of the clusters/groups. BTRSs can be used as tracers of galaxy clusters and groups at high redshifts because radio observations can have the sensitivity to go beyond redshift of $z = 2$. This would supplement optical and NIR galaxy cluster searches as well as SZ clusters.

## 8.1 Summary

In this work it, has been demonstrated that the SALT telescope can be used to study the velocity dispersion of massive galaxies to predict the SMBH mass via the $M_{\mathrm{BH}} - \sigma$ relation. These can then be followed up on to improve the statistics of measured SMBH masses. A sample of such spectroscopic measurements, with their high S/N ratio and good spectral resolution, is a good first step in the search for high mass SMBHs

A Bayesian framework for SMBH mass measurements was introduced and tested. JAM modelling has a successful history of use in SMBH mass measurements. The need for alternative ways to constrain the $M/L$ ratio and inclination angle for use in JAM modelling is still a problem that has to be solved, even with multi-variate Bayesian models. This consistently showed up in both the toy model and the NGC 6861 SMBH mass measurement. The method produces results that are comparable to the more state-of-the-art Schwarzschild orbit super-position method and this result, for NGC 6861, compares well with the performance of prior JAM method applications, but also provides the extra benefits of providing the full posterior distribution.

The masses of high redshift quasars were measured using the virial mass estimator method, which is based on the results of reverberation mapping. Although there is a lack of observed low mass SMBHs at high redshift, they are important for studying the evolution of the $M_{\mathrm{BH}} - \sigma$ relation with redshift. Finding more of them would improve their statistics at high redshift. Finding the $M_{\mathrm{BH}} - \sigma$ relation at high redshift also helps in the interpreting of radio jets seen at high redshift because, in the local Universe, the mass of the SMBH is related to the radio loudness of the host galaxy.

The effectiveness of using BTRSs as tracers of galaxy clusters and galaxy groups was studied using the results of the MareNostrum Universe simulation. The results showed that BTRSs are equally likely to be found in galaxy clusters and galaxy groups because, despite their high likelihood of hosting BTRSs, the massive clusters are very rare compared to galaxy groups that have very small likelihood but are much more numerous. For a determination of a cluster other subsequent criteria can be added to the basic criterion. Finding a BTRS at a radius greater than 500 kpc from the cluster/group core and finding more than one BTRS in close proximity is also a better tracer of galaxy cluster than its mere presence within a cluster.

## 8.2 Future work

Future work will be based on expanding the scope of this work. Other questions that arise in the course of this investigation will also be dealt with in the future. The pilot project of the SALT massive galaxy sample will be expanded to include Southern ETGs and Seyfert galaxies of all sizes and surface brightnesses. This will be a survey that is complementary to the Northern Hemisphere HETMGS survey. The requirement that the galaxies have a $\sigma > 250\ \mathrm{km\,s^{-1}}$ value will be relaxed so that the low mass end of the $M_{\rm BH} - \sigma$ relation may also be investigated. The result should be that the total sample will include all ETGs and Seyfert galaxies within the sample boundaries. ETGs are over-represented in high SMBH mass samples and testing the $M_{\rm BH} - \sigma$ relation in spiral galaxy bulges should improve its robustness. This project will be extended with the GANDALF software to separate stellar kinematics and gas emission. The large number of the galaxies that this survey would find means that it would be important to prioritise the galaxies with predicted low SMBH masses. These are the statistics that are required to investigate the potential curvature of $\mathrm{M}{-}\sigma$ relation.

The posterior distribution is a much richer measure of uncertainty than standard deviation. This Bayesian method will be applied to more IFU observations of galaxies to measure the SMBH masses of more galaxies, in particular those that will be in the SALT massive galaxy survey. This method will be used in observed galaxies and the results will be compared with literature values. This will incorporate the total galaxy mass as a parameter in the algorithm. Adding dark matter contribution in observed galaxies to the algorithm will allow for the use of both the total galaxy mass as a parameter and the use of multiple mass tracers in observations. The efficacy of the method will be further investigated by comparing its results to the more accurate methods such as Masers and molecular gas dynamics observed in the sub-millimeter wavelength regime. An H I survey of Southern ETGs, complementary to the proposed SALT massive galaxy survey will be done to constrain, where possible, the $M/L$ ratio in some of the ETGs to help in the application of JAM models for SMBH mass measurements.

A search for more low mass SMBHs at high redshift will be continued to improve the statistics of high redshift low mass SMBHs ($M_{\rm BH} \approx 10^6$ M$_\odot$). This will be in conjuction with a search for interacting binary SMBHs in galaxy-galaxy mergers where the the effects of the merger in the formation of QSOs and radio loud AGNs will be investigated.

It has been shown that the use of BTRSs as tracers of high redshift galaxy clusters can be refined by using the results of a cosmological simulation. Future work will use cosmological simulations with mass resolution of baryon and dark matter particles that is more than 10 times better. The high mass limit corresponds to where the most massive cluster is found in the MareNostrum simulation. The number densities of potential BTRSs cannot be compared to observations without making assumptions about the lifetimes of AGN activity and, to a lesser extent, viewing angles of galaxy jets in the Universe.

In this work, the observing angle, AGN activity life cycles and lifetimes, the average age of these massive galaxies, the volume within which they can be observed as well as jet length, jet luminosity and the observable radius of curvature are not properly constrained. Morsony et al. (2013) states that at an observing angle of 60° the radius of curvature is perceived as half the actual radius of curvature. Since radius of curvature is stated in relation to the jet radius, the observing angle range for which the results of the BTRS study remain valid has to be constrained. The role of cluster-cluster mergers and galaxy infall onto clusters will be investigated together with the role of gas motions in filaments in creating high relative velocity between galaxies and the environment. Addressing these challenges forms part of future work.

The LOFAR telescope observes the low frequency emission from the Universe up to $z \geq 2$ and the Jansky very large array (JVLA) will serve a similar purpose at the gigaHertz regime. The SKA pathfinders, MeerKAT and ASKAP, when fully operational, will extend these radio studies through better survey speed and sensitivity. The low frequency studies will reveal old electron populations in the cores of galaxy clusters at $z \simeq 2$ and in AGN jets, whereas gigahertz frequencies will map the interactions of jets with ICM plasma and use detailed Faraday rotation observations to reveal the magnetic field structure of the plasma. The low frequency luminosity has been found to correlate with SMBH mass and, in this work, it has been found that a bigger sample of SMBH mass measurements of low radio frequency galaxies is needed to constrain the correlation.

Studying relativistic jets in AGNs is one of the key science goals of the SKA. This field is still subject to active research and has many open questions with respect to the detailed physics of AGN jets. The resolution and sensitivity of the SKA will facilitate the study of AGN jets in great detail up to the epoch or re-ionisation. Agudo et al. (2015) lists some of the outstanding research questions as

- The particle composition of the ejecta plasma at different scales and its evolution along the jet.
- The influence of magnetic fields on jet formation, collimation and how it is maintained over a distance of hundreds of kpc.
- The influence of the jet-IGM feedback on group/cluster evolution.
- The 3-dimensional distribution of jet flow parameters like velocity, magnetic structure and emissivity.
- Why are jets produced efficiently in some cases and not others, and how does blackhole mass and accretion mode relate to jet power?

Understanding the physical nature of these jets will allow the use of BTRSs not only as tracers of clusters and groups at high $z$ but as probes of the ICM density and magnetic structure in the host clusters. The optical and NIR methods of SMBH mass measurement methods at high redshift are essential to probing the last point. The multiwavelength approach is the only viable one for these fundamental jet physics studies.

The increased sensitivity and angular resolution of sub-millimeter ALMA telescope has already extended the distance to galaxies for which the blackhole mass can be measured via molecular gas dynamics in the cores of ETGs. This will increase the statistical sample size of measured blackhole masses and potentially allow for more SMBH masses measured via two or more methods. The next generation of optical and NIR telescopes like the TMT, OWL and E-ELT will achieve the same objective in the optical and NIR regimes. The ability to cross-reference SMBH masses obtained via different methods will improve the modeling and constrain uncertainties in the assumptions used in the models.

The ansatz that BTRSs are caused by ram pressure experienced by AGN jets against the IGM will be better constrained when tested against observations of the next generation radio telescopes, particularly the SKA. Detailed observations of the jet plasma as well as the IGM itself will be able to measure the particle content, flow velocity, jet age and magnetic field structure and strength with enough resolution and for a big enough sample of AGN jets to allow better modelling of the plasma physics of jets and likely be able to pinpoint where and why jets bend. The study pursued in this work will then have to be able to allow for more accurate physics in the future as well as the separation between different types of radio galaxies. The old population of particles in radio lobes of AGN jets will help in the study of the impact of the radio jets on the environment. This includes the degree to which the jets enrich the IGM with metals, the role of the jets in the cooling flows of clusters/groups and the role of the shocks, generated by the jets, in the heating of the IGM.

The use of BTRSs as tracers of galaxy clusters at high redshift has been tested for $z \geq 1$. It has worked reasonably well for galaxies in $z \leq 1$ clusters but it has yet to be proven in deep ($z$ up to $> 2$) large scale radio surveys . Only $\simeq 50\%$ of galaxies in the low redshift Universe are in clusters, with the rest being in the field and in groups. This work is a first step in bringing together the numerical studies of bent AGN jets with the observational success of this method at $z \leq 1$.

The highest redshift quasars that are found in the SDSS survey is $z > 6$. The search for galaxy clusters is not supposed to extend much beyond $z = 2$. According to the hierarchical structure formation paradigm, the earliest they could have formed is $z \simeq 2$. Before then, they had not virialised and are proto-clusters. In this work, it is shown that SMBH masses can be measured up to $z \simeq 3$ using the virial mass estimator method which has a scatter of 0.5 dex. Blackhole mass and accretion rate are the primary driving forces in the study of AGN jet formation. The ability to measure SMBH masses at high $z$ allows the comparison of jet formation at high $z$ with jet formation in the local Universe. This is important when testing the ansatz that jet formation does not change with redshift.

Determining the particle content of the jet ejecta, allows for its use in probing the density of the ICM. At high $z$, this would be an excellent method to determine cluster density. Modeling interactions between radio jets and the environments requires a constraint on the particle content of the jets or the gas density of the environment. It may be possible, with the next generation of telescopes, to constrain gas density which would allow the use of BTRSs to measure the particle content of jet ejecta.

# Bibliography

Abazajian K. N., Adelman-McCarthy J. K., Agüeros M. A., Allam S. S., Allende Prieto C., An D., Anderson K. S. J., Anderson S. F., Annis J., Bahcall N. A., et al. 2009, ApJS, 182, 543

Agudo I., Boettcher M., Falcke H. D. E., Georganopoulos M., Ghisellini G., Giovannini G., Giroletti M., Gurvits L., Gómez J. L., Laing R., Lister D., Stawarz L., Vlahakis N., Wardle J., 2015, Advancing Astrophysics with the Square Kilometre Array (AASKA14), p. 93

Akritas M. G., Bershady M. A., 1996, ApJ, 470, 706

Alberdi A., Marcaide J. M., Marscher A. P., Zhang Y. F., Elosegui P., Gomez J. L., Shaffer D. B., 1993, ApJ, 402, 160

Allen S. W., Evrard A. E., Mantz A. B., 2011, ARA&A, 49, 409

Allen S. W., Schmidt R. W., Ebeling H., Fabian A. C., van Speybroeck L., 2004, MNRAS, 353, 457

Amarantidis S., Afonso J., Messias H., Henriques B., Griffin A., Lacey C., Lagos C. d. P., Gonzalez-Perez V., Dubois Y., Volonteri M., Matute I., Pappalardo C., Qin Y., Chary R.-R., Norris R. P., 2019, MNRAS, 485, 2694

Antognini J., Bird J., Martini P., 2012, ApJ, 756, 116

Antonucci R., 1993, Annual Review of Astronomy and Astrophysics, 31, 473

Arp H., 1966, ApJS, 14, 1

Arp H. C., Madore B., 1987, A catalogue of southern peculiar galaxies and associations

Arshakian T. G., Longair M. S., 2004, MNRAS, 351, 727

Ascaso B., Wittman D., Dawson W., 2014, MNRAS, 439, 1980

Barnabè M., Auger M. W., Treu T., Koopmans L. V. E., Bolton A. S., Czoske O., Gavazzi R., 2010, MNRAS, 406, 2339

Barnabè M., Czoske O., Koopmans L. V. E., Treu T., Bolton A. S., Gavazzi R., 2009, MNRAS, 399, 21

Bastian N., Covey K. R., Meyer M. R., 2010, ARA&A, 48, 339

Baum S. A., Heckman T., 1989, ApJ, 336, 702

Becker R. H., White R. L., Helfand D. J., 1995, ApJ, 450, 559

Begelman M. C., Rees M. J., Blandford R. D., 1979, Nature, 279, 770

Beifiori A., Sarzi M., Corsini E. M., Dalla Bontà E., Pizzella A., Coccato L., Bertola F., 2009, ApJ, 692, 856

Bell E. F., McIntosh D. H., Katz N., Weinberg M. D., 2003, ApJS, 149, 289

Bender R., 1990, A&A, 229, 441

Bender R., Saglia R. P., Gerhard O. E., 1994, MNRAS, 269, 785

Bennett C. L., 2003, ApJS, 148, 1

Bentz M. C., Katz S., 2015, PASP, 127, 67

Best P. N., 2009, Astronomische Nachrichten, 330, 184

Best P. N., Kauffmann G., Heckman T. M., Brinchmann J., Charlot S., Ivezić Ž., White S. D. M., 2005, MNRAS, 362, 25

Best P. N., von der Linden A., Kauffmann G., Heckman T. M., Kaiser C. R., 2007, MNRAS, 379, 894

Binney J., Tremaine S., 2008, Galactic Dynamics: Second Edition. Princeton University Press

Bird J., Martini P., Kaiser C., 2008, ApJ, 676, 147

Blandford R., Meier D., Readhead A., 2019, Annual Review of Astronomy and Astrophysics, 57, 467

Blandford R. D., McKee C. F., 1982, ApJ, 255, 419

Blanton E. L., Gregg M. D., Helfand D. J., Becker R. H., Leighly K. M., 2001, AJ, 121, 2915

Blanton E. L., Gregg M. D., Helfand D. J., Becker R. H., White R. L., 2000, ApJ, 531, 118

Blanton E. L., Gregg M. D., Helfand D. J., Becker R. H., White R. L., 2003, AJ, 125, 1635

Blanton M. R., Moustakas J., 2009, Annual Review of Astronomy and Astrophysics, 47, 159

Bonnet H., Conzelmann R., Delabre B., Donaldson R., Fedrigo E., Hubin N. N., Kissler-Patig M., Lizon J.-L., Paufique J., Rossi S., Stroebele S., Tordo S., 2004, in Bonaccini Calia D., Ellerbroek B. L., Ragazzoni R., eds, Advancements in Adaptive Optics Vol. 5490 of Proc. SPIE, First light of SINFONI AO-module at VLT. pp 130–138

Bridges M., Feroz F., Hobson M. P., Lasenby A. N., 2009, MNRAS, 400, 1075

Burns J. O., 1981, MNRAS, 195, 523

Burns J. O., Owen F. N., 1980, AJ, 85, 204

Campbell L. A., Lucey J. R., Colless M., Jones D. H., Springob C. M., Magoulas C., Proctor R. N., Mould J. R., Read M. A., Brough S., Jarrett T., Merson A. I., Lah P., Beutler F., Cluver M. E., Parker Q. A., 2014, MNRAS, 443, 1231

Cappellari M., 2002, MNRAS, 333, 400

Cappellari M., 2008, MNRAS, 390, 71

Cappellari M., Copin Y., 2003, MNRAS, 342, 345

Cappellari M., Emsellem E., 2004, PASP, 116, 138

Cappellari M., Emsellem E., Bacon R., Bureau M., Davies R. L., de Zeeuw P. T., Falcón-Barroso J., Krajnović D., Kuntschner H., McDermid R. M., Peletier R. F., Sarzi M., van den Bosch R. C. E., van de Ven G., 2007, MNRAS, 379, 418

Cappellari M., McDermid R. M., Bacon R., Davies R. L., de Zeeuw P. T., Emsellem E., Falcón-Barroso J., Krajnović D., Kuntschner H., Peletier R. F., Sarzi M., van den Bosch R. C. E., van de Ven G., 2010, in Debattista V. P., Popescu C. C., eds, American Institute of Physics Conference Series Vol. 1240 of American Institute of Physics Conference Series, Testing Mass Determinations of Supermassive Black Holes via Stellar Kinematics. pp 211–214

Cappellari M., Scott N., Alatalo K., Blitz L., Bois M., Bournaud F., Bureau M., Crocker A. F., Duc P.-A., Emsellem E., Khochfar S., Krajnović D., Weijmans A.-M., Young L. M., 2013, MNRAS, 432, 1709

Combes F., 2017, Frontiers in Astronomy and Space Sciences, 4, 10

Conroy C., van Dokkum P. G., 2012, ApJ, 760, 71

Courteau S., Cappellari M., de Jong R. S., Dutton A. A., Emsellem E., Hoekstra H., Koopmans L. V. E., Mamon G. A., Maraston C., Treu T., Widrow L. M., 2014, Reviews of Modern Physics, 86, 47

Czoske O., Barnabè M., Koopmans L. V. E., Treu T., Bolton A. S., 2008, MNRAS, 384, 987

Davé R., Cen R., Ostriker J. P., Bryan G. L., Hernquist L., Katz N., Weinberg D. H., Norman M. L., O'Shea B., 2001, ApJ, 552, 473

Davis S. W., Tchekhovskoy A., 2020, Annual Review of Astronomy and Astrophysics, 58, null

Davis T. A., Bureau M., Cappellari M., Sarzi M., Blitz L., 2013, Nature, 494, 328

de Vaucouleurs G., 1948, Annales d'Astrophysique, 11, 247

de Vaucouleurs G., 1959, Handbuch der Physik, 53, 275

de Vaucouleurs G., de Vaucouleurs A., Corwin Jr. H. G., Buta R. J., Paturel G., Fouqué P., 1991, Third Reference Catalogue of Bright Galaxies. Volume I: Explanations and references. Volume II: Data for galaxies between $0^h$ and $12^h$. Volume III: Data for galaxies between $12^h$ and $24^h$.

De Young D. S., 1991, ApJ, 371, 69

Dehghan S., Johnston-Hollitt M., Franzen T. M. O., Norris R. P., Miller N. A., 2014, AJ, 148, 75

Dehghan S., Johnston-Hollitt M., Mao M., Norris R. P., Miller N. A., Huynh M., 2011, Journal of Astrophysics and Astronomy, 32, 491

Diakogiannis F. I., Lewis G. F., Ibata R. A., 2014a, MNRAS, 443, 598

Diakogiannis F. I., Lewis G. F., Ibata R. A., 2014b, MNRAS, 443, 610

Doe S. M., Ledlow M. J., Burns J. O., White R. A., 1995, AJ, 110, 46

Dongarra J., Sullivan F., 2000, Computing in Science and Engineering, 2, 22

Drehmer D. A., Storchi-Bergmann T., Ferrari F., Cappellari M., Riffel R. A., 2015, MNRAS, 450, 128

Dressler A., 1989, in Osterbrock D. E., Miller J. S., eds, Active Galactic Nuclei Vol. 134 of IAU Symposium, Observational Evidence for Supermassive Black Holes. p. 217

Dressler A., Richstone D. O., 1988, ApJ, 324, 701

Edge D. O., Shakeshaft J. R., McAdam W. B., Baldwin J. E., Archer S., 1959, MmRAS, 68, 37

Edwards L. O. V., Fadda D., Frayer D. T., 2010, ApJ, 724, L143

Eilek J. A., Burns J. O., O'Dea C. P., Owen F. N., 1984, ApJ, 278, 37

Einasto J., Klypin A. A., Saar E., Shandarin S. F., 1984, MNRAS, 206, 529

Eisenhauer F., Abuter R., Bickert K., Biancat-Marchet F., Bonnet H., Brynnel J., Conzelmann R. D., Delabre B., Donaldson R., Farinato J., Fedrigo E., Genzel R., Tecza M., Thatte N. A., Weisz H., 2003, in Iye M., Moorwood A. F. M., eds, Instrument Design and Performance for Optical/Infrared Ground-based Telescopes Vol. 4841 of Proc. SPIE, SINFONI - Integral field spectroscopy at 50 milli-arcsecond resolution with the ESO VLT. pp 1548–1561

Ekers R. D., 1978, A&A, 69, 253

Elmegreen D. M., Elmegreen B. G., 1982, MNRAS, 201, 1021

Emsellem E., Cappellari M., Krajnović D., van de Ven G., Bacon R., Bureau M., Davies R. L., de Zeeuw P. T., Falcón-Barroso J., Kuntschner H., McDermid R., Peletier R. F., Sarzi M., 2007, MNRAS, 379, 401

Emsellem E., Monnet G., Bacon R., 1994, A&A, 285

Emsellem E., Monnet G., Bacon R., Nieto J.-L., 1994, A&A, 285

ESO CPL Development Team, 2015, EsoRex: ESO Recipe Execution Tool

Faber S. M., Willmer C. N. A., Wolf C., Koo D. C., Weiner B. J., Newman J. A., Im M., Coil A. L., Conroy C., Cooper M. C., Davis M., Finkbeiner D. P., Simard L., Szalay A. S., Vogt N. P., Yan R., 2007, ApJ, 665, 265

Fabian A., 2012, Annual Review of Astronomy and Astrophysics, 50, 455

Fabian A. C., 1999, MNRAS, 308, L39

Falcón-Barroso J., Sánchez-Blázquez P., Vazdekis A., Ricciardelli E., Cardiel N., Cenarro A. J., Gorgas J., Peletier R. F., 2011, A&A, 532, A95

Fan X., Strauss M. A., Richards G. T., Newman J. A., Doi M., Fukugita M., Hennessy G. S., Hindsley R. B., Ivezić Ž., Knapp G. R., McKay T. A., Munn J. A., Pier J. R., Szalay A. S., York D. G., 2001, AJ, 121, 31

Fanaroff B. L., Riley J. M., 1974, MNRAS, 167, 31P

Feroz F., Gair J. R., Hobson M. P., Porter E. K., 2009, Classical and Quantum Gravity, 26, 215003

Feroz F., Hobson M. P., 2008, MNRAS, 384, 449

Feroz F., Hobson M. P., Bridges M., 2009, MNRAS, 398, 1601

Ferrarese L., Merritt D., 2000, ApJ, 539, L9

Ferrarese L., Pogge R. W., Peterson B. M., Merritt D., Wandel A., Joseph C. L., 2001, ApJ, 555, L79

Ferrari A., 1998, ARA&A, 36, 539

Fisher D. B., Drory N., 2008, AJ, 136, 773

Foltz C. B., Chaffee Jr. F. H., Hewett P. C., MacAlpine G. M., Turnshek D. A., Weymann R. J., Anderson S. F., 1987, AJ, 94, 1423

Fontanot F., Monaco P., Shankar F., 2015, MNRAS, 453, 4112

Freeland E., Cardoso R. F., Wilcots E., 2008, ApJ, 685, 858

Freeland E., Wilcots E., 2011, ApJ, 738, 145

Gebhardt K., Bender R., Bower G., Dressler A., Faber S. M., Filippenko A. V., Green R., Grillmair C., Ho L. C., Kormendy J., Lauer T. R., Magorrian J., Pinkney J., Richstone D., Tremaine S., 2000, ApJ, 539, L13

Gebhardt K., Richstone D., Ajhar E. A., Lauer T. R., Byun Y.-I., Kormendy J., Dressler A., Faber S. M., Grillmair C., Tremaine S., 1996, AJ, 112, 105

Gebhardt K., Thomas J., 2009, ApJ, 700, 1690

Genzel R., Eisenhauer F., Gillessen S., 2010, Reviews of Modern Physics, 82, 3121

Ghez A. M., Salim S., Weinberg N. N., Lu J. R., Do T., Dunn J. K., Matthews K., Morris M. R., Yelda S., Becklin E. E., Kremenek T., Milosavljevic M., Naiman J., 2008, ApJ, 689, 1044

Ghisellini G., Celotti A., Tavecchio F., Haardt F., Sbarrato T., 2014, MNRAS, 438, 2694

Gottlöber S., Yepes G., Khalatyan A., Sevilla R., Turchaninov V., 2006, in Manoz C., Yepes G., eds, The Dark Side of the Universe Vol. 878 of American Institute of Physics Conference Series, Dark and baryonic matter in the MareNostrum Universe. pp 3–9

Graham A. W., 2007, MNRAS, 379, 711

Graham A. W., 2016, Galactic Bulges, 418, 263

Graham A. W., Scott N., 2015, ApJ, 798, 54

Graham A. W., Soria R., 2019, MNRAS, 484, 794

Graham A. W., Soria R., Davis B. L., 2019, MNRAS, 484, 814

Graves G. J., Faber S. M., 2010, ApJ, 717, 803

Gültekin K., Richstone D. O., Gebhardt K., Lauer T. R., Tremaine S., Aller M. C., Bender R., Dressler A., Faber S. M., Filippenko A. V., Green R., Ho L. C., Kormendy J., Magorrian J., Pinkney J., Siopis C., 2009, ApJ, 698, 198

Gustafsson B., Edvardsson B., Eriksson K., Jørgensen U. G., Nordlund Å., Plez B., 2008, A&A, 486, 951

Hardcastle M. J., 2006, MNRAS, 366, 1465

Hardcastle M. J., Alexander P., Pooley G. G., Riley J. M., 1998, MNRAS, 296, 445

Harms R. J., Ford H. C., Tsvetanov Z. I., Hartig G. F., Dressel L. L., Kriss G. A., Bohlin R., Davidsen A. F., Margon B., Kochhar A. K., 1994, ApJ, 435, L35

Harrison I., Hotchkiss S., 2013, , 2013, 022

Heckman T. M., 1983, ApJ, 273, 505

Heckman T. M., Best P. N., 2014, Annual Review of Astronomy and Astrophysics, 52, 589

Hernquist L., 1990, ApJ, 356, 359

Hewett P. C., Foltz C. B., Chaffee F. H., 2001, AJ, 122, 518

Higdon J. L., Higdon S. J. U., 2010, in Smith B., Higdon J., Higdon S., Bastian N., eds, Galaxy Wars: Stellar Populations and Star Formation in Interacting Galaxies Vol. 423 of Astronomical Society of the Pacific Conference Series, Why Are Ring Galaxies Interesting?. p. 12

Higdon J. L., Higdon S. J. U., Rand R. J., 2011, ApJ, 739, 97

Hill G. J., Rawlings S., 2003, New Astronomy Reviews, 47, 373

Hill J. M., Longair M. S., 1971, MNRAS, 154, 125

Ho L. C., Filippenko A. V., Sargent W. L. W., 1997, ApJS, 112, 315

Hu J., 2008, MNRAS, 386, 2242

Huarte Espinosa M., Mendoza S., 2007, in Revista Mexicana de Astronomia y Astrofisica, vol. 27 Vol. 27 of Revista Mexicana de Astronomia y Astrofisica Conference Series, Simple Scaling Laws for Astrophysical Jets. p. 236

Hubble E., Kirshner R., Carroll S., 2013, The Realm of the Nebulae. Mrs. Hepsa Ely Silliman memorial lectures, Yale University Press

Hubble E. P., 1926, ApJ, 64

Huchra J. P., Geller M. J., 1982, ApJ, 257, 423

Into T., Portinari L., 2013, MNRAS, 430, 2715

Jaffe W., 1983, MNRAS, 202, 995

Jahnke K., Macciò A. V., 2011, ApJ, 734, 92

Jarrett T. H., Chester T., Cutri R., Schneider S., Skrutskie M., Huchra J. P., 2000, AJ, 119, 2498

Jeans J. H., 1922, MNRAS, 82, 122

Jetha N. N., Hardcastle M. J., Sakelliou I., 2006, MNRAS, 368, 609

Jiang G., Kochanek C. S., 2007, ApJ, 671, 1568

Jones T. W., Owen F. N., 1979, ApJ, 234, 818

Kaiser C. R., Alexander P., 1997, MNRAS, 286, 215

Kaiser C. R., Dennett-Thorpe J., Alexander P., 1997, MNRAS, 292, 723

Kaspi S., Smith P. S., Netzer H., Maoz D., Jannuzi B. T., Giveon U., 2000, ApJ, 533, 631

Kauffmann G., Heckman T. M., Tremonti C., Brinchmann J., Charlot S., White S. D. M., Ridgway S. E., Brinkmann J., Fukugita M., Hall P. B., Ivezić Ž., Richards G. T., Schneider D. P., 2003, MNRAS, 346, 1055

Kerr R. P., 1963, Physical Review Letters, 11, 237

Kharb P., Stanley E., Lister M., Marshall H., O'Dea C., Baum S., 2015, IAU Symp., 313, 211

King A., Pounds K., 2015, Annual Review of Astronomy and Astrophysics, 53, 115

King I. R., 1966, AJ, 71, 64

Klypin A., Gottlöber S., Kravtsov A. V., Khokhlov A. M., 1999, ApJ, 516, 530

Koester B. P., McKay T. A., Annis J. e. a., 2007, ApJ, 660, 239

Koliopanos F., Ciambur B. C., Graham A. W., Webb N. A., Coriat M., Mutlu-Pakdil B., Davis B. L., Godet O., Barret D., Seigar M. S., 2017, A&A, 601, A20

Koopmans L. V. E., 2006, in Mamon G. A., Combes F., Deffayet C., Fort B., eds, EAS Publications Series Vol. 20 of EAS Publications Series, Gravitational Lensing and Stellar Dynamics. pp 161–166

Kormendy J., 1988a, ApJ, 335, 40

Kormendy J., 1988b, ApJ, 325, 128

Kormendy J., Djorgovski S., 1989, ARA&A, 27, 235

Kormendy J., Ho L. C., 2013, ARA&A, 51, 511

Kormendy J., Kennicutt Jr. R. C., 2004, ARA&A, 42, 603

Kormendy J., Richstone D., 1995, ARA&A, 33, 581

Krajnović D., McDermid R. M., Cappellari M., Davies R. L., 2009, MNRAS, 399, 1839

Kravtsov A. V., Borgani S., 2012, ARA&A, 50, 353

Krist J. E., Hook R. N., Stoehr F., 2011, in Optical Modeling and Performance Predictions V Vol. 8127 of Proc. SPIE, 20 years of Hubble Space Telescope optical modeling using Tiny Tim. p. 81270J

Krolik J. H., 2001, ApJ, 551, 72

Lacy M., Riley J. M., Waldram E. M., McMahon R. G., Warner P. J., 1995, MNRAS, 276, 614

Lalovic A., 2010, Serbian Astronomical Journal, 180, 57

Lauer T. R., Faber S. M., Richstone D., Gebhardt K., Tremaine S., Postman M., Dressler A., Aller M. C., Filippenko A. V., Green R., Ho L. C., Kormendy J., Magorrian J., Pinkney J., 2007, ApJ, 662, 808

Ledlow M. J., Owen F. N., 1995, AJ, 109, 853

Lin Y.-T., Shen Y., Strauss M. A., Richards G. T., Lunnan R., 2010, ApJ, 723, 1119

Lochner M., Natarajan I., Zwart J. T. L., Smirnov O., Bassett B. A., Oozeer N., Kunz M., 2015, MNRAS, 450, 1308

Lombriser L., Hu W., Fang W., Seljak U., 2009, Phys. Rev. D, 80, 063536

Lynden-Bell D., 1969, Nature, 223, 690

Lynden-Bell D., 1978, Phys. Scr, 17, 185

Lynds R., Toomre A., 1976, ApJ, 209, 382

MacDonald G. H., Kenderdine S., Neville A. C., 1968, MNRAS, 138, 259

Machacek M. E., O'Sullivan E., Randall S. W., Jones C., Forman W. R., 2010, ApJ, 711, 1316

Mackay C. D., 1971, MNRAS, 154, 209

Magorrian J., Tremaine S., Richstone D., Bender R., Bower G., Dressler A., Faber S. M., Gebhardt K., Green R., Grillmair C., Kormendy J., Lauer T., 1998, AJ, 115, 2285

Makarov D., Prugniel P., Terekhova N., Courtois H., Vauglin I., 2014, A&A, 570, A13

Marconi A., Hunt L. K., 2003, ApJ, 589, L21

Matthews T. A., Sandage A. R., 1963, ApJ, 138, 30

McGilchrist M. M., Baldwin J. E., Riley J. M., Titterington D. J., Waldram E. M., Warner P. J., 1990, MNRAS, 246, 110

McLure R. J., 2003, New Astronomy Reviews, 47, 173

McLure R. J., Dunlop J. S., 2003, in Bender R., Renzini A., eds, The Mass of Galaxies at Low and High Redshift On the Black Hole – Bulge Mass Relation in Active and Inactive Galaxies. p. 26

McLure R. J., Dunlop J. S., 2004, MNRAS, 352, 1390

McLure R. J., Jarvis M. J., 2002, MNRAS, 337, 109

McLure R. J., Jarvis M. J., 2004, MNRAS, 353, L45

McLure R. J., Jarvis M. J., Targett T. A., Dunlop J. S., Best P. N., 2006, MNRAS, 368, 1395

McLure R. J., Willott C. J., Jarvis M. J., Rawlings S., Hill G. J., Mitchell E., Dunlop J. S., Wold M., 2004, MNRAS, 351, 347

McMaster M., et al. 2008, Wide Field and Planetary Camera 2 Instrument Handbook v. 10.0

Mezcua M., Civano F., Fabbiano G., Miyaji T., Marchesi S., 2016, ApJ, 817, 20

Mguda Z., Faltenbacher A., Heyden K. v. d., Gottlöber S., Cress C., Vaisanen P., Yepes G., 2015, MNRAS, 446, 3310

Michie R. W., Bodenheimer P. H., 1963, MNRAS, 126, 269

Miley G. K., Perola G. C., van der Kruit P. C., van der Laan H., 1972, Nature, 237, 269

Miller N. A., Bonzini M., Fomalont E. B., Kellermann K. I., Mainieri V., Padovani P., Rosati P., Tozzi P., Vattakunnel S., 2013, ApJS, 205, 13

Miyoshi M., Moran J., Herrnstein J., Greenhill L., Nakai N., Diamond P., Inoue M., 1995, Nature, 373, 127

Morsony B. J., Miller J. J., Heinz S., Freeland E., Wilcots E., Brüggen M., Ruszkowski M., 2013, MNRAS, 431, 781

Mulchaey J. S., 2000, Annual Review of Astronomy and Astrophysics, 38, 289

Munari U., Sordo R., Castelli F., Zwitter T., 2005, A&A, 442, 1127

Naab T., Ostriker J. P., 2017, Annual Review of Astronomy and Astrophysics, 55, 59

Natarajan I., Paragi Z., Zwart J., Perkins S., Smirnov O., van der Heyden K., 2017, MNRAS, 464, 4306

Navarro J. F., Frenk C. S., White S. D. M., 1997, ApJ, 490, 493

Netzer H., 2015, Annual Review of Astronomy and Astrophysics, 53, 365

O'Dea C. P., 1985, ApJ, 295, 80

O'Dea C. P., Daly R. A., Kharb P., Freeman K. A., Baum S. A., 2009, A&A, 494, 471

O'Dea C. P., Owen F. N., 1985, AJ, 90, 954

O'Dea C. P., Owen F. N., 1986, ApJ, 301, 841

O'Dea C. P., Owen F. N., 1987, ApJ, 316, 95

O'Donoghue A. A., Eilek J. A., Owen F. N., 1993, ApJ, 408, 428

Oke J. B., Schmidt M., 1963, AJ, 68, 288

Onken C. A., Ferrarese L., Merritt D., Peterson B. M., Pogge R. W., Vestergaard M., Wandel A., 2004, ApJ, 615, 645

Owen F. N., Hardee P. E., Cornwell T. J., 1989, ApJ, 340, 698

Owen F. N., O'Dea C. P., Inoue M., Eilek J. A., 1985, ApJ, 294, L85

Owen F. N., Rudnick L., 1976, ApJ, 205, L1

Oyaizu H., Lima M., Cunha C. E., Lin H., Frieman J., Sheldon E. S., 2008, ApJ, 674, 768

Paliya V. S., Sahayanathan S., Parker M. L., Fabian A. C., Stalin C. S., Anjum A., Pand ey S. B., 2014, ApJ, 789, 143

Park S., Sohn B. W., Yi S. K., 2013, A&A, 560, A80

Paturel G., Petit C., Prugniel P., Theureau G., Rousseau J., Brouty M., Dubois P., Cambrésy L., 2003, A&A, 412, 45

Pearson T. J., Kus A. J., 1978, MNRAS, 182, 273

Peterson B. M., 2001, in Aretxaga I., Kunth D., Mújica R., eds, Advanced Lectures on the Starburst-AGN Variability of Active Galactic Nuclei. p. 3

Peterson B. M., Ferrarese L., Gilbert K. M., Kaspi S., Malkan M. A., Maoz D., Merritt D., Netzer H., Onken C. A., Pogge R. W., Vestergaard M., Wandel A., 2004, ApJ, 613, 682

Peterson B. M., Horne K., 2004, Astronomische Nachrichten, 325, 248

Peterson B. M., Wandel A., 2000, ApJ, 540, L13

Pisano D. J., Wakker B. P., Wilcots E. M., Fabian D., 2004, AJ, 127, 199

Planck Collaboration Ade P. A. R., Aghanim N., Armitage-Caplan C., Arnaud M., Ashdown M., Atrio-Barandela F., Aumont J., Baccigalupi C., Banday A. J., et al. 2013, ArXiv e-prints

Poci A., Cappellari M., McDermid R. M., 2017, MNRAS, 467, 1397

Portinari L., Into T., 2011, in Kerschbaum F., Lebzelter T., Wing R. F., eds, Why Galaxies Care about AGB Stars II: Shining Examples and Common Inhabitants Vol. 445 of Astronomical Society of the Pacific Conference Series, The Role of the TP-AGB Phase in Color - M/L Relations. p. 403

Prandoni I., Seymour N., 2015, in Advancing Astrophysics with the Square Kilometre Array (AASKA14) Revealing the Physics and Evolution of Galaxies and Galaxy Clusters with SKA Continuum Surveys. p. 67

Press W. H., Davis M., 1982, ApJ, 259, 449

Proctor D. D., 2006, ApJS, 165, 95

Prugniel P., Soubiran C., 2001, A&A, 369, 1048

Ramsey L. W., Adams M. T., Barnes T. G., Booth J. A., Cornell M. E., Fowler J. R., Gaffney N. I., Glaspey J. W., Good J. M., Hill G. J., Kelton P. W., Krabbendam V. L., Long L., MacQueen P. J., Ray F. B., Ricklefs R. L., Sage J., Sebring T. A., Spiesman W. J., Steiner M., 1998, in Stepp L. M., ed., Advanced Technology Optical/IR Telescopes VI Vol. 3352 of Proc. SPIE, Early performance and present status of the Hobby-Eberly Telescope. pp 34–42

Reber G., 1944, ApJ, 100, 279

Rees M. J., 1984, ARA&A, 22, 471

Richards G. T., Kruczek N. E., Gallagher S. C., Hall P. B., Hewett P. C., Leighly K. M., Deo R. P., Kratzer R. M., Shen Y., 2011, AJ, 141, 167

Rousselot P., Lidman C., Cuby J.-G., Moreels G., Monnet G., 2000, A&A, 354, 1134

Rudnick L., Owen F. N., 1976, ApJ, 203, L107

Rusli S. P., Thomas J., Saglia R. P., Fabricius M., Erwin P., Bender R., Nowak N., Lee C. H., Riffeser A., Sharp R., 2013, AJ, 146, 45

Ryle M., Windram M. D., 1968, MNRAS, 138, 1

Sakelliou I., Merrifield M. R., 2000, MNRAS, 311, 649

Sánchez-Blázquez P., Peletier R. F., Jiménez-Vicente J., Cardiel N., Cenarro A. J., Falcón-Barroso J., Gorgas J., Selam S., Vazdekis A., 2006, MNRAS, 371, 703

Sandage A., Sandage M., Kristian J., 1975, Galaxies and the Universe

Sargent W. L. W., Young P. J., Lynds C. R., Boksenberg A., Shortridge K., Hartwick F. D. A., 1978, ApJ, 221, 731

Schilizzi R. T., Ekers R. D., 1975, A&A, 40, 221

Schmidt M., Green R. F., 1983, ApJ, 269, 352

Schramm M., Silverman J. D., 2013, ApJ, 767, 13

Schulze A., Wisotzki L., 2011, A&A, 535, A87

Schutte Z., Reines A. E., Greene J. E., 2019, ApJ, 887, 245

Schwarzschild K., 1916, Abh. Konigl. Preuss. Akad. Wissenschaften Jahre 1906,92, Berlin,1907, 1916

Schwarzschild M., 1979, ApJ, 232, 236

Serra P., Oosterloo T., Morganti R., Alatalo K., Blitz L., Bois M., Bournaud F., Bureau M., Cappellari M., Crocker A. F., Davies R. L., Sarzi M., Scott N., Trager S. C., Weijmans A.-M., Young L. M., 2012, MNRAS, 422, 1835

Sersic J. L., 1968, Atlas de galaxias australes

Sexton R. O., Canalizo G., Hiner K. D., Komossa S., Woo J.-H., Treister E., Hiner Dimassimo S. L., 2019, ApJ, 878, 101

Seyfert C. K., 1943, ApJ, 97, 28

Shankar F., 2009, New Astronomy Reviews, 53, 57

Shen Y., Greene J. E., Ho L. C., Brand t W. N., Denney K. D., Horne K., Jiang L., Kochanek C. S., McGreer I. D., Merloni A., Peterson B. M., Petitjean P., Schneider D. P., Schulze A., Strauss M. A., Tao C., Trump J. R., Pan K., Bizyaev D., 2015, ApJ, 805, 96

Shirakata H., Kawaguchi T., Okamoto T., Makiya R., Ishiyama T., Matsuoka Y., Nagashima M., Enoki M., Oogi T., Kobayashi M. A. R., 2016, MNRAS, 461, 4389

Silk J., Rees M. J., 1998, A&A, 331, L1

Silva D. R., Kuntschner H., Lyubenova M., 2008, ApJ, 674, 194

Sivia D., Skilling J., 2006, Data Analysis: A Bayesian Tutorial. Oxford science publications, OUP Oxford

Skilling J., 2004, in Fischer R., Preuss R., Toussaint U. V., eds, American Institute of Physics Conference Series Vol. 735 of American Institute of Physics Conference Series, Nested Sampling. pp 395–405

Skilling J., 2006, in Mohammad-Djafari A., ed., Bayesian Inference and Maximum Entropy Methods In Science and Engineering Vol. 872 of American Institute of Physics Conference Series, Calibration and Interpolation. pp 321–330

Soltan A., 1982, MNRAS, 200, 115

Somerville R. S., Davé R., 2015, Annual Review of Astronomy and Astrophysics, 53, 51

Sparke L. S., Gallagher III J. S., 2006, Galaxies in the Universe - 2nd Edition

Springel V., 2005, MNRAS, 364, 1105

Springel V., White S. D. M., Jenkins A., Frenk C. S., Yoshida N., Gao L., Navarro J., Thacker R., Croton D., Helly J., Peacock J. A., Cole S., Thomas P., Couchman H., Evrard A., Colberg J., Pearce F., 2005, Nature, 435, 629

Statler T. S., 1995, in Buzzoni A., Renzini A., Serrano A., eds, Fresh Views of Elliptical Galaxies Vol. 86 of Astronomical Society of the Pacific Conference Series, The Instrinsic Shape of Elliptical Galaxies. p. 27

Stoehr F., White R., Smith M., Kamp I., Thompson R., Durand D., Freudling W., Fraquelli D., Haase J., Hook R., Kimball T., Kümmel M., Levay K., Lombardi M., Micol A., Rogers T., 2008, in Argyle R. W., Bunclark P. S., Lewis J. R., eds, Astronomical Data Analysis Software and Systems XVII Vol. 394 of Astronomical Society of the Pacific Conference Series, DER_SNR: A Simple and General Spectroscopic Signal-to-Noise Measurement Algorithm. p. 505

Stoughton C., 2002, AJ, 123, 485

Syer D., Tremaine S., 1996, MNRAS, 282, 223

Tadhunter C., 2008, New Astronomy Reviews (), 52, 227

Tonry J. L., 1984, ApJ, 283, 27

Tonry J. L., 1987, ApJ, 322, 632

Tremaine S., Gebhardt K., Bender R., Bower G., Dressler A., Faber S. M., Filippenko A. V., Green R., Grillmair C., Ho L. C., Kormendy J., Lauer T. R., Magorrian J., Pinkney J., Richstone D., 2002, ApJ, 574, 740

Treu T., Koopmans L. V. E., 2004, ApJ, 611, 739

Urry C. M., 2003, in American Astronomical Society Meeting Abstracts #202 Vol. 202 of American Astronomical Society Meeting Abstracts, Grand Unification of Active Galaxies. p. 22.01

Vacca W. D., Cushing M. C., Rayner J. T., 2003, PASP, 115, 389

Valdes F., Gupta R., Rose J. A., Singh H. P., Bell D. J., 2004, ApJS, 152, 251

Valentijn E. A., 1979, A&A, 78, 367

van den Bergh S., 1960a, ApJ, 131, 558

van den Bergh S., 1960b, ApJ, 131, 215

van den Bergh S., 1960c, Publications of the David Dunlap Observatory, 2, 159

van den Bosch R. C. E., Gebhardt K., Gültekin K., Yıldırım A., Walsh J. L., 2015, ApJS, 218, 10 van der Marel R. P., Franx M., 1993, ApJ, 407, 525

van Dokkum P. G., Franx M., 1995, AJ, 110, 2027

van Velzen S., Falcke H., Körding E., 2015, MNRAS, 446, 2985

Venkatesan T. C. A., Batuski D. J., Hanisch R. J., Burns J. O., 1994, ApJ, 436, 67

Vestergaard M., Osmer P. S., 2009, ApJ, 699, 800

Vestergaard M., Peterson B. M., 2006, ApJ, 641, 689

Vestergaard M., Wilkes B. J., 2001, ApJS, 134, 1

Wandel A., Peterson B. M., Malkan M. A., 1999, ApJ, 526, 579

Wardle J. F. C., Aaron S. E., 1997, MNRAS, 286, 425

Weinberg D. H., Mortonson M. J., Eisenstein D. J., Hirata C., Riess A. G., Rozo E., 2013, Phys. Rep., 530, 87

Willott C. J., et al. 1998, in Bremer M. N., Jackson N., Perez-Fournon I., eds, Observational Cosmology with the New Radio Surveys Vol. 226 of Astrophysics and Space Science Library, A Complete Sample of Quasars from the 7c Redshift Survey. p. 209

Willott C. J., Rawlings S., Blundell K. M., Lacy M., Hill G. J., Scott S. E., 2002, MNRAS, 335, 1120

Wilman D. J., Erwin P., 2012, ApJ, 746, 160

Wing J. D., Blanton E. L., 2011, AJ, 141, 88

Woo J.-H., Urry C. M., 2002, ApJ, 581, L5

Wyithe J. S. B., 2006, MNRAS, 365, 1082

York D. G., Adelman J., Anderson Jr. J. E., Anderson S. F., Annis J., Bahcall N. A., SDSS Collaboration 2000, AJ, 120, 1579

Young P. J., Westphal J. A., Kristian J., Wilson C. P., Landauer F. P., 1978, ApJ, 221, 721

Zel'dovich Y. B., 1964, Soviet Physics Doklady, 9, 195

Zhao W., Braatz J. A., Condon J. J., Lo K. Y., Reid M. J., Henkel C., Pesce D. W., Greene J. E., Gao F., Kuo C. Y., Impellizzeri C. M. V., 2018, The Astrophysical Journal, 854, 124

Zirbel E. L., 1996, ApJ, 473, 144

Zwart J. T. L., Santos M., Jarvis M. J., 2015, MNRAS, 453, 1740